VARIABLE-FIDELITY HYPERSONIC AEROELASTIC ANALYSIS OF THIN-FILM BALLUTES FOR AEROCAPTURE

A Thesis
Presented to
The Academic Faculty

by

Reuben R. Rohrschneider

In Partial Fulfillment
of the Requirements for the Degree
Doctor of Philosophy in the
School of Aerospace Engineering

Georgia Institute of Technology
May 2007

VARIABLE-FIDELITY HYPERSONIC AEROELASTIC ANALYSIS OF THIN-FILM BALLUTES FOR AEROCAPTURE

Approved by:

Dr. Robert D. Braun, Advisor
School of Aerospace Engineering
Georgia Institute of Technology

Dr. Stephen M. Ruffin
School of Aerospace Engineering
Georgia Institute of Technology

Dr. Olivier A. Bauchau
School of Aerospace Engineering
Georgia Institute of Technology

Dr. F. McNeil Cheatwood
Exploration Systems Engineering Branch
NASA Langley Research Center

Kevin L. Miller
Civil Space Systems
Ball Aerospace & Technologies Corp.

Date Approved: 2 April 2007

ACKNOWLEDGEMENTS

First, I would like to thank my parents, Jean and Larry Rohrschneider, for instilling in me a good work ethic and the desire to question the world around me. They provided a loving home, a good environment to grow up in, and supported me in all my activities and interests. I can only hope to, when the time comes, become such a good parent.

I am grateful for my opportunity to work with my adviser, Dr. Robert Braun. His approach to problem solving lends a clarity that all teachers should strive for. In particular, I appreciate his support and the guidance and advice he provided to get me through the difficult parts of my research. His mentoring style is hands off, he is always there for you, and he provides just enough pressure to get the job done.

I would like to thank Dr. John Olds for giving me the opportunity to work in a premier design organization, and allowing me the freedom I needed to decide what I wanted to work on. I am also thankful for the chance to work with, and learn from, my fellow graduate students in the Space Systems Design Lab.

Kevin Miller of Ball Aerospace & Technology Corp. inspired me to attempt this problem and provided guidance during my time there. I would like to thank Jody Ware (ILC Dover) for providing material data. Fred Hausle, Chris Zeller, and Duffy Morales (Ball Aerospace) were instrumental in helping me track down the difficulties in the structural analysis. The help of Forrest Lumpkin of NASA Johnson Space Center and Chris Zeller in compiling and understanding DAC is appreciated. I would like to thank the other members of the ISP and ESR&T ballute teams for providing advice and encouragement throughout the project.

Jin-Wook Lee and Dr. Ruffin provided invaluable help in working with NASCART-GT, for which I am very thankful. Jin-Wook sacrificed many nights with his family to be at work, helping me.

Finally, I'm thankful for the friendship of my lab mates, with whom I have had more fun with than I probably should have had as a grad student, and who made my time here enjoyable.

TABLE OF CONTENTS

LIST OF TABLES

LIST OF FIGURES

LIST OF SYMBOLS OR ABBREVIATIONS

A	Projected frontal area or surface area, m^2.
AIR	An Inherently Safe Reentry Capsule.
B	Constant in bridging function.
BAAT	Ballute Aeroelastic Analysis Tool.
C_A	Axial force coefficient.
C_D	Drag coefficient.
CEV	Crew exploration vehicle.
CFD	Computational fluid dynamics.
CG	Center of gravity.
C_m	Pitching moment coefficient.
C_p	Pressure coefficient.
CSD	Computational structural dynamics.
d	Payload base diameter, m.
D_{major}	Major diameter of torus, $2R$, m.
D_{minor}	Pitching moment coefficient, $2r$, m.
DOF	Degrees of freedom.
dt	Time step size, s.
dy	Small step size in linear coordinate, m.
E	Elastic modulus, GPa or psi.
EOM	Equations of motion.
ESR&T	Exploration Systems Research and Technology.
F	Axial load on membrane at the center of the aft end of the ballute, N.
FEA	Finite element analysis.
FFT	Fast Fourier transform.
g_E	Acceleration due to gravity at Earth, 9.8 m/s^2.

HTA	Hilbert transform analysis.
IRDT	Inflatable Reentry Descent Technology.
ISP	In Space Propulsion.
k	Meridian cord factor, $nT_m/P_{rb}\pi r_b^2$.
k_{heat}	Emperical constant in approximate continuum heating equation.
L_0	Rigid vehicle length, m.
L/D	Lift to drag ratio.
LDA	Logarithmic decrement analysis.
LV	Launch vehicle.
m	Log base in bridging function.
M	Vehicle mass, kg or Mach number.
MBA	Moving block analysis.
MBSA	Moving Boundary Simple Aerodynamics code.
n	Number of gores or number of meridian cords or number density, $1/m^3$.
NASA	National Aeronautics and Space Administration.
$nbmin$	Parameter controlling the minimum number of elements along the body in NASCART-GT.
P	Circumferential force in torus due to radial load, N.
p	Ballute fill pressure or fluid pressure, Pa.
P_{rb}	Pressure difference on membrane at maximum ballute diameter, Pa.
q	Dynamic pressure, $0.5\rho V^2$, Pa.
$\dot{q}$	Heat rate, W/cm^2.
q_w	Heat rate, W/cm^2.
R	Specific gas constant, or major radius of torus, m.
r	Minor radius of torus, m.
r_b	Base radius of vehicle, m.
Re	Reynolds number.

R_n	Effective nose radius, m.
RTS	Real-to-simulated.
s	Speed ratio, $V(2RT)^{-1/2}$.
St	Stanton number.
t	Time, s.
T	Vehicle thickness to length ratio, or temperature.
T_m	Tension in each meridian cord, N.
V	Velocity, m/s.
x	Fill pressure to elasticity ratio, m^3/kg.
y	Linear coordinate or position, m.

Greek Symbols.

α	Angle of attack, deg.
β	Ballistic coefficient, kg/m^2.
γ	Ratio of specific heats.
Δ	Overpressure parameter.
ϵ	Fraction of specular reflection.
λ	Mean-free-path, m.
ν	Poisson's ratio.
ϕ	Membrane elastic constant, N/m.
Ψ	Flow incidence angle.
ρ	Density, kg/m^3.
σ	Axial load factor, $F/P_{rb}\pi r_b^2$.

Subscripts.

$bridge$	Value in the transitional regime based on the bridging function.
$cont$	Continuum regime value.
fm	Free-molecular regime value.
∞	Value in the free stream.
max	Maximum value.

SUMMARY

Ballute hypersonic aerodynamic decelerators have been considered for aerocapture since the early 1980's. Recent technology advances in fabric and polymer materials as well as analysis capabilities lend credibility to the potential of ballute aerocapture. The concept of the thin-film ballute for aerocapture shows the potential for large mass savings over propulsive orbit insertion or rigid aeroshell aerocapture. Several technology hurdles have been identified, including the effects of coupled fluid structure interaction on ballute performance and survivability. To date, no aeroelastic solutions of thin-film ballutes in an environment relevant to aerocapture have been published.

In this investigation, an aeroelastic solution methodology is presented along with the analysis codes selected for each discipline. Variable-fidelity aerodynamic tools are used due to the long run times for computational fluid dynamics or direct simulation Monte Carlo analyses. The improved serial staggered method is used to couple the disciplinary analyses in a time-accurate manner, and direct node-matching is used for data transfer. In addition, an engineering approximation has been developed as an addition to modified Newtonian analysis to include the first-order effects of damping due to the fluid, providing a rapid dynamic aeroelastic analysis suitable for conceptual design.

Static aeroelastic solutions of a clamped ballute on a Titan aerocapture trajectory are presented using non-linear analysis in a representative environment on a flexible structure. Grid convergence is demonstrated for both structural and aerodynamic models used in this analysis. Static deformed shape, drag and stress level are predicted at multiple points along the representative Titan aerocapture trajectory. Results

are presented for verification and validation cases of the structural dynamics and simplified aerodynamics tools. Solutions match experiment and other validated codes well.

Contributions of this research include the development of a tool for aeroelastic analysis of thin-film ballutes which is used to compute the first high-fidelity aeroelastic solutions of thin-film ballutes using inviscid perfect-gas aerodynamics. Additionally, an aerodynamics tool that implements an engineering estimate of hypersonic aerodynamics with a moving boundary condition is developed and used to determine the flutter point of a thin-film ballute on a Titan aerocapture trajectory.

CHAPTER I

BACKGROUND AND MOTIVATION

1.1 Aerocapture

The concept of using aerodynamic lift and drag to effect a change in orbital energy or plane is classified as aeroassist. First introduced in 1960, aeroassist techniques were shown to have substantial mass savings over propulsive methods [70, 123]. Many types of aeroassist trajectories exist including direct entry, entry from orbit, aerocapture, aerobraking and aero-gravity assist. The focus of this thesis is aerocapture.

In an aerocapture manuever, aerodynamic forces are used to decelerate a vehicle from its hyperbolic approach trajectory into a closed orbit about a planet in a single atmospheric pass. The mission profile is illustrated in Figure 1-1, and shows the small propulsive periapsis raise manuever required to achieve orbit. The velocity increment removed during the atmospheric pass can be controlled by modulating the vehicle's aerodynamic lift (using either angle-of-attack or bank angle control) or changing the vehicle drag during the atmospheric pass. Due to the large velocity reduction, aerocapture subjects an orbiter to deceleration and heating (both heat rate and heat load) levels high enough to warrant a protective shroud or aeroshell around the spacecraft.

Traditionally, the protective shroud has been a rigid aeroshell similar to those used for planetary entry missions and these systems have a ballistic coefficient on the order of 50-200 kg/m^2 for a robotic exploration mission. As the ballistic coefficient is lowered, deceleration occurs higher in the atmosphere, reducing the heat rate. For extremely low ballistic coefficients, the heat rate is low enough that fabric and polymer films can be used for thermal protection. This realization gave birth to the

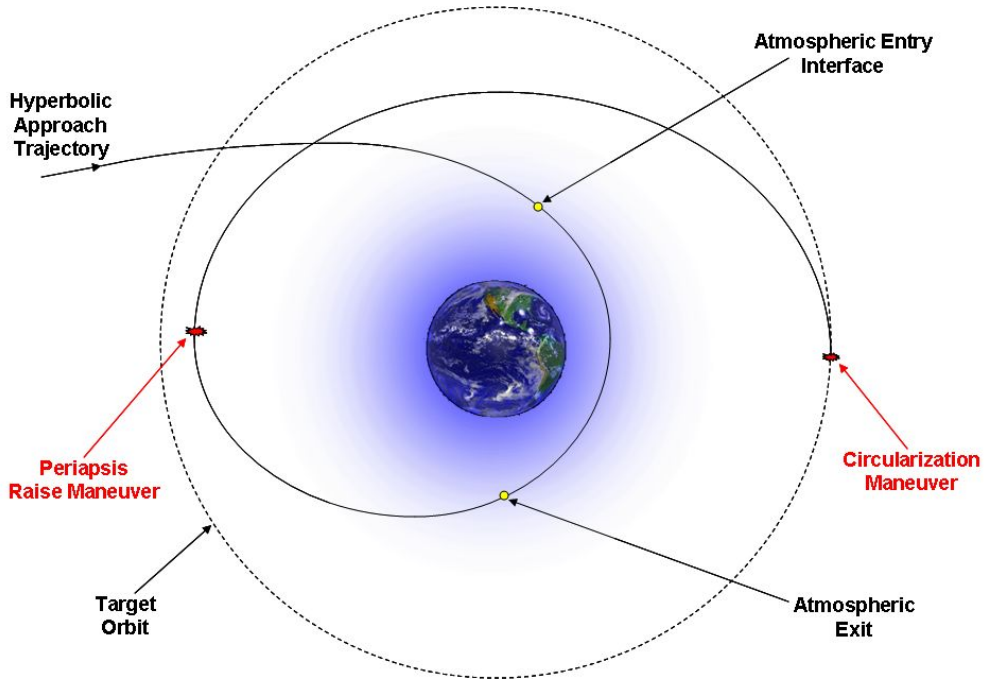

Figure 1-1: Aerocapture mission profile.

hypersonic ballute concept for aerocapture applications.

The Goodyear Aerospace Corp. coined the term "ballute" (a contraction of "balloon" and "parachute" which the original ballute closely resembles) for their cone balloon decelerator in 1962 [56]. The term has become popular in the literature and now refers to any inflatable drag device for high speed deceleration. In the present literature, ballutes are divided into clamped and trailing types, as illustrated in Figure 1-2.

In 1982, Walberg reviewed the aeroassist state of the art, including aerocapture for planetary entry and orbit insertion [121]. Missions to Mars, Saturn (via Titan aerocapture), Uranus, and Venus were reviewed, and all showed significantly reduced launch mass compared to an all propulsive mission (often by a factor of 2).

In [43] several missions are identified from the NASA Space Science Strategic Plan [97] that require orbital insertion or entry at planets with atmospheres, and which could benefit from the mass savings of aerocapture. Mass savings of more

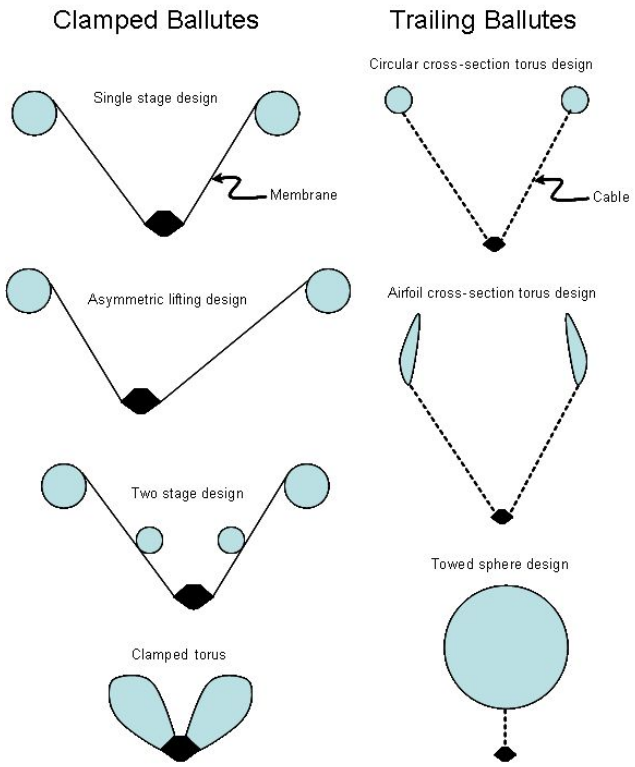

Figure 1-2: Examples of clamped and trailing ballutes.

than a factor of 2 for the orbit insertion system are realized for these missions with incorporation of thin-film ballute technology. Hall and Le [43] also demonstrate that a significant entry corridor exists for each mission where the steep entry limit is the material temperature limit and the shallow entry achieves the required velocity decrement without releasing the ballute.

Three common materials for ballutes are carbon fiber, fiberglass, and polymer films, which maintain sufficient strength up to temperatures of about 3500, 850 and 500°C, respectively. Upilex, Kapton, and PBO are three polymer films with sufficient strength for ballute aerocapture applications at 500°C.

In Ref. [44], Hall et al. compare the mass and cost of aerocapture to chemical propulsion, chemical propulsion with aerobraking, and solar electric propulsion options. Ten planetary missions are studied and include insertion into circular and highly elliptic orbits at each feasible body. The study concludes that aerocapture is

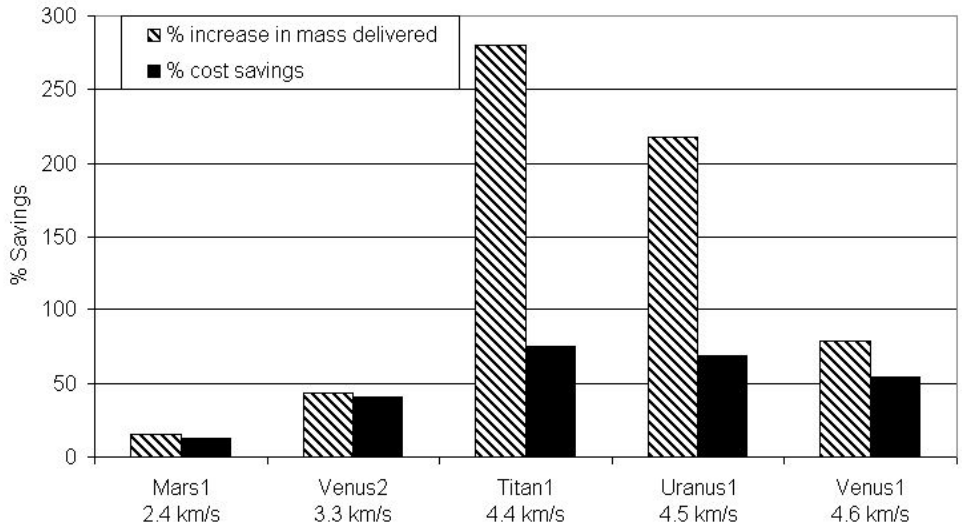

Figure 1-3: Percent increase in mass delivered and cost savings over a non-aerocapture option for planetary missions using rigid aeroshell aerocapture and heavy-lift launch vehicles [44].

enabling for three missions (ΔV = 6 to 17 km/s), enhancing for five missions (ΔV = 2.4 to 4.6 km/s), and not helpful for two of the missions ($\Delta V \leq$ 1.4 km/s). Figure 1-3 shows the mass increase and cost savings afforded by aerocapture over the best non-aerocapture option for each enhancing mission that benefits from aerocapture. In this analysis, rigid aeroshells are used for aerocapture, and a fixed entry mass fraction that ranges between 25% for Mars and 65% for Jupiter, is assumed.

1.2 Early Ballute Development

The instability and low drag coefficient of supersonic parachutes [77] and the desire to recover supersonic, high altitude payloads led to the testing of towed spherical balloons (ballutes) as high speed drag devices by McShera and Keyes [85] in 1961. Many other early tests and studies demonstrated the good supersonic stability characteristics of the ballute [21, 83, 23, 3, 4, 84].

The advantages of the low ballistic coefficient (β) were utilized in Reference [95] as a supersonic decelerator for Mars entry. Both trailing and attached ram-air inflated

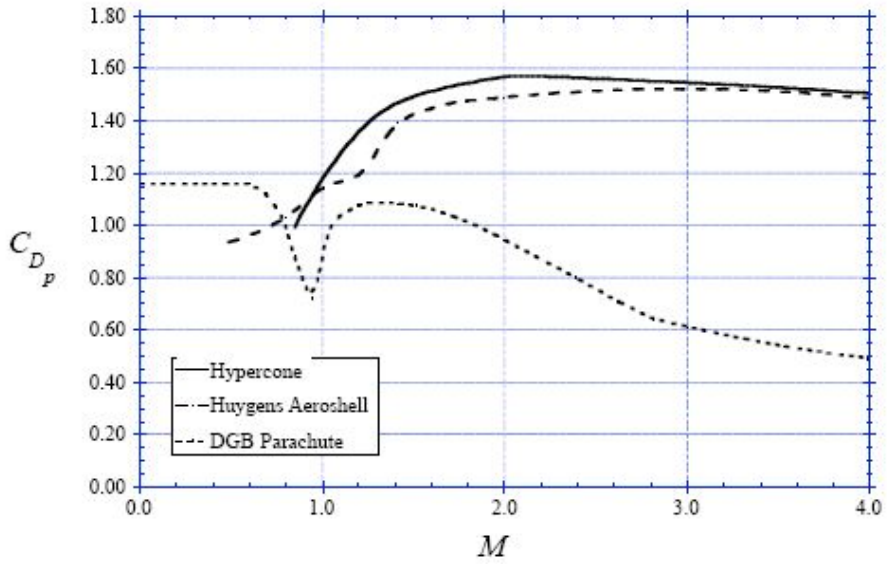

Figure 1-4: Ballutes (Hypercone is a clamped ballute) are more effective aerodynamic decelerators than parachutes above Mach 1 [24].

configurations constructed of Nomex or Dacron cloth coated with Viton or Neoprene were considered. A range of entry conditions were considered with a target of reaching Mach 1 at 6,100 m altitude. All configurations were able to meet the target altitude for material temperatures less than 230°C when deployed at speeds up to Mach 5. In 1966, Alexander reviews the test envelope of clamped fabric ballutes [4]. Tests were conducted with metal ballutes up to Mach 10, but fabric ballutes were not tested at conditions exceeding Mach 3 flight conditions. In References [41, 24], the drag characteristics of the ballute and parachute are summarized as a function of Mach number (and are reproduced in Figure 1-4). Ballutes are shown to be more effective aerodynamic decelerators than parachutes at speeds above Mach 1. The mass delivery advantage of using a supersonic clamped ballute is shown in References [41, 30] for Mars entry. Landed mass advantages in excess of 15% are discovered when deploying a clamped fabric ballute at Mach 5 in place of a parachute at Mach 2.

Reference [46] first proposed the use of a clamped ballute for entry from orbit in 1963 as a single-use personal space rescue vehicle. The concept consisted of a flight seat for a space-suited astronaut around which a clamped ballute inflated. The

system was designed to land without a parachute and utilized an inflatable pad to limit impact acceleration. The concept was later expanded and refined for recovery of both men and payload in Refs. [57, 59, 58].

1.3 Ballute Aerocapture

Traditionally, aerocapture has been analyzed using a rigid aeroshell similar to those used for entry applications [25, 125]. Lift is generally used to control the energy dissipated in the atmosphere in the presence of uncertainties, and so axisymmetric shapes are flown at an angle of attack. French and Cruz showed that an L/D of about 1.5 maximizes the accuracy of the atmospheric exit conditions[29]. References [17, 18, 104, 94, 53, 67] show that sufficient accuracy can be achieved with low L/D vehicles (L/D = 0.3) for Earth and Mars applications. Ballutes, however, are not typically constructed as lifting bodies. In 1999, McRonald demonstrated that lift was unnecessary for aerocapture [81]. Instead, he measures the velocity loss during flight and cuts the ballute when the proper exit conditions are predicted. This allows simple control of the spacecraft exit conditions without requiring lift or bank angle control, and enables the use of ballistic configurations.

In Ref. [121], Walberg points out that one of the most difficult implementation aspects of aerocapture mission design is packaging an orbiter's deployable components inside a rigid aeroshell. To mitigate the packaging concerns of a rigid aeroshell, early ballute studies used a clamped, coated Kevlar fabric ballute with a forward facing rocket engine to produce a low enthalpy boundary layer over the vehicle. The center of pressure of this configuration allowed a more aft center of gravity (CG), and the less restrictive geometry made packaging easier. Recognizing the potential mass and operational advantages of a ballute system, Andrews and Bloetcher [9] and Grenich and Woods [39] proposed ballute concepts for aerocapture in 1981. These early studies focused on reducing the orbital energy from geosynchronous Earth orbit to low Earth

orbit. Andrews and Bloetcher [9] showed that drag could be varied using engine throttling. Because this would impose a mass penalty, variable inflation pressure was specified instead. Even with the low enthalpy boundary layer produced by the engine the Kevlar fabric required a quartz outer layer and insulation to maintain its structural integrity.

Kustas et al. [62, 63] have explored clamped ballute configurations for Mars entry. The configurations considered consist of single and double attached toroids as shown in Figure 1-5. Trajectory analysis indicates a peak heat rate of 35 W/cm^2 and a multi-layer insulation strategy is specified to protect the spacecraft and ballute. Kustas et al. show that their ballute and insulation are 43% less massive than a traditionally designed SLA-561V heatshield of the same diameter.

The low β of ballute aerocapture results in deceleration higher in the atmosphere and with significantly reduced heating rate on the spacecraft. In Reference [81], McRonald used this principle to design ballutes for entry and aerocapture at Mars and Pluto, and discovered that a ballute with a diameter 10 times that of the spacecraft (resulting in a β 100 times lower than that of a rigid aeroshell) could realize a heat rate 100 to 10,000 times less than with a rigid aeroshell.

Figure 1-6 shows the heat rate for a Mars mission using a ballute for aerocapture. The lower curves are for heat rate and the upper curves are stagnation pressure. The vehicle numbers represent spherical towed ballute/spacecraft combinations with β decreasing from 5.0 to 0.05 kg/m^2 for vehicles one to six respectively. As noted previously, lower β leads to lower heat rate. Heating rates below 4.0 W/cm^2 are readily obtained for a ballute ($\beta < 1$) while heating rates of approximately 40 W/cm^2 are obtained for rigid aeroshell ($\beta > 100$) aerocapture [74]. The reduced heat rate eliminates the need for an ablative thermal protection system (TPS) encompassing the spacecraft and relaxes packaging requirements. Furthermore, this low heat rate allows materials to be radiatively cooled to around 500°C.

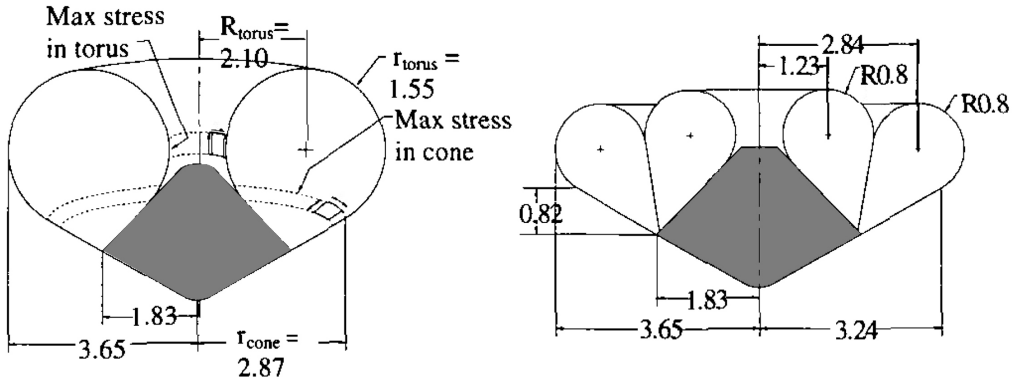

Figure 1-5: Clamped ballute configurations for Mars entry [62].

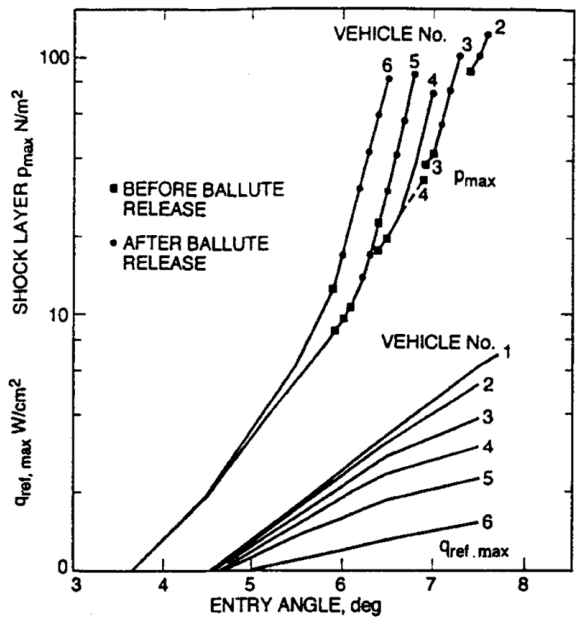

Figure 1-6: Peak heat rate and pressure for spherical thin-film ballute aerocapture and entry at Mars with entry velocity of 5.5 km/s [81].

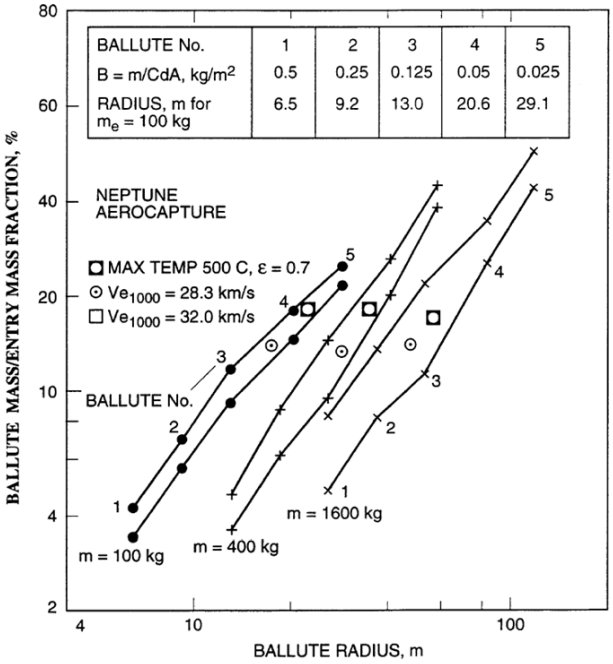

Figure 1-7: Neptune aerocapture ballute mass fraction (ballute mass/entry mass) [82].

Yavrouian et al. [133, 132] present properties of polybenzoxazole (PBO), polyimidobenzoxazole, Mylar, and Kapton thin film polymers at temperatures up to 500°C for balloon applications on Venus. These materials are also well suited for ballute construction. Entry and aerocapture at Venus and Neptune are examined in Refs. [80, 82] with ballute systems constructed of PBO and Kapton. Analysis at Venus, Earth, Mars, and Neptune shows that the ballute mass to vehicle entry mass fraction can be in the 10-20% range. Figure 1-7 demonstrates the ballute to entry system mass fractions possible for aerocapture at Neptune. Two other ballute configurations were examined by McRonald, the lenticular and toroidal ballute, which are depicted in Figure 1-8 and have the goal of reducing the inflation gas mass compared to the spherical ballute.

1.4 Ballute Aerocapture Technical Challenges

Despite the promising outlook portrayed in papers by McRonald [81, 80, 82], Hall and Le [43], and Kustas et al. [62, 63], much of the ballute analysis completed has

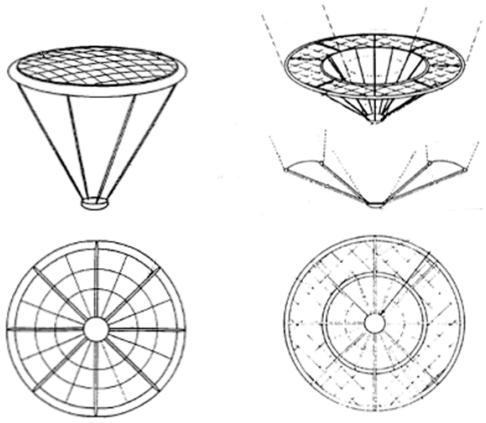

Figure 1-8: Lenticular (left) and toroidal (right) ballutes are designed to reduce inflation gas mass [81, 82].

been at the conceptual level with little subsystem work to define system mass and implementation options.

In 2000, Hall reviewed ballute technology for planetary aerocapture [42] and identified ten key technical issues that need to be resolved for planetary aerocapture. Flow stability, structural integrity, and ballute survivability are included in these challenges, and when combined are the field of aeroelasticity.

The remainder of this chapter provides a summary of ballute aerocapture technology and shows that the disciplinary tools needed for the aeroelastic analysis of thin-film ballutes exist, but their integration into an aeroelastic analysis tool applicable to the high-altitude, hypersonic flight regime has not been performed. In this investigation, the appropriate high-fidelity analysis tools are selected and the low-fidelity, unsteady aerodynamic tools necessary for aeroelastic analysis in this flight regime are developed. The necessary aerodynamic to structural-dynamic coupling code is developed to automate the analysis process, and this automated tool is used to analyze a representative thin-film ballute on an aerocapture trajectory with both high- and low-fidelity aerodynamic tools. These solutions represent the first static and dynamic aeroelastic solutions of thin-film ballutes in an aerocapture environment.

The results of the varying-fidelity analyses are compared, and independent validation data is used to determine the accuracy and realm of applicability of the low-fidelity solution. Finally, an aeroelastic analysis method that is viable for conceptual design of future ballute systems is developed.

1.5 Ballute Aerocapture Technology Survey

In the following sections, the current state-of-the-art in ballute aerocapture is summarized, and the need for aeroelastic analysis of ballutes is highlighted. The majority of studies reviewed have been published since 2000, but some that are particularly relevant from earlier dates are also included. The survey has been separated into sections on trajectory analysis, structural analysis, hypersonic aerothermodynamics, coupled analysis, and flight testing. The current state-of-the-art is summarized at the conclusion of each of these sections.

1.5.1 Trajectory Analysis

During 2003 and 2004 a significant amount of work was performed to determine the aerocapture capability of ballutes at Titan. Miller et al. performed a systems study based on the toroidal trailing ballute. In [86], they detail the analysis, including configuration and spacecraft packaging, aeroheating in the continuum, transitional, and free molecular flight regimes, thermal, and trajectory analyses. An aerodynamic database was developed for a 5:1 (R/r) torus and was used for trajectory analysis. Titan atmospheric entry was initiated at 1000 km altitude, at 6.5 km/s velocity, values typical of a low-thrust trajectory to the Saturnian system. For comparison, Mars aerocapture trajectories were also investigated, with a nominal entry velocity of 5.5 km/s at 200 km altitude. For Titan and Mars, β was 0.4 and 0.8 kg/m^2 respectively. Table 1-1 lists the critical trajectory characteristics of both Mars and Titan aerocapture. Titan trajectory work was extended to include an algorithm for ballute release. The algorithm uses orbital energy as the release criteria and

Table 1-1: Comparison of Mars and Titan aerocapture trajectories [86].

Characteristic	**Mars**	**Titan**
Ballute β (kg/m^2)	0.8	0.4
$\beta_{spacecraft}/\beta_{ballute}$	140	145
V_{entry} (km/s)	5-6	6-8
Pass duration (s)	1100	3600
ΔV (km/s)	2.0	4.8
Peak Deceleration (g's)	2.8	0.9
Peak heat rate (W/cm^2)	2	0.9
Peak dynamic pressure (Pa)	28	46

propagates the trajectory on-board using accelerometer data and an updated density model. A Monte Carlo analysis was performed with perturbations to the atmosphere, accelerometer data, entry velocity, entry flight path angle, and β. The resulting circularization velocity increment and heating values are presented in Table 1-2. Two other sources [126, 55] have implemented algorithms for ballute release at Titan and performed Monte Carlo analysis showing similar performance.

In [71], Lyons and Johnson studied the trailing toroidal ballute for Neptune aerocapture into a highly eccentric orbit with apoapsis at 430,000 km. This study assumed a 500 kg spacecraft and explored three ballute sizes (750, 1477, 3000 m^2) and seven entry velocities (22.4, 22.8, 23.4, 24.1, 25.0, 26.1, 27.2 km/s). Figure 1-9 shows the maximum heat rate on the ballute for the range of entry velocities. Peak heat rate varies between different ballute areas by roughly a factor of two for low entry velocities, and by more than a factor of five for high entry velocities. Larger ballutes at lower entry speeds are advantageous from a heating perspective. Trajectories in this study were targeted independently such that the exit conditions were met without releasing the ballute. Because this method did not account for uncertainties, the heat rates shown would increase once a lower periapsis is targeted to account for uncertainties. Peak deceleration is shown to be 3.5 g_E, but again will increase slightly

Table 1-2: Results of Monte Carlo simulation of Titan aerocapture trajectory [86].

Characteristic	**Value**
Number of failed* cases	0
Min. circularization ΔV	125 m/s
Max. circularization ΔV	376 m/s
Mean circularization ΔV	186 m/s
Mean $+3\sigma$ circularization ΔV	285 m/s
Mean heat rate	1.9 W/cm^2
Mean $+3\sigma$ heat rate	2.1 W/cm^2

*Failure is entering, or not capturing.

once uncertainties are accounted for. Even if the deceleration increased by 40%, the deceleration would still be less than 5 g, a tolerable level for instruments and even humans. The study concludes that heat rate is the driving factor in ballute design for Neptune entry given the high entry velocities, and an effort should be made to design a mission which reduces the arrival velocity so that the heat rate can be maintained within the limits of thin-film materials for reasonable size ballutes.

Ballute trajectory design was explored at the Earth in 2006 as part of the ESR&T funding. Clark et al. [22] explored the ballute design space for CEV entry from lunar return and found that a minimum deceleration of 7.75 g_E and a heating rate of 35 W/cm^2 on the spacecraft was obtained with a shallow ballistic skipping entry that discards the ballute at an inertial velocity of 7.8 km/s. Further reduction in the deceleration and heat rate are obtained by using a spacecraft L/D of 0.3 after dropping the ballute, which can reduce the deceleration to 4 g_E and the heating rate to 21 W/cm^2 on the spacecraft. Using a purely thin-film construction, ballute mass was found to be approximately 37% of the entry mass for the ballute sizes explored. Reduction of either the material areal density or the ballute diameter is necessary for concept viability. Masciarelli et al. [73] analyzed lunar return cases for the Crew Exploration Vehicle (CEV) using ballutes constructed of thin-films and

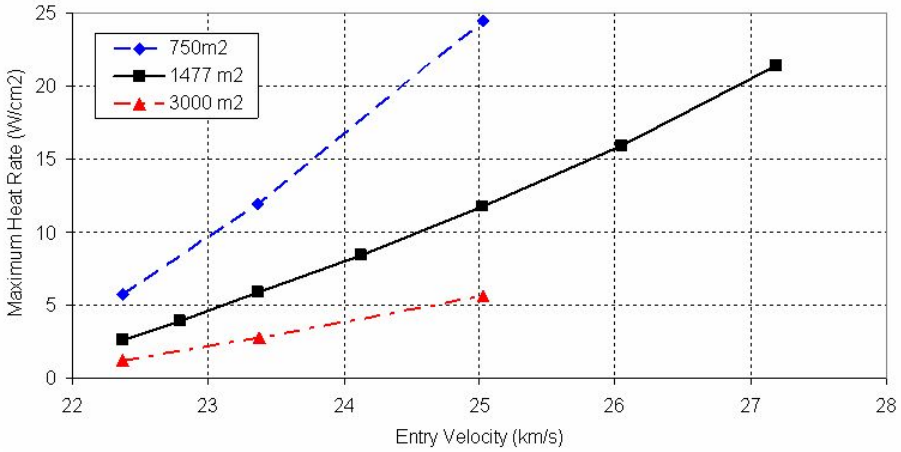

Figure 1-9: Peak heat rate on a trailing toroidal ballute at Neptune [71].

hybrid fabric/insulation/thin-film materials. The study found that local insulation is necessary to maintain a small ballute size such that it can be packed into a space less than 5% of the CEV volume and keep the polymer temperature below 500°C. Material layups composed of fabrics and polymer films show promise for achieving operating temperatures up to 800°C, which would allow smaller, lower mass ballutes. Using a hybrid material with a higher operating temperature allowed the ballute size to be reduced to 20 m, resulting in a ballute with a mass of just 7.3% of the CEV entry mass.

Ballute aerocapture trajectories have been explored thoroughly for a 500 kg spacecraft at Titan. A robust algorithm has been developed that successfully inserts the spacecraft into orbit using drag modulation while accounting for uncertainties. Preliminary analysis at Earth, Neptune, and Mars is also presented and shows that a sufficient entry corridor exists to account for uncertainties. Ballute entry at Earth requires the use of hybrid material construction to be viable. The algorithm presented in [55] needs to be adapted to other atmospheres, or new ones developed, to verify the ability to perform drag-modulated aerocapture at other planets.

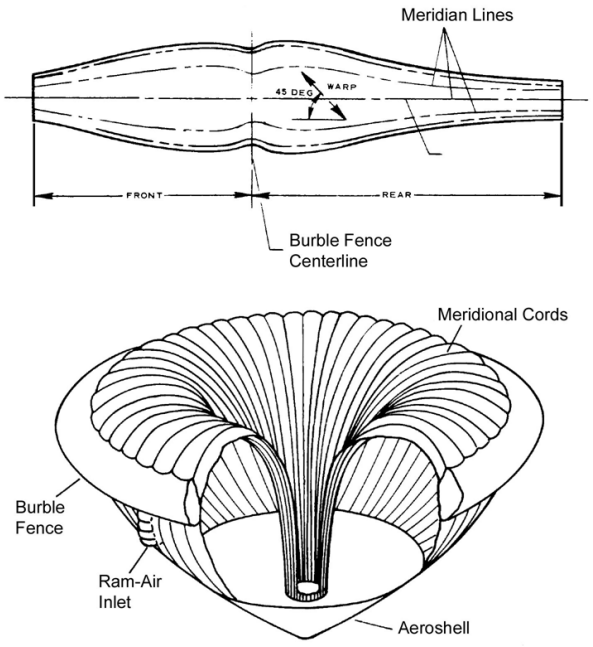

Figure 1-10: Clamped ballute showing the meridian cords and a gore pattern used in its construction [54].

1.5.2 Structural Analysis

Structural analysis of early inflatables was largely based on empirical results and application of simple membrane equations. In 1964, the membrane equations were manipulated by Houtz to show that a uniform stress fabric reinforced with meridian cords could be designed for a given axially symmetric pressure load. In [48], the technique by which the meridian profile, number of meridian cords, and fabric gore shape could be designed is demonstrated using algebra and integration. For a sphere, a meridian cord would follow a line of longitude, and a gore would be the surface pattern between two lines of longitude as shown in Figure 1-10 for a clamped ballute. Solutions to the differential equations are families of curves dependent on the axial load factor (σ) and meridian cord factor (k). When σ is zero, the solution has zero slope at the axis, and when k is zero too, the surface becomes a sphere with uniform stress in all directions. When σ is zero and k is one the stress is carried completely

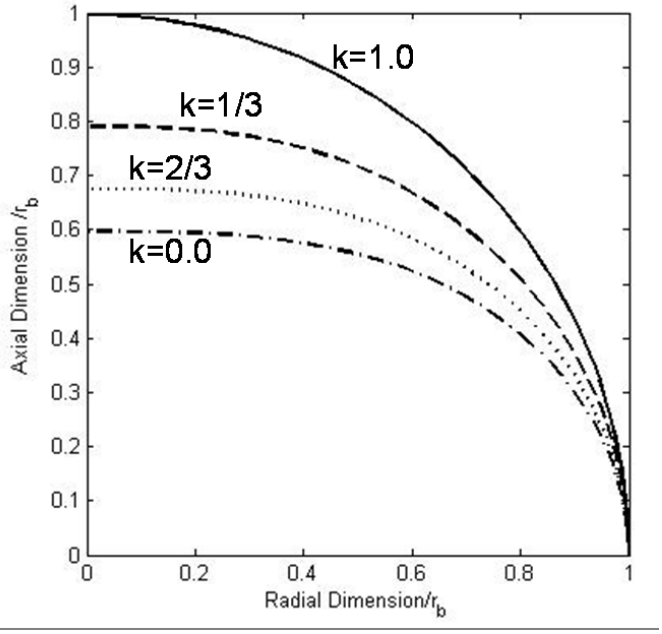

Figure 1-11: Surface curves for $\sigma = 0$ and constant pressure load [48].

in the meridians. These two cases are the bounding curves in Figure 1-11 for a constant pressure load which is typically used for aft surfaces. Here the y-axis is the axis of symmetry and dimensions have been normalized by the base radius of the vehicle. For forward surfaces, the pressure distribution is fixed and the surface shape must be solved. Though not stated in the paper, it would clearly be necessary to iterate between the actual shape obtained and the pressure distribution to achieve a consistent solution. Isotensoid design became the de facto method for ballute design in the later half of the 1960's.

Also in 1964, Anderson [8] identified that aeroshell design is limited by the buckling load case, so the full strength of materials is not used. This led to the concept of the tension shell entry vehicle where the compressive load is isolated in a single ring structure at the base of the vehicle. Anderson also demonstrates that the tension shell shape can achieve a lower ballistic coefficient than a rigid sphere-cone aeroshell due to its structural efficiency, leading to lower weight for a given frontal area. In [7] the shape is mathematically defined using membrane theory and both a constant and

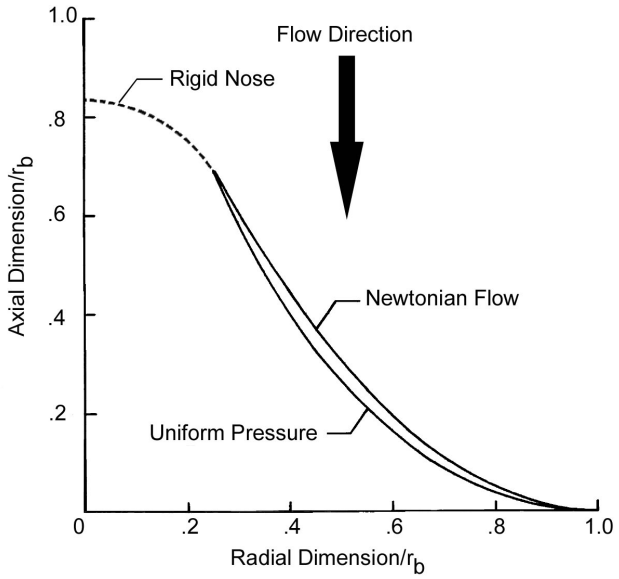

Figure 1-12: Tension shell surface shapes for Newtonian and constant pressure distributions [7].

Newtonian pressure loading. The surface contours for each pressure loading are shown in Figure 1-12 for solutions with the same end points. The vertical-axis is the axis of symmetry with dimensions normalized by the base radius (r_b). The flow direction is from top to bottom. The small difference in the contours indicates that the shape is not sensitive to the pressure distribution since the Newtonian and constant pressure distributions are quite different. From the pressure distribution it was found that for relatively blunt versions of the tension cone, the drag coefficient is between 1.4 and 1.7.

Since the tension shell requires no compressive strength, a thin fabric or membrane can be used as the aerodynamic surface. To achieve very low ballistic coefficients the surface can be deployed using an inflatable torus to support the compression load. In 1967, the equations for buckling of a radially loaded pressurized toroidal shell were developed [124]. These equations were then verified and used in [64] to analyze the deployment and flight of a tension cone. For verification purposes, two fixtures were used to apply a distributed radial load to the torus: a toggle harness, and a vacuum

bag apparatus. Both a slender ($R/r = 7.25$) and a stout torus ($R/r = 4.71$) were tested in each fixture, and three compressive failure modes were identified. The first failure mode is when the circumferential load in the torus due to the radial load (P) exceeds the circumferential force in the torus due to pressure:

$$P > p\pi r^2 \tag{1-1}$$

where p is the fill pressure, and r is the minor radius of the torus. This failure mode was termed the crippling mode and was characterized by a wrinkling of the torus surface followed by the torus folding, out-of-plane, about a single hinge line. The remaining two failure modes are in-plane and out-of-plane buckling modes. The out-of-plane buckling mode appeared as a curling deformation and was able to support an increasing load until the crippling load was reached. The in-plane buckling mode appeared as four hinges and four arcs as shown in Figure 1-13. The buckling load as a function of internal pressure for the slender torus, shown in Figure 1-14, is in good agreement with theory. For the stout torus the results are similar, except that the wall has a larger contribution to the compressive strength, hence collapse is observed consistently at loads greater than the crippling load.

Kyser [64] also developed a model for deployment of an inflated torus based on a hinge moment when the torus is folded, out-of-plane, in half. The model was applied to a tension shell decelerator and tested in a water tow tank. Results indicated that the theory is conservative as complete deployment was observed at lower fill pressures and higher dynamic pressures than predicted. It should also be noted that the surface shape was designed using a Newtonian pressure distribution and produced wrinkles during tow tests, indicating that the actual pressure distribution was far from Newtonian.

In recent years finite element analysis (FEA) has been used to analyze ballutes. Prada y Nogiera et al. [105] detail the analysis of a coated fabric clamped ballute with TPS using FEA. The LS-DYNA structural dynamics code is used to study the

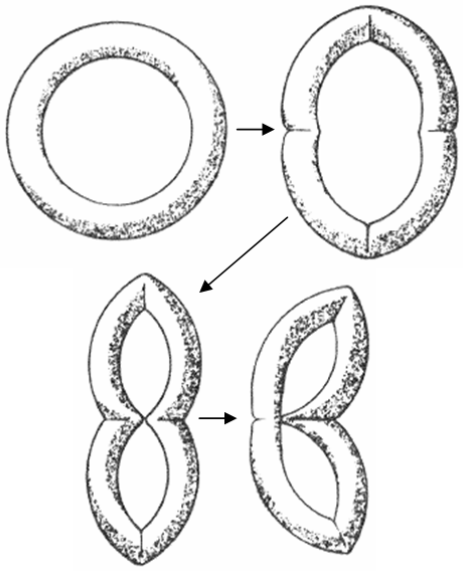

Figure 1-13: Planar buckling mode of a pressurized toroidal shell under uniform radial load [64].

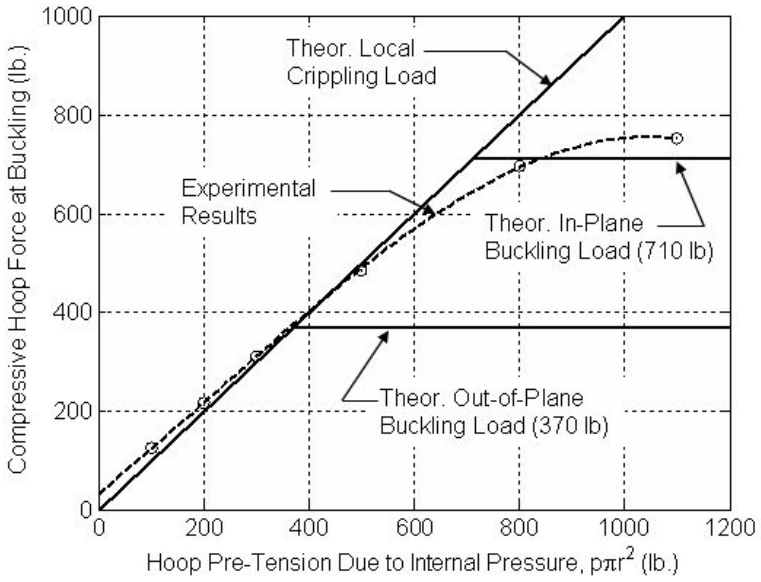

Figure 1-14: Buckling load as a function of internal pressure for a slender torus showing good agreement between experiment and theory [64].

uncoupled deformation due to aerodynamic pressure and the effect of air chamber deflation on two different configurations. The analysis utilized the fabric material and inflation models developed for automotive airbag analysis.

NASTRAN and ABAQUS codes have also been used to model an inflated cylindrical membrane strut. Modal analysis was performed using each analysis package and the results compared favorably to experiment for the first mode. For higher modes, results were not as good, with errors as high as 24%. Within the results for the first mode, better accuracy was achieved for stiffer configurations (thicker membrane and higher inflation pressure). In general, the NASTRAN and ABAQUS codes were found to have similar accuracy.

Numerical modeling of thin polymer membranes has presented several difficulties, including numerical instability and accurate capture of surface wrinkles and deformation. Many of the membrane modeling advances have been made by the solar sail community and are only just starting to be applied to ballutes. In [122], Wang et al. use the ABAQUS code to explore the effects of element formulation and analysis type (implicit vs explicit) on the deformation of a membrane strip under gravity loading. The seemingly simple problem of numerically solving the membrane equations using FEA proves difficult. The implicit solution technique only produced correct results for the membrane element formulation with either stabilization or pre-tension added. Only reduced integration shell elements were able to produce converged solutions, though the results under-predict the deformation. The explicit solution technique used a reduced integration shell element and produced the correct result with artificial damping added to eliminate oscillations due to the load application method.

The numerical prediction of surface wrinkle amplitudes in a true membrane is not possible due to the influence of bending and compressive stiffness on the shape of the wrinkles. Furthermore, initially flat membranes under shear or compression will not buckle because there is no means to produce a bending moment. This problem was

resolved by initially perturbing the nodes by a fraction of the membrane thickness to couple the bending moment to the shear and compressive loads [115]. The method was used to predict wrinkles in a flat membrane subject to a pure shear load and a flat membrane subject to corner tension. The wrinkle patterns in the computational results compare well with experiments, but the amplitudes vary by nearly a factor of 2. Su et al. [111] applied tension field theory to predict the wrinkle patterns, and nonlinear post-buckling analysis to predict the wrinkle amplitudes in a square membrane with corner loads. Amplitude prediction is quite good for wrinkles away from the edges, but wrinkle amplitudes near the edges are much smaller than those found in testing.

Theories have been developed and validated through tests for pressure stabilized structures in the presence of variable external loads. The analytical methods presented provide the tools for preliminary sizing of both clamped and trailing ballutes. The finite element method has been successfully applied to analysis of coated fabric ballutes and modelling of thin polymer membranes should be possible due to advances made by the solar sail community.

1.5.3 Hypersonic Aerothermodynamics

Unsteady flow effects have long been observed in parachutes and so it was not surprising to see them in early supersonic ballute tests. McShera and Keyes observed time varying flow separation from the tow cable in [85], and McShera observed failure due to unsteady flow in [83].

Early tests were at supersonic Mach numbers with relatively high dynamic pressures [32] (at low altitude on Earth). In contrast, aerocapture applications encounter only hypersonic flow and low dynamic pressures ($q < 100$ Pa compared to $q > 12$ kPa), but may still suffer failure due to thermal effects or fluid-structure interaction. Computational and experimental studies of ballute aerodynamics have been performed as

a series of related studies, with overlapping cases for validation purposes.

1.5.3.1 Experimental Results

Rasheed et al. [106] performed a set of experimental studies using a toroidal ballute. The design was advocated based on the thought that the hole in the torus would swallow the spacecraft wake and reduce aerodynamic interaction between the bodies. Due to the resulting small minor radius of the torus, heating was a concern and testing was performed to determine the heating rate on the torus. Heating tests were performed in the Graduate Aeronautical Laboratories, California Institute of Technology (GALCIT) T5 Hypervelocity Shock Tunnel. Test conditions were set to match reference Reynolds number and stagnation enthalpy similarity criteria for aerocapture of the Mars Micro Satellite and the Titan Organics Explorer, two possible applications of a toroidal ballute. The experimentally determined heat rates will be higher than flight conditions due to the high enthalpy flow and small test article dimensions. High enthalpy flow is necessary to capture the effects of flow chemistry and the ensuing change in shock wave geometry. Due to the small geometry, heating due to radiation cannot be captured in shock tube experiments, necessitating a flight experiment to fully simulate the environment. Table 1-3 shows the design parameters for these two missions. Test results show good agreement with theory for the Stanton number as a function of Reynolds number which can be extrapolated to provide heat rates for these missions. Additional tests were performed with the hole of the torus blocked to verify the unsteadiness observed in the computational results [47]. The complex shock shape observed in the experiment indicates the flow was unsteady.

McIntyre et al. [78] extended the work of Rasheed et al. [106] to flows of higher freestream enthalpy to better capture the effects of dissociation and ionization. A moderate enthalpy case (18 MJ/kg) in CO_2 and N_2 was studied for comparison to the previous study, and a high enthalpy case (50 MJ/kg) was studied to see the effects

Table 1-3: Ballute mission design parameters [106].

Design Parameter	**Mars Micro Satellite Value**	**Titan Organics Explorer Value**
D_{major} (m)	15	52
D_{minor} (m)	3	13
V_∞ (m/s)	5490	8550
ρ_∞ (kg/m^3)	7.1x10^{-7}	1.9x10^{-7}
Gas	95% CO_2	98% N_2

Table 1-4: Measured and calculated stagnation point results for moderate enthalpy flow in N_2 [78].

Shot	**Re$_e$**	**Exp. heat rate ±3 MW/m^2**	**Exp.St$_e$ ±0.7x10^3**	**Theor. heat rate MW/m^2**	**Theor.St$_e$**
C1	2090	24	10.0x10^{-3}	24.0	10.1x10^{-3}
C2	2800	27	9.3x10^{-3}	26.3	9.06x10^{-3}
C3	2800	25	8.6x10^{-3}	26.3	9.06x10^{-3}
C4	2800	19	6.5x10^{-3}	26.3	9.06x10^{-3}

of dissociation and ionization. Additional testing was performed at high enthalpy (80 MJ/kg) in a Hydrogen-Neon gas to simulate entry into a gas giant. The toroidal ballute model used in [106] was scaled to fit in the University of Queensland superorbital expansion tube, X2. Both a standard torus and a blocked torus model were used to explore the effects of choked flow. In general, it was found that shock interaction occurs further downstream for higher enthalpy and higher Mach number flows. Good agreement between calculated and experimental heat rate was observed for the moderate and high enthalpy N_2 conditions and the high enthalpy CO_2 condition. The flow around the blocked torus was unsteady in all conditions. Table 1-4 shows the good agreement obtained between the experimental data and the calculated heat rate and Stanton number (St) for the moderate enthalpy N_2 case. When higher freestream enthalpies were included it was found that the Stanton number still followed the $Re^{-1/2}$ relation found in [106].

1.5.3.2 Computational Studies

In 2001, Hornung [47] performed a series of time-accurate inviscid computational fluid dynamics (CFD) solutions for vehicles with an elliptical and a toroidal towed ballute. The study examined the effect of towing distance and a sting support. The elliptical trailing body was found to have violently unsteady flow for medium towing distances, but steady flow for very short or very long towing distances. Figure 1-15 shows a pseudo-schlieren image at Mach 10 for an elliptical towed ballute at medium distance with unsteady shock structure. Since the unsteadiness in the flow originated from interaction of the towing spacecraft wake with the shock structure of the towed ballute, it was thought that moving the shock interaction further downstream from the spacecraft would improve the situation. By using a toroidal ballute the towing distance could still be reasonable, and the shock interaction would be moved downstream because it would pass through the hole in the torus. Further computations showed that the spacecraft wake was swallowed, but the shock reflections on the axis of symmetry produced such high pressure that the shock moved upstream to the base of the towing spacecraft, producing unsteady flow in its wake. The addition of a sting supporting the spacecraft significantly reduces unsteadiness and leads to a much more benign environment for the spacecraft. This indicates that sting-supported wind tunnel tests may not discover the full extent of unsteady flow.

Because the torus must be connected to the spacecraft with a tension device, it would be advantageous to counter the radial force of the tethers with outward lift from the torus. An outward radial force can be provided by giving the torus an elliptical cross section with an angle of attack. Analysis of this configuration yielded the steady shock structure shown in Figure 1-16. The effectiveness of a ballute can be based on the mass required to achieve equivalent drag. Analysis of the elliptical and toroidal ballutes shows that the primary difference is in the inflation gas, with the toroidal ballute requiring about one quarter the volume of the elliptical ballute.

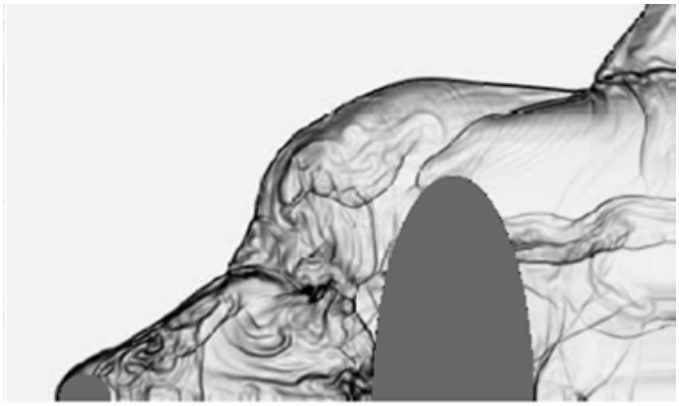

Figure 1-15: Elliptical towed ballute at medium distance, Mach 10 flow, and unsteady shock structure [47].

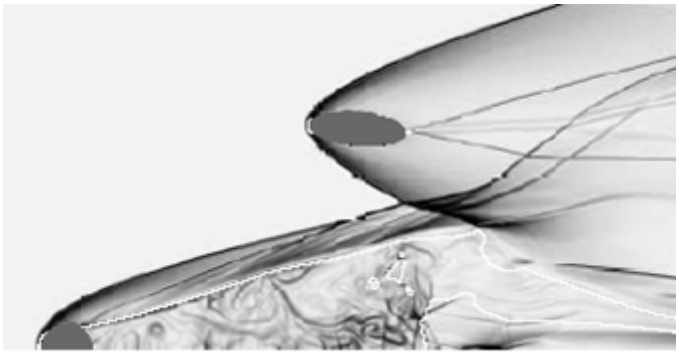

Figure 1-16: Steady flow over a sphere towing a toroidal ballute with elliptic cross section at an angle of attack to counter the radial tether forces [47].

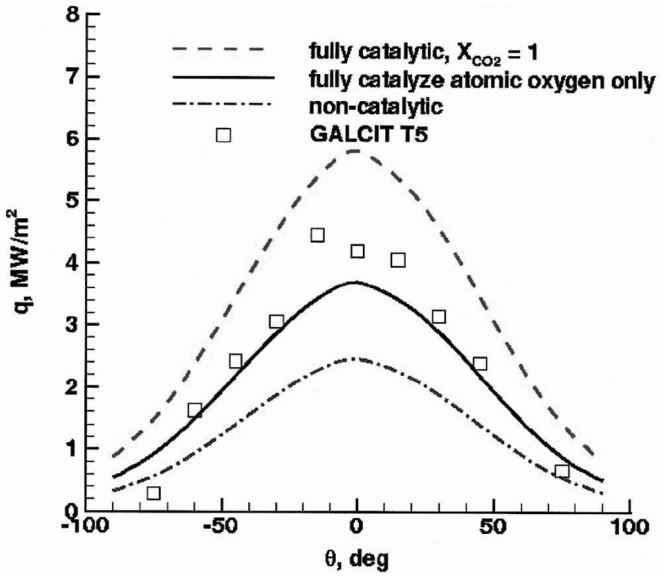

Figure 1-17: Heat transfer on the wall of a toroidal ballute in CO_2 computed by LAURA and measured in the GALCIT T5 shock tunnel [33].

Computational studies using the LAURA [31] algorithm were performed by Gnoffo [33] for one of the toroidal ballute cases (torus only) run in the GALCIT T5 shock tunnel [106] (case T2018-toroid) to validate the computed heating rate. The computational models include viscous and high temperature effects [35]. To capture high temperature effects, the validation experiment used a high enthalpy flow with a scale model, resulting in heat rates significantly higher than expected in flight. Three different boundary conditions were analyzed (see Figure 1-17) with the experimental data being bounded by the fully catalytic wall and the fully catalyzed atomic oxygen only cases, except near $\theta = 90$ deg. Drag coefficients for toroidal and spherical ballutes are also calculated in the Venus, Saturn, Titan, and Neptune atmospheres.

Additional computational studies of toroidal and spherical trailing ballutes were performed by Gnoffo and Anderson using the LAURA algorithm in the Titan atmosphere [34]. Studies of a trailing toroidal ballute found that a steady solution exists with no flow impingement on the aft of the spacecraft. The same model run with an increased Reynolds number produced a much stronger interaction which enveloped the base of the spacecraft as in [47], but the solution had only small oscillations near

the base of the spacecraft. Even with flow impinging on the aft end of the spacecraft there was no unsteady flow interaction with the ballute. The increased heat rate on the spacecraft could easily be countered by addition of TPS to the spacecraft backshell.

For the trailing spherical ballute studies, the same six meter diameter spacecraft was used, and a 70 m diameter sphere was towed at distances ranging from zero to 200 m (0, 30, 40, 50, 100, 200 m). For towing distances between 30 and 200 m the peak drag produced by the ballute occurs at a tow line length near 50 m. For the longer towing distances the ballute is almost completely enveloped in the low dynamic pressure of the spacecraft wake, producing significantly less drag. There is also a significant increase in heat rate on the ballute where the spacecraft bow shock intersects the inflated sphere. In all computational cases, a steady state flow resulted for the baseline conditions, and a recirculation zone was present in front of the sphere for tow distances between 30 and 100 m. As with the toroidal ballute, a ten fold increase in Reynolds number produced marginally unsteady flow with upstream flow extending to the base of the spacecraft for the 40 m towing distance, similar to that observed for elliptical ballutes in [47]. For the limiting case of zero tow distance the spacecraft is protected within the shock layer of the ballute, resulting in lower heat rates.

Figure 1-18 compares the convective heating rate on the clamped ballute configuration to the heating rate on the sphere and spacecraft for the trailing ballute configuration. The lack of shock interactions, unsteady flow, and reduced heating rates make the clamped ballute configuration an attractive option. In the analysis of both the toroidal and spherical ballutes, the wake flow had a Knudsen number of order one or higher, invalidating the continuum solution. Future work needs to include a mix of continuum and transitional regime solutions in these cases.

In 2004 Anderson studied the static stability and effects of transitional flow

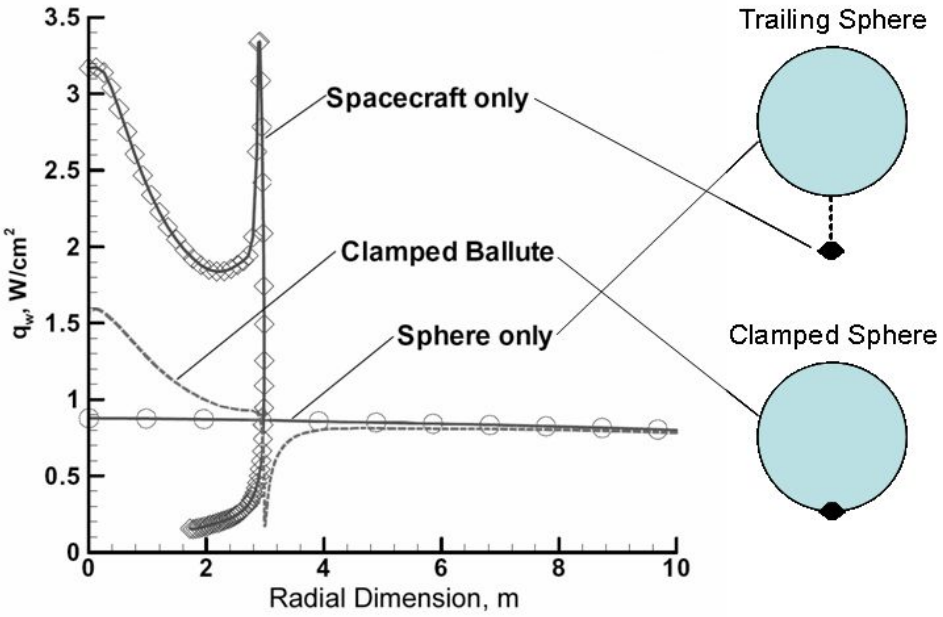

Figure 1-18: Heat rate on the towed sphere and spacecraft for the trailing ballute configuration compared to the clamped ballute configuration [34].

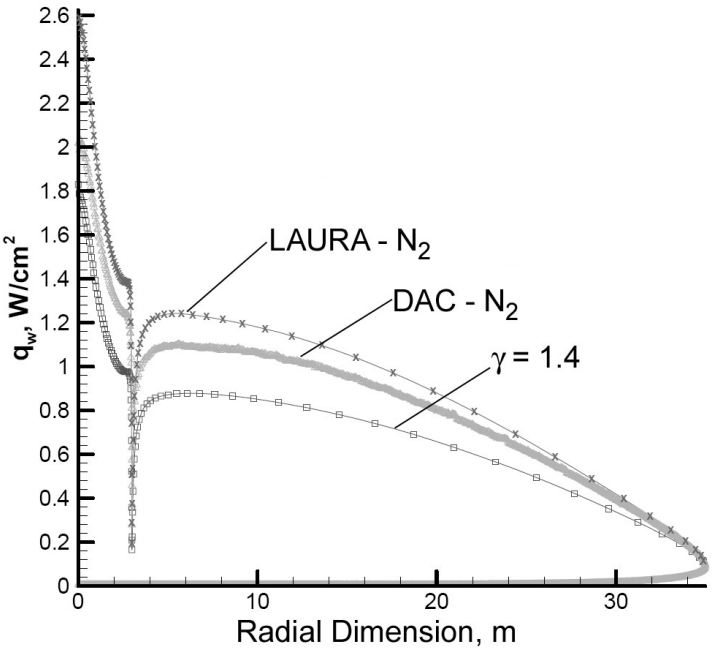

Figure 1-19: Effects of transitional flow on the surface heat rate to a clamped ballute [5].

on a spherical, clamped ballute [5]. Static stability was determined from a three-dimensional continuum solution at 5 deg. angle of attack. It was found that the clamped ballute was statically stable ($\frac{\partial C_m}{\partial \alpha} < 0$). The effects of transitional flow on the ballute were determined by using a direct simulation Monte Carlo solution. The resulting heat rate falls between the continuum solution for a perfect gas with $\gamma = 1.2$ and a gas in thermal and chemical non-equilibrium with $\gamma = 1.4$, and is shown in Figure 1-19.

The premise of achieving lower system mass through increased size, lower β, and lower heat rate is questioned by Park in [99]. He points out that radiative heating has not been considered, and while convective heat rate decreases with increasing size, radiative heat rate is proportional to shock stand-off distance, and so increases with vehicle size. Park reviews the radiative heat rate observed in ground and flight tests and the theories for predicting radiative heat rate. Using the best theory available (in 1987), the radiative heat rate for Earth return from Geosynchronous Earth orbit ranges from 2.5 W/cm^2 to 7.0 W/cm^2 for nose radii of 3 and 12 m respectively, with the rate increasing by a factor of 2.4 for lunar return. In 1991 Tauber and Sutton [114] presented improved computations indicating that the radiative heat rate should be even higher - between 30 W/cm^2 and 83 W/cm^2 (at 72 km altitude) for vehicles with nose radii of 3 and 12 m respectively. This level of heat rate input would be problematic for many candidate ballute materials. Unfortunately, these values are only valid up to 72 km altitude, far below the altitude of peak heating on a ballute trajectory. Clearly, additional work is needed to determine radiative heating effects, and these effects must be factored into ballute system design.

The work done in the area of hypersonic aerothermodynamics has shown that unsteady flow exists for simple (spherical and elliptical) trailing ballutes, but can be avoided by using a toroidal trailing ballute at low Reynolds numbers or a clamped ballute. Testing has verified the convective heat rate predictions of the computational

methods currently in use. Estimation of radiative heat transfer at high altitudes at Earth and for non-terrestrial atmospheres remains a major issue. Further work is necessary to determine the effects of rarefied and transitional flow in the spacecraft wake for trailing ballutes.

1.5.4 Coupled Analysis

Recognizing that structural shape and aerodynamics are coupled, Park simplified the ballute to a two-dimensional problem and found a set of differential equations subject to constraints that defined its shape [100]. This set of equations was integrated numerically for a given angle of attack, ballute geometry, internal pressure, and material elasticity to find the aerodynamic parameters. Using an analytical approach enabled Park to study the possibility of using internal pressure to control drag. Figure 1-20 shows the variation in drag coefficient as a function of the overpressure parameter (Δ) and pressure-to-elasticity ratio (x), defined as:

$$\Delta = \frac{p}{\rho U^2} - 1 \tag{1-2}$$

$$x = \frac{L_0}{\phi} V^2 (1 + \Delta) \tag{1-3}$$

For small values of x, the membrane stiffness dominates, and the overpressure parameter provides little control of ballute drag. When x is 1, drag can vary by a factor of 5. Therefore x must be of order 1 or greater to use internal pressure to control ballute drag.

A simple aerocapture trajectory was calculated using planar translational degrees of freedom and one rotational degree of freedom. The trajectory was run with the CG at 0.3000, 0.4375, and 0.4438 times the vehicle length and a small initial angle of attack. The two cases with the CG closest to the nose were stable, but the case with CG $= 0.4438 L_0$ became unstable and started to tumble in the low density atmosphere. For stability at all freestream densities the CG must be less than $0.18 L_0$. Placing the

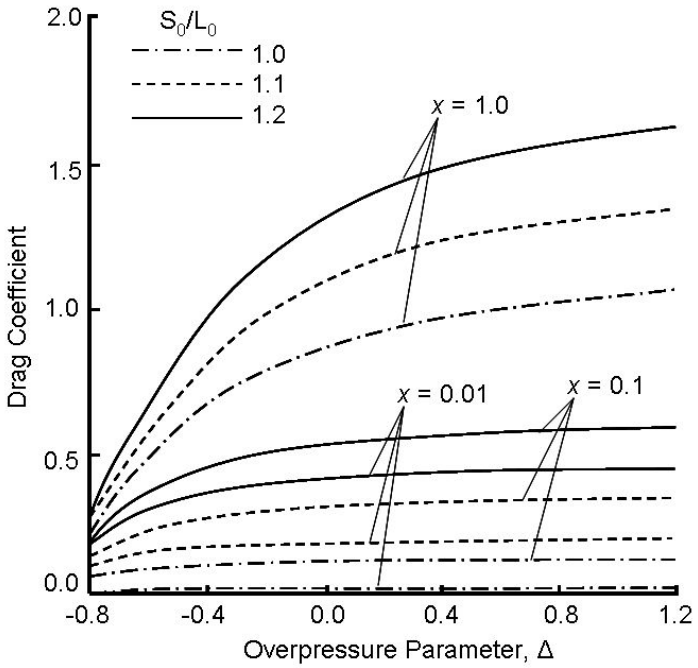

Figure 1-20: Variation in C_D as a function of Δ and x at 0 deg angle of attack [100].

CG at $0.18L_0$ is very restrictive, but subsequent trajectory work showed that the ballute's dynamic motion was bounded up to CG = $0.4375L_0$ since the relatively short time spent in the low density region of the atmosphere does not allow the aerodynamic instability to propagate significantly.

Numerical solutions of the Navier-Stokes equations emerged in the late 1970's and early 1980's. Abe [2] used CFD to iteratively determine the surface shape of a tension shell vehicle. For this study, an axisymmetric CFD solution was used to determine the pressure distribution. The pressure distributions showed good agreement with experimental results, but poor agreement with Newtonian theory at Mach 7. The discrepancy is due, in part, to separated flow for models with large nose radius relative to base radius, which Newtonian theory cannot capture. The iterative method used to achieve a consistent coupled solution converged in less than four iterations and consistently produced a shorter (more blunt) shape than the initial guess (the initial guess was a uniform pressure distribution). Figure 1-21 shows a representative

example of the surface pressure and shape after each iteration.

The next major advance in modeling of ballutes was the time accurate coupling of computational structural dynamics (CSD) and CFD by Mosseev in 1997 [92]. Mosseev presents a coupled solution for the deployment of a trailing ballute at Mach 2 and its final shape using the MONSTR code. The MONSTR code combines a fabric shell structural dynamic solution with three different continuum flow solvers capable of handling moving boundaries. The technology is applicable to any thin, flexible body and Mosseev [93] compares the numerical solution for surface pressure and aerodynamic coefficients to experimental data for several parachutes and a supersonic ballute. The results are quite accurate for the subsonic and low supersonic flight regimes examined. While the code appears capable of transient solutions, the flight condition was fixed for the analysis presented. No hypersonic cases were computed, likely because the aerodynamics code they used was not applicable in that flight regime.

Bartels et al. propose wind tunnel tests utilizing the NASA Langley Transonic Dynamics Tunnel to explore the effects of model scale and construction techniques in conjunction with a computational effort [11]. The computational effort would focus on coupling a nonlinear FEA code to a hypersonic aerothermodynamic code using loose coupling for static solutions and closely coupled modal methods for dynamic solutions. Due to large computational requirements, system identification and order reduction are suggested when possible. While this computational aeroelasticity technique has been demonstrated for a generic launch vehicle in hypersonic flight [116], no hypersonic cases relevant to aerocapture have been computed.

Aeroelastic analysis of ballutes poses many challenges, including: 1) coupling of a highly flexible structure, 2) nonlinear fluid and structure behavior, 3) FEA of highly nonlinear membranes, and 4) experimental validation of results [11]. Coupled CSD

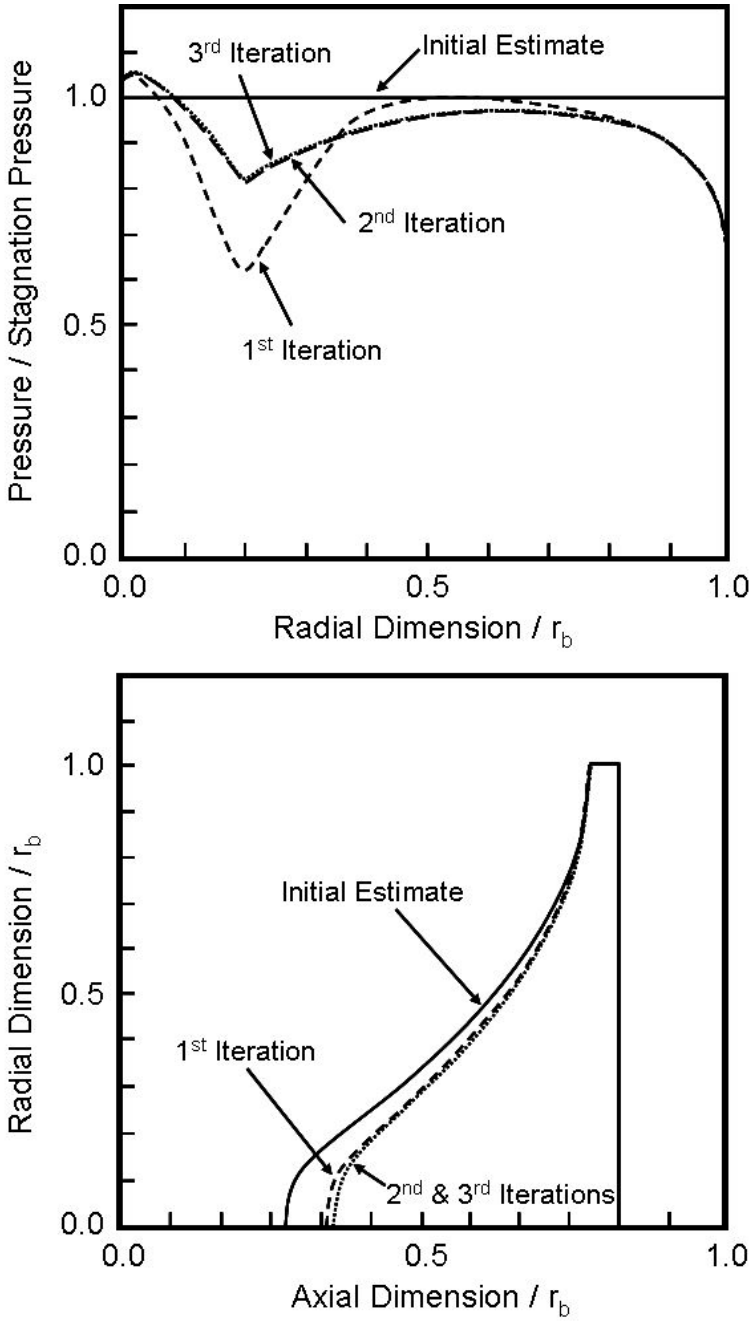

Figure 1-21: Iteration history of pressure distribution (top) and vehicle shape (bottom) for a consistent tension shell vehicle [2].

and CFD codes represent a significant advance in modeling of inflatable decelerators, but lack the ability to find solutions for aerocapture trajectories where flight conditions are in the transitional and free-molecular regimes, and in the hypersonic continuum regime where high temperature effects are important. Many challenges to ballute aeroelastic analysis have been identified and ongoing work in this area is described further in Section 1.5.6. A complete simulation package for ballute aerocapture would also include coupling to thermal and trajectory analyses so that performance and integrity of the complete system could be evaluated in a fully coupled manner.

1.5.5 Past Flight Testing

At the time of this writing (April 2007) no ballute has successfully been flight tested in aerocapture relevant conditions. However, successful ballute tests have been achieved for subsonic and supersonic applications [38, 76, 127, 109]. Three attempts have been made in Russia and Europe to fly a hypersonic inflatable decelerator. The first inflatable decelerator flight system was on the penetrators for the MARS-96 mission which failed to leave Earth orbit following launch. The second two attempts were the inflatable reentry descent technology (IRDT) demonstrators. Though the MARS-96 mission and IRDT missions are entry missions, they encounter similar flight conditions to an aerocapture mission.

1.5.5.1 MARS-96 Penetrators

The MARS-96 mission carried two penetrators with surface science and seismology payloads. The penetrator configuration consisted of a long spike with a small rigid cone and an inflatable brake [134]. Figure 1-22 shows the penetrator layout with the rigid and inflatable brakes identified. The penetrators were to be released during Mars approach and intersect the atmosphere at 5.6 km/s and -12±2 deg. flight path angle. Each penetrator had a mass of 45 kg and carried a 4.5 kg scientific payload.

Table 1-5: Critical events during entry for IRDT [37].

Entry Event	**Value**	**Altitude**
Deorbit burn		600 km
1^{st}-stage deploy		200 km
LV Separation	t=0 s	150 km
Entry velocity	5.4 km/s	100 km
Entry angle	-7.3 deg	100 km
Peak heat rate	31.3 W/cm^2	61 km
Peak accel.	13.5 g_E	53 km
2^{nd}-stage deploy		30 km
Ground impact	14 m/s	0 km

Decelerator size was designed to achieve ground impact at 80±20 m/s, resulting in ground penetration up to 6 meters. The inflatable brake was a second stage decelerator designed to deploy at Mach 15 during the Mars atmospheric entry. Unfortunately, on November 16, 1996, the MARS-96 launch vehicle upper stage failed to ignite and the spacecraft re-entered the Earth's atmosphere, terminating the mission.

1.5.5.2 Inflatable Reentry Descent Technology

Due to the upper-stage failure of the MARS-96 penetrator mission, an Earth test was proposed for this technology. The test flight planned the return of an instrumented payload from Earth orbit using a two stage conical ballute. The mission and vehicle parameters are given in [51, 37]. The layout and critical dimension of the vehicle are shown in Figure 1-23. The aerodynamic decelerator mission profile began with inflation of the first-stage ballute while still attached to the Fregat upper stage. Separation was commanded and the IRDT ballute encountered the Earth's atmosphere at 100 km altitude, 5.4 km/s, and -7.3 deg flight path angle. The second stage ballute was deployed at about 30 km altitude and increased the ballistic coefficient by a factor of five, allowing a slow final descent and impact at 14 m/s. Table 1-5 lists the critical events during entry.

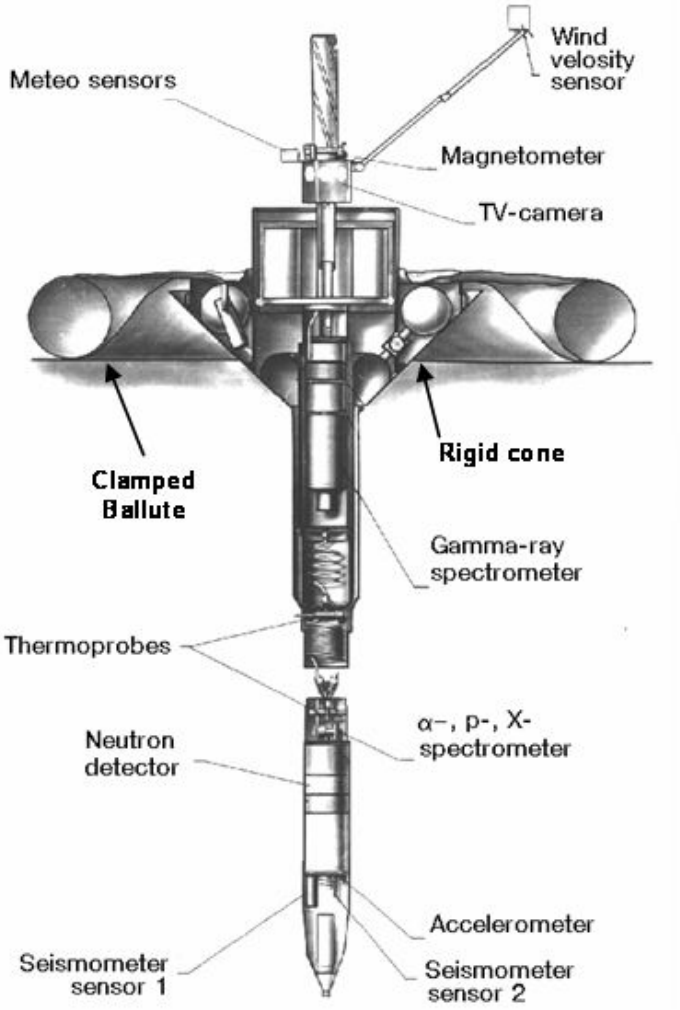

Figure 1-22: MARS-96 penetrator schematic showing the rigid cone and clamped ballute [134].

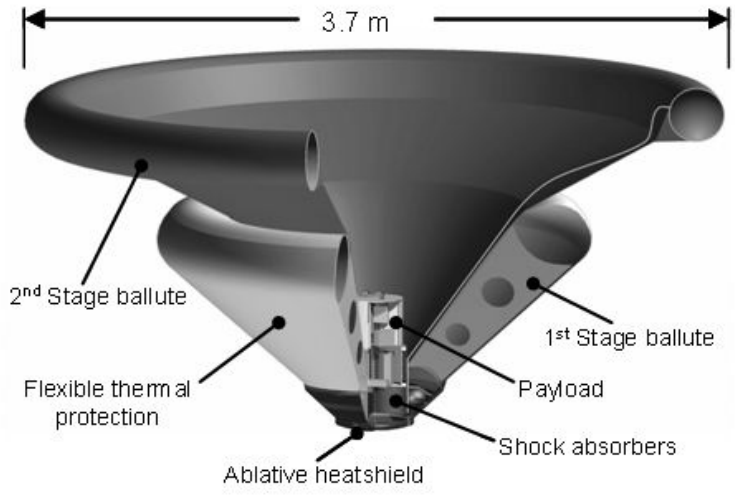

Figure 1-23: IRDT configuration [37].

The IRDT test flight took place in February of 2000 aboard a Soyuz/Fregat launch vehicle. Gräßlin and Schöttle [37] describe the post-flight recovery and trajectory reconstruction efforts. Upon recovery of the vehicle, inspection revealed destroyed first- and second-stage ballutes, higher than expected ablation of the ablative heatshield, full second-stage gas bottles, and an impact damaged payload canister. Despite the loss of the inflatables and damage to the payload canister, the instruments recorded the flight data and this data was successfully retrieved. Linear acceleration, angular acceleration, pressure, and temperature measurements were recorded. Data recording was started at 150 km altitude. Several spikes in the acceleration curve were noted shortly after the start of recording. These spikes are indicative of impact with a foreign object, most likely the payload adapter of the upper stage that induced a tumbling motion, later damped by aerodynamic forces. Upon entry, forces were primarily in the axial direction, indicating proper functioning of the ballute, but about 50 s after entry interface (near peak deceleration) the capsule began to tumble again. The tumbling motion exposed the back of the payload where the pressure sensor is mounted, and increased pressure is observed in the readings corresponding to this region of the trajectory. After about 90 s, the tumbling motion was damped and the

vehicle descended at about 60 m/s, significantly above the nominal rate of 14 m/s. The increased descent rate correlates well with the drag produced by the rigid core of the vehicle alone, indicating failure of both ballute stages. A definitive cause of failure was not determined. The Fregat upper stage was also outfitted with a scaled up version of the IRDT ballute. The Fregat stage entered, but was not recovered.

Since the initial IRDT flight was largely unsuccessful a reflight was planned (IRDT-2). Wilde and Walther [128] describe the improvements to the heatshield design, pressure control system, data acquisition and telemetry system. Improvements were based on the desire for more complete information in the case of a failure. The packaged layout for IRDT-2 is shown in Figure 1-24. The system has a mass of 140 kg, 30 kg more than IRDT due to the extra instrumentation. This flight was initiated on a Russian Volna submarine launched rocket, and would simulate a 7.8 km/s entry with -2.0 deg flight path angle. Launch occurred on July 7, 2001 but the payload failed to separate from the launch vehicle and the vehicle was never found. An identical reflight named IRDT-2R was launched in October 2005, but was also not recovered.

1.5.6 Advancing Ballute Technology

Numerous studies have shown the mass advantage of using ballutes for aerocapture and entry. Recent advances in materials technology and integrated aerothermal-structural analysis have spurred a new round of research to develop the concept further. Ongoing work is critically focused on advancing the technology readiness of fabric and thin-film ballute concepts, leading to flight validation.

The Inflatable Reentry Vehicle Experiment (IRVE) is currently under development at NASA Langley Research Center. A clamped fabric ballute composed of concentric toroids is being designed for launch on a sounding rocket [49]. While not entering from orbit, the resulting supersonic trajectory will approximate the heating and loads

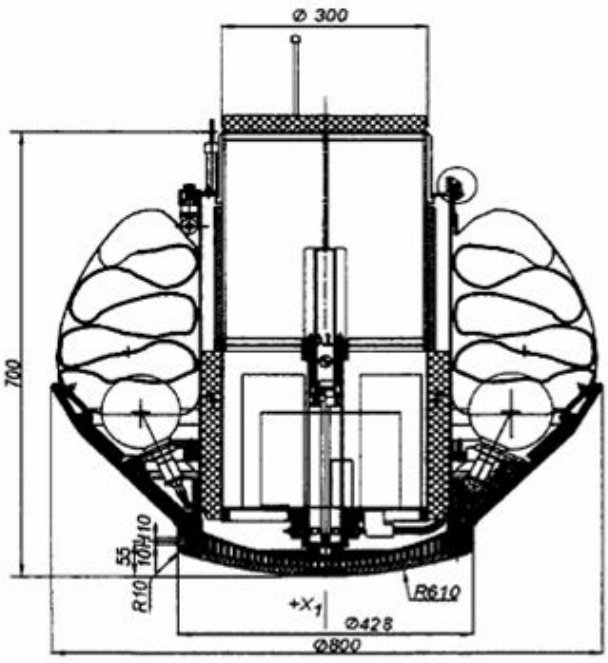

Figure 1-24: Packaging of IRDT-2 [128].

encountered during Earth entry. Figure 1-25 shows a schematic of the layout of the IRVE vehicle. Launch is planned for 2007.

The Program to Advance Inflatable Decelerators for Atmospheric Entry (PAI-DAE) project aims to develop material layups, atmospheric deployment, and plans for technology development for inflatable aerodynamic decelerators. PAI-DAE research is focused on inflatable aerodynamic decelerators with smaller diameters and heavier materials than thin-film ballutes. Flexible thermal protection systems and bladder materials will be tested in mission relevant conditions, and deployment tests will be conducted in the NASA Glenn Research Center 10x10 ft. supersonic wind tunnel of a tension shell configuration. Follow-on plans for 2008 outline performance and dynamic stability wind tunnel tests and subscale testing to determine backshell heating.

The 2nd young engineers' satellite project is a completely student-built project started in 2002. Kruijff et al. [61] describe the mission, detailing the use of a tether to de-orbit "an inherently safe reentry" (AIR) capsule for entry and landing in mainland

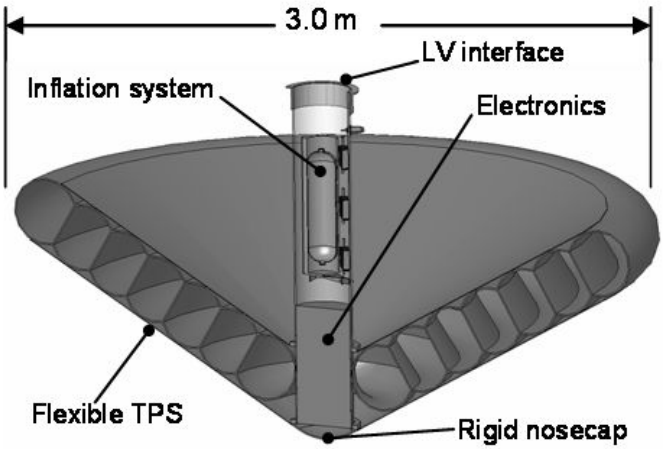

Figure 1-25: Schematic of IRVE vehicle [49].

Europe. AIR is considered inherently safe because it is designed to burn up in the upper atmosphere if inflation does not occur, and if it works properly the descent speed will be extremely low. The final configuration is to have a mass between 5 and 10 kg and have a terminal velocity of about 7 m/s. Kruijff et al. [60] outlines the evolution of the AIR design from a simple inflatable sphere to the inflated sphere-cone specified for the mission. Details and performance of the final configuration are provided in [88].

Numerous systems studies and tool development programs are supporting development of ballutes for aerocapture and entry. A majority of the recently-completed ballute work has been sponsored either through NASA's In-Space Propulsion (ISP) [52] or Exploration Systems Research and Technology (ESR&T) programs. A representative set of this technology development work is described here.

The ISP work is focused on a comparison of thin-film ballute aerocapture to rigid aeroshell aerocapture at Titan and Neptune for a 500 kg science payload. Current results are summarized in [86], and show that the payload mass fraction is significantly improved using thin-film ballutes. The mission profile uses ballute release (drag modulation) to control the exit conditions. The conceptual design study includes

aerothermal, packaging, structural, and trajectory analysis and identified no show stoppers. Limited wind tunnel testing has been performed on simplified models to verify analyses. Future planned work includes aeroelastic analysis, incorporation of tether aerodynamics and wind tunnel testing of inflated models.

Ballute research sponsored by the NASA ESR&T program focused on International Space Station down-mass, Earth return from the Moon and abort options for the Crew Exploration Vehicle [73, 22]. Direct entry, aerocapture into a low Earth orbit, and booster recovery were being considered. These analysis efforts incorporated integrated systems design, aeroelasticity, and materials evaluation. Wind tunnel testing in support of the analytic effort was also planned, but not completed.

With sufficient investment, the fidelity and accuracy of integrated analysis capabilities will continue to advance. Current capability includes static aeroelastic analysis in the supersonic continuum flight regime. CFD codes for entry and aerocapture applications with moving boundaries are being developed, and dynamic aeroelastic solutions along with flutter solutions will be available within five years in all flight regimes. If the current level of technology investment continues, a successful flight test of a clamped ballute will occur in the next five years. Under these same assumptions, the requisite analysis and hypersonic ground-based testing for a thin-film trailing ballute will also be completed, paving the way for flight test of this technology.

1.6 Summary

The concept of the ballute was first theorized in the early 1960's. Early proof-of-concept wind tunnel and drop tests demonstrated flutter failure of the ballute fabric upon deployment. Since these early tests, aeroelastic response of ballutes has been a concern to designers. Isotensoid and tension shell design were developed to eliminate surface wrinkles that fluttered and failed. This method proved effective for flutter failure, but other aeroelastic effects were observed during supersonic deployment and

flight that depended largely on geometry. While no tests have been performed in the hypersonic flight regime, hypersonic shock-tube tests and computational studies have shown that unsteadiness exists in the flow-field for some trailing ballute configurations at high Reynolds numbers. The unsteady flow-field coupled with the flexibility and low natural frequency of thin-film ballutes indicates that aeroelastic effects are likely important.

Flow computations validated against shock-tube test results indicate that aerodynamic tools exist for predicting unsteady flow in the hypersonic flight regime. Structural solutions using both explicit and implicit finite element analysis indicate that commercially available software tools are capable of accurately solving for the deformation and stress in thin-film structures. Coupled analysis has progressed to predicting static and dynamic solutions for fabric structures in the supersonic flight regime, but none have incorporated hypersonic high temperature effects or aerodynamics in the transitional and rarefied regimes.

This thesis will include solutions in all flight regimes applicable to thin-film ballute aerocapture. Creation of a variable-fidelity ballute aeroelastic analysis tool will allow designers to move from first-order assumptions to physics-based analysis of ballute aerocapture.

CHAPTER II

STUDY OBJECTIVES AND METHODS

In light of the flexibility, low natural frequencies, and potential for unsteady flow, credible aeroelastic analysis is required prior to flight of a thin-film ballute. Natural frequencies for trailing ballutes have been computed to be less than 1.0 Hz with deformation at peak dynamic pressure comparable to the minor diameter of the torus. Unsteady flow has been observed for trailing toroidal ballutes flying at high Reynolds number and for trailing spherical ballutes both computationally and experimentally. This combination of low frequency structural response and unsteady flow could result in a damaging aeroelastic response of the ballute. The remainder of this chapter discusses the analysis to be completed and the methods used in this investigation.

2.1 Study Objectives

This study will select the appropriate toolset for the flight environment and develop a variable-fidelity analysis tool for performing aeroelastic analysis of ballutes. The tool will use FEA for both high- and low-fidelity analyses, with grid density controlling the fidelity. The ballute aeroelastic analysis tool (BAAT), developed here, will be validated in a largely qualitative manner using available wind tunnel test data.

This thesis contains two studies using BAAT; one study that compares results using high- and low-fidelity aerodynamics at two points on a typical Titan aerocapture trajectory, and a second study that uses low-fidelity aerodynamics to demonstrate the design capabilities of BAAT.

The comparative study will use a high-fidelity structures model for both high- and low-fidelity aerodynamics solutions and will show the relative error of the low-fidelity aerodynamics at near-continuum conditions and near-rarefied conditions. It

is expected that the solutions will differ since the low-fidelity aerodynamics will not capture the complete physics (shock interactions will not be captured, altering the surface pressure distribution, and real gas effects will be approximated by using a modified ratio of specific heats equivalent to the reacting flow). The deformed shape, stress, and pressure distribution will be compared between low- and high-fidelity solutions.

The design capabilities of BAAT will be used to predict parameters of interest for a clamped ballute along a typical Titan aerocapture trajectory using the low-fidelity aerodynamics approach, suitable for conceptual design. Many points will be analyzed and the trends in drag, deformation, and stress will be shown. Furthermore, a first-order moving boundary aerodynamic method will be developed as part of the low-fidelity aerodynamics solution and used to predict if a clamped ballute would flutter.

2.2 Variable-Fidelity Analysis

Determining the deformed shape, stress, and drag of a flexible body using high-fidelity analysis is time consuming and computationally intensive. In the conceptual design phase, using high-fidelity tools to determine the drag for trajectory analysis is often not feasible, making low-fidelity analysis desireable. Low-fidelity analysis of some ballute geometries yields drag results within 15% of high-fidelity methods, indicating that low-fidelity analysis may be appropriate for conceptual mission analysis. Stress predictions, however, require high-fidelity analysis for accurate predictions. Since the maximum stress occurs at the peak dynamic pressure point of the trajectory, the high-fidelity analysis need only be run once, at the peak dynamic pressure point, to predict maximum stress.

Having both high- and low-fidelity analysis capabilities in one tool reduces the workload of the designer since the input files and structural grid are identical for

either analysis. Simply changing a flag in the input file selects either high- or low-fidelity analysis in any flight regime. The combination also allows stress, drag, and deformed shape prediction with minimum computation time for conceptual analysis of ballute missions.

2.3 Aeroelastic Analysis Modeling Philosophy

Aeroelastic analysis can be divided into loosely coupled methods [13] which allow use of existing codes with little or no modification, and monolithic or fully integrated methods [75] which require a complete code rewrite.

Loosely coupled methods typically use existing analysis codes, rely on input and output files for data transfer and don't necessarily exchange data at the end of each aerodynamic or structural dynamic analysis time step [14]. This allows for use of validated codes, block-substitution of other analysis codes, and simple coupling through the use of boundary conditions. This method is also modular and can be adapted easily for variations on the problem and advances made in each discipline's analysis. The primary disadvantage to this approach is the relatively large overhead for reading and writing input and output files. In addition, code tweaking is not possible for cases where source code is not available.

Monolithic methods start with the governing equations of the problem and solve them simultaneously using a custom built solution algorithm. This requires a reformulation of the governing equations for compatibility [12], and since the source code is typically written in-house, tweaking is possible but validation is much more difficult. Less time is spent passing data because all analysis codes are built together, but this also produces a numerically stiff problem which is often difficult to solve [40]. Development time is also longer due to the increased complexity of the program and the need to rewrite the analysis codes and solvers.

The loose coupling method has been chosen for this application due to time constraints, lower complexity, and the desire to use existing, validated disciplinary codes.

2.4 Analysis Codes

The design of thin-film ballutes requires structural dynamics and aerodynamics analysis in the rarefied, transitional and continuum regime. Existing tools were chosen where available to eliminate the need to fully validate each individual analysis code. For each code a text file interface and command line execution were used for ease of integration with the interface code. Alternatively, codes developed for this project can be run as sub-functions to the interface code, allowing data passing through memory.

2.4.1 Structural Analysis Code

The structural dynamics code needs to analyze geometrically non-linear deformation of thin polymer films and fabrics with thermal expansion, and temperature dependent, non-linear material properties. ABAQUS [1], ANSYS [10], and LS-DYNA [69] were investigated with LS-DYNA performing the best and producing consistent answers where other codes encountered numerical stability problems. Solutions to thin-film problems in LS-DYNA are straightforward, requiring few additional inputs to achieve stability. The resulting displacement, velocity, and acceleration are produced at the nodes. Temperatures and shear forces are input at nodes, while pressures are input at element face centers.

To ensure that the proper parameters are used in LS-DYNA for the coupled problem an inflated column buckling problem was solved and compared to experimental results published by Topping [117]. The experiment that most closely represents a thin-film ballute construction is a 0.0005 inch thick Mylar column inflated to 4.89 psi. Column geometry is shown in Figure 2-1. Two sets of material properties were provided and are shown in Table 2-1. The less stiff values are from estimates by Seide, Weingarte, and Morgan [107], while the stiffer values were experimentally measured

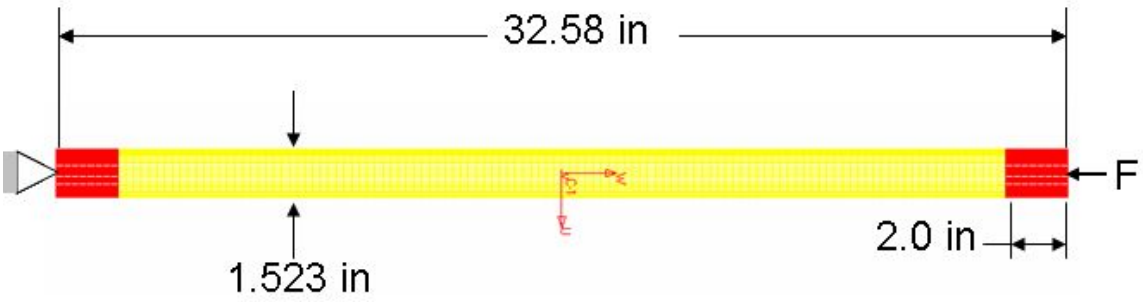

Figure 2-1: Inflated mylar column geometry.

Table 2-1: Mylar material data from test and estimation.

	Measured Properties	**Estimated Properties**
E (psi)	848,000	700,000
G (psi)	310,000	269,000
ν	0.3677	0.3010

for the buckling study. Computations were performed at both ends of the spectrum to show the variation in buckling load due to uncertainty in the material properties. Several element formulations and material models were used in LS-DYNA in an attempt to find the best modeling parameters for thin inflated membrane structures. Table 2-2 shows the options used and the resulting buckling load. Loading was applied via a prescribed displacement on the top of the column and simply constrained at the base. The load was output at every time step at the single constraint on the base of the column, and the peak load was considered the buckling load.

The buckling load from experiment was found to be 5.45 lb. by Topping and most of the element and material model combinations produced reasonable results. The notable exceptions are the membrane model using the elastic thermal (#4) or temperature dependent orthotropic (#23) materials. The linear isotropic model requires significantly less computational time than the elastic thermal material model, and the fabric model varies depending on the liner thickness. Due to the fast run time, the fabric model with 10% liner thickness is used when thermal effects are not being

Table 2-2: Material and element models in LS-DYNA and the corresponding buckling load. The element formulations examined are: Belytschko-Tsay (B-T), Hughes-Liu (H-L), slectively reduced H-L (S/R H-L), fast co-rotational H-L (fast, CR H-L), and Belytschko-Wong-Chiang (B-W-C).

Element Type	**Material Model**	**Material Props.**	**Compute Time (hrs)**	**Buckling Load (lb)**
Shell (B-T)	#1 Linear isotropic	Est.	4.4	5.35
Shell (B-T)	#1 Linear isotropic	Meas.	5.5	6.45
Memb. (B-T)	#34 Fabric (no liner)	Est.	8.2	5.39
Memb. (B-T)	#34 Fabric (10% liner)	Est.	4.7	5.36
Memb. (B-T)	#34 Fabric (20% liner)	Est.	8.5	5.36
Memb. (B-T)	#4 Elastic thermal	Est.	3.8	8.75
Shell (H-L)	#4 Elastic thermal	Est.	6.1	5.37
Shell (S/R H-L)	#4 Elastic thermal	Est.	32.5	5.36
Shell (B-T)	#4 Elastic thermal	Est.	4.2	5.28
Shell (Fast,CRH-L)	#4 Elastic thermal	Est.	6.0	5.28
Shell (B-T)	#23 Temp. dep. ortho.	Est.	5.0	5.28
Shell (Fast,CRH-L)	#23 Temp. dep. ortho.	Est.	6.5	5.28
Shell (B-W-C)	#23 Temp. dep. ortho.	Est.	6.1	5.28
Memb. (B-T)	#23 Temp. dep. ortho.	Est.	4.3	8.76

considered. The membrane element formulation produces excessively stiff buckling loads when used with non-fabric material models. The fabric model is not affected because LS-DYNA uses an element formulation for the fabric material model that includes a compressive strength model (but no moments). The linear isotropic model was run using both the measured and estimated material properties, and the buckling loads found bracket the experimentally determined buckling load, showing that the numerical solution is accurate within the material properties.

Buckling of an inflated torus due to radial loading was also tested. This model used the clamped ballute configuration to apply the radial load through a membrane. The results are compared to analytic results obtained by Weeks [124], and experimentally validated by Kyser [64]. The model cross-section is pictured in Figure 2-2. The torus has a major radius of 12.1m, a minor radius of 1.73m, a material thickness of 1.524x10-5m, a modulus of 88.26 MPa, and a Poisson's ratio of 0.25. Internal

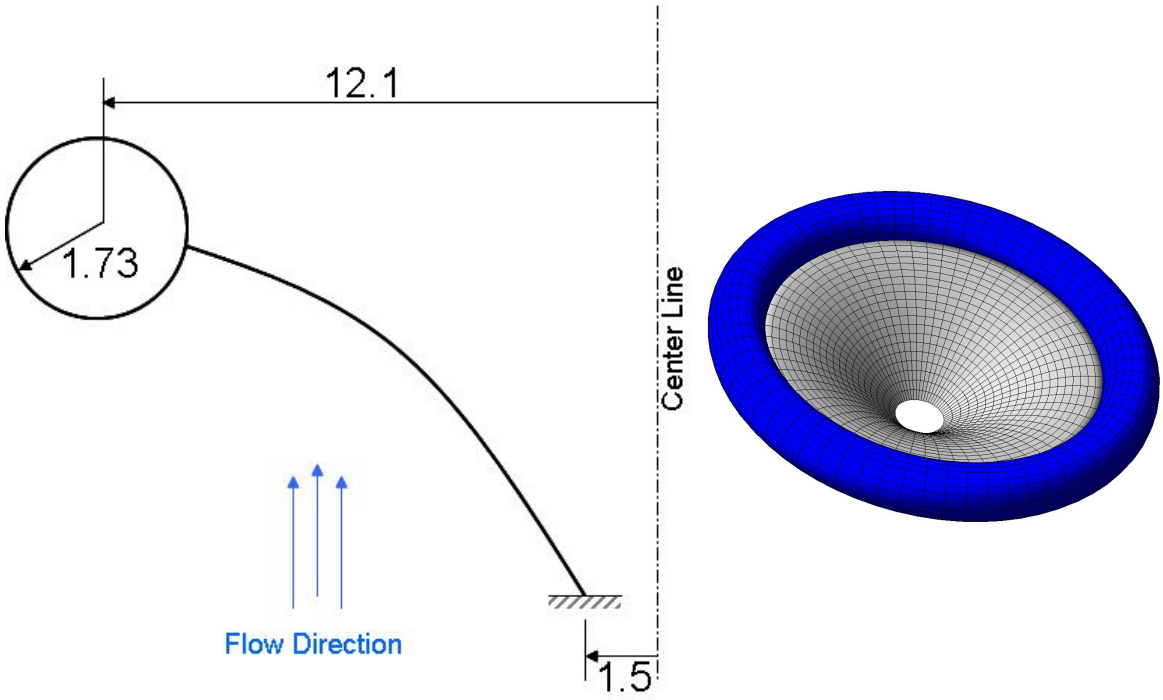

Figure 2-2: Cross-section of the torus model used for radial buckling calculations with dimensions in meters, and the revolved 3-D geometry.

pressure is 100 Pa and the distributed load is increased until buckling is observed as a drop in axial load carrying ability. The total axial load at the constraints was used to determine the membrane tension and the distributed radial load acting on the torus. This method was used because the model already existed and it provides a good approximation to a true radial loading.

Loads for three different buckling modes were calculated based on the equations provided by Weeks and Kyser:

$$\begin{aligned} \text{In-plane} &= 40 \text{ N/m} \\ \text{Out-of plane} &= 21 \text{ N/m} \\ \text{Crippling load} &= 940 \text{ N} \end{aligned}$$

The in-plane buckling mode is characterized by a physical collapse of the torus as four hinges and four arcs as shown in Figure 1-13. The out-of-plane mode is a curling of the torus that does not result in a loss of load carrying ability, and the crippling load

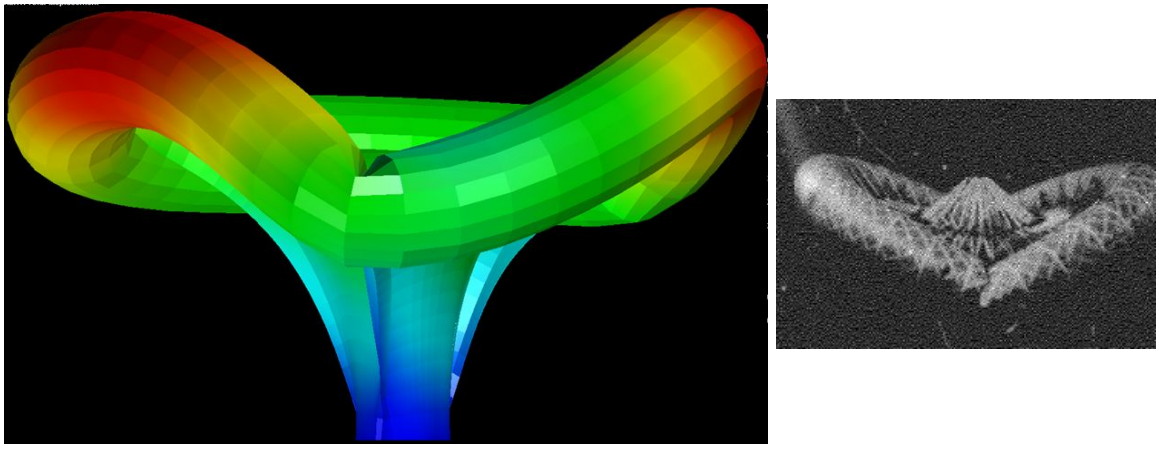

Figure 2-3: The computed deformed shape of a torus at its buckling load compared to experimental results from [64].

is the point at which the circumferential load in the torus exceeds the load due to the internal pressure in the torus and is characterized by the torus folding, out-of-plane, on a single hinge-line. The load at which buckling occurred in the LS-DYNA model was 38 N/m radial load, and a circumferential load of 720 N. The deformed geometry is shown in Figure 2-3 at the buckling load. The radial load is just 5% less than the predicted in-plane buckling load. The circumferential load is significantly less than the crippling load, though the deformed shape at buckling is more indicative of the crippling mode. This is believed to be due to slight differences in the load application method between the experiment and the numerical solution.

2.4.2 High-Fidelity Aerodynamics Codes

Continuum aerodynamics will be calculated by NASCART-GT [72, 118] which is capable of handling hypersonic flow. Navier Stokes, Euler, or modified Newtonian equation sets are available. This problem will use NASCART-GT to solve the Euler equations using a constant ratio of specific heats. By neglecting viscosity in the solution, the effects of viscous interaction are neglected, and proper surface heating calculations are not possible. The lack of flow chemistry increases the shock stand-off distance in this computation. NASCART-GT can run on multiple processors for

static grid cases, and uses a Cartesian grid and the only required geometric input is a triangulated surface. Surface pressure data is ouput at cell centers and values are mapped back to quadrilateral elements for input to LS-DYNA.

DAC [65] will be used for the rarefied and the transitional aerodynamics, and was obtained from the Technology Transfer & Commercialization Office at NASA Johnson Space Center. The code is based on the Direct Simulation Monte Carlo method of Bird [15]. Flow chemistry is available if reaction equations are provided, but will not be used for this problem. The DSMC method produces good solutions for any flow speed with high Knudsen number. DAC uses a Cartesian grid method with manually driven grid refinement based on the cell size to mean free path ratio. Results are available as either surface element or node based data.

The cartesian grids used in both high-fidelity aerodynamics codes completely automate the grid generation process, simplifying the coupling process. Prior to executing coupled analysis the appropriate parameters determining grid density and outer boundaries must be determined for the specific case being executed. These grid studies will be presented for each geometry used in this dissertation.

2.4.3 Low-Fidelity Aerodynamics Codes

Due to the long computation time required by both NASCART-GT and DAC, a simplified set of aerodynamic tools is also being employed. A computer program, referred to as the Moving Boundary Simple Aerodynamics (MBSA) code has been developed, and encompasses all of the methods presented in this subsection.

In the rarefied regime the collisionless DSMC method of Bird is used [15].

$$\begin{aligned}\frac{p}{p_\infty} &= \left[(1+\epsilon)\pi^{-1/2}s\sin\Psi + \frac{1}{2}(1-\epsilon)\left(\frac{T_r}{T_\infty}\right)^{1/2}\right]\exp(-s^2\sin^2\Psi) \\ &+ \left[(1+\epsilon)(\frac{1}{2}+s^2\sin^2\Psi) + \frac{1}{2}(1-\epsilon)\left(\frac{T_r}{T_\infty}\right)^{-1/2}\pi^{1/2}s\sin\Psi\right][1+\mathrm{erf}(s\sin\Psi)]\end{aligned} \tag{2-1}$$

$$\frac{\tau}{p_\infty} = \pi^{-1/2}(1-\epsilon)s\cos\Psi\left[\exp(-s^2\sin^2\Psi) + \pi^{1/2}s\sin\Psi\left(1+\mathrm{erf}(s\sin\Psi)\right)\right] \quad (2\text{-}2)$$

$$\frac{\dot{q}s^3}{h_\infty} = \frac{(1-\epsilon)}{2\pi^{1/2}}\left[s^2 + \frac{\gamma}{(\gamma-1)} - \frac{(\gamma+1)}{2(\gamma-1)}\frac{T_r}{T_\infty}\right]\left[\begin{array}{l}\exp(-s^2\sin^2\Psi)+\\ \pi^{1/2}s\sin\Psi\left(1+\mathrm{erf}(s\sin\Psi)\right)\end{array}\right] \quad (2\text{-}3)$$
$$- \frac{(1-\epsilon)}{2\pi^{1/2}}\frac{1}{2}\exp(-s^2\sin^2\Psi)$$

Equations 2-1 to 2-3 for pressure, shear, and heat rate were implemented, by this author, in MBSA and verified against DACFREE [129], a code authored by Dick Wilmoth of NASA Langley which uses the same equation set. The resulting drag, using diffuse reflection at the boundary (ϵ), of the ballute over the velocity range from 4 to 12 km/s does not differ by more than 1 N relative to the DACFREE solution for flight conditions on the ballute trajectory at Titan. This slight variation is likely due to differing implementation details including a switch from single to double precision.

The Modified Newtonian method [6] is used for static cases in the continuum regime. The surface pressure is computed knowing the Mach number and flow incidence angle.

$$C_p = C_{pmax}\sin^2\Psi \quad (2\text{-}4)$$

$$C_{pmax} = \frac{2}{\gamma M_\infty^2}\left\{\left[\frac{(\gamma-1)^2M_\infty^2}{4\gamma M_\infty^2 - 2(\gamma-1)}\right]^{\gamma/(\gamma-1)}\left(\frac{1-\gamma+2\gamma M_\infty^2}{\gamma-1}\right) - 1\right\} \quad (2\text{-}5)$$

The continuum regime heat rate is calculated using Sutton and Graves' equation for the stagnation point [112] with decrease away from the stagnation point that follows a sine of the flow incidence angle function [113].

$$\dot{q}_{cont} = k_{heat}\sqrt{\frac{\rho_\infty}{R_n}}V_\infty^3\sin\Psi \quad (2\text{-}6)$$

Table 2-3: Optimized bridging function variables.

Parameter	Optimized Value
B	0.436
m	3.044
Kn_{upper}	3.044
Kn_{lower}	0.00049

Here k_{heat} is an atmosphere dependent constant, taking the value 1.2676x10^{-4} for Titan, 1.7415x10^{-4} for Earth, and 1.9027x10^{-4} for Mars, and R_n is the effective nose radius of the body. The simplified methods produce face-centered results for pressure, shear, and heat rate.

Once the rarefied and continuum limits have been calculated, the transitional regime aerodynamics are computed using a bridging function [130] of the form:

$$C_{p,bridge} = C_{p,cont} + (C_{p,fm} - C_{p,cont}) \sin^2 \left(\pi \left[B + \left(\frac{1}{2} - B \right) \log_m(Kn) \right] \right) \quad (2\text{-}7)$$

Here B and m are found by fitting the CFD and DSMC results calculated by Peter Gnoffo and Richard Wilmoth of NASA Langley Research Center for the toroidal trailing ballute at varying flight conditions along a Titan aerocapture trajectory [87]. Coefficients were found that minimized the square of the difference between the bridging function and the actual results. The continuum and rarefied limits were also allowed to vary. The results are shown in Figure 2-4, where the optimized bridging function is shown in red, the continuum and rarefied limits are dashed lines, and the CFD and DSMC solutions are square and triangle symbols respectively. The resulting values for B, m, and the bounds are presented in Table 2-3. Of note is the low value of the continuum limiting Knudsen number which is 0.00049, lower than the typical limit of 0.001 [91].

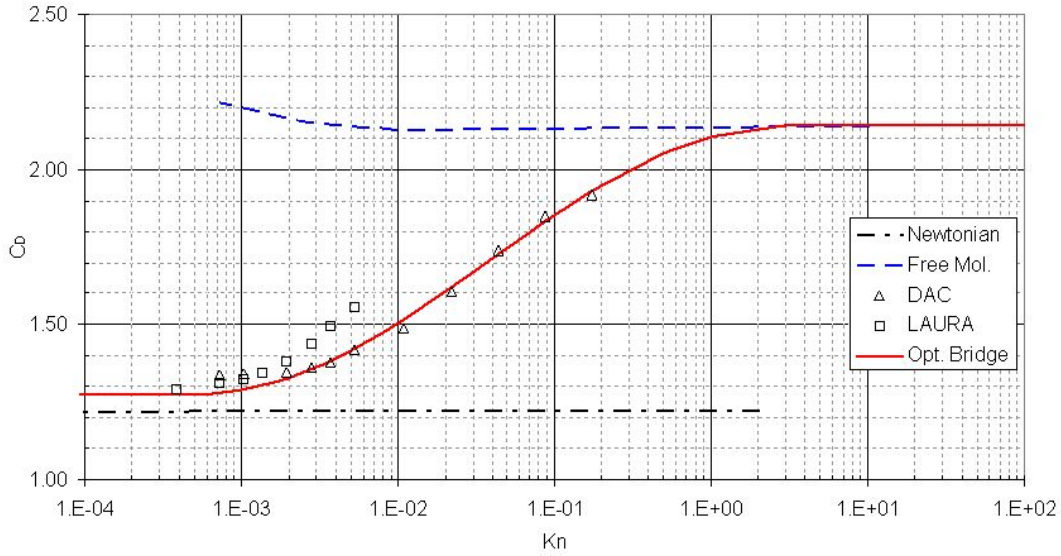

Figure 2-4: Detailed computational results for a toroidal trailing ballute with an optimized bridging function showing the continuum and rarefied drag values.

2.5 Boundary Condition Mapping

Coupling the analysis codes requires a scheme for transferring boundary condition data between the disparate analyses and, over time, the coupling scheme needs to introduce as little error as possible so that energy is not artificially dissipated, causing an increased flutter boundary velocity.

LS-DYNA uses primarily four-node shell elements while DAC and NASCART-GT require a pure three-node shell element input. Both DAC and NASCART-GT only require surface resolution from the input grid, which can be satisfied by simply splitting the four-node elements from the LS-DYNA input. Unfortunately, NASCART-GT has proven unable to handle the high number of input cells required by the structures model, necessitating a second, coarser grid.

To couple LS-DYNA with DAC, the mixed triangular-quadrilateral grid used for structural analysis is split into a pure triangular grid. Since both the LS-DYNA and DAC grids use the same nodes, transfering displacement data is straightforward. Transfering pressure data from the aerodynamic grid to the structural dynamic grid

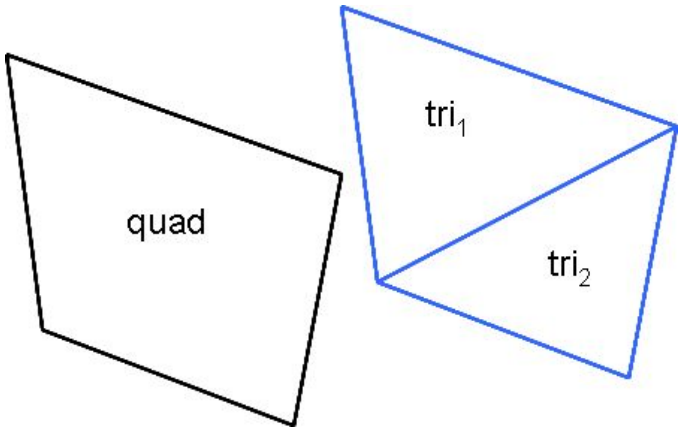

Figure 2-5: Nomenclature for area weighted pressure averaging between the triangular aerodynamics grid and quadrilateral structures grid with matching nodes.

requires area weighted averaging from two three-node elements to a single four-node element. Pressure transfer uses Equation 2-8, with nomenclature illustrated in Figure 2-5.

$$P_{quad} = \frac{P_{tri_1} A_{tri_1} + P_{tri_2} A_{tri_2}}{A_{tri_1} + A_{tri_2}} \tag{2-8}$$

Here, A is the area of a triangular element, and P is the pressure on the element specified by the subscript. This method ensures that total force magnitude is conserved when boundary data is transfered, but does not necessarily match force direction. Force direction should be close since the quadrilateral element should not twist very much in the structural analysis, and there is no way to match direction using pressure loading.

Coupling LS-DYNA with NASCART-GT requires that the triangular aerodynamic grid be coarsened when the structural grid is large, which is the case for the analysis presented in Section 4.4.1. Since the structural grid is produced by rotating a set of nodes about an axis, the coarse aerodynamic grid is coarsened by using every fifth node in the radial and cicumferential directions of the structural grid. Since nodes match between the two models, transfering displacement data only requires knowledge of the matching node numbers. For transfering pressure data,

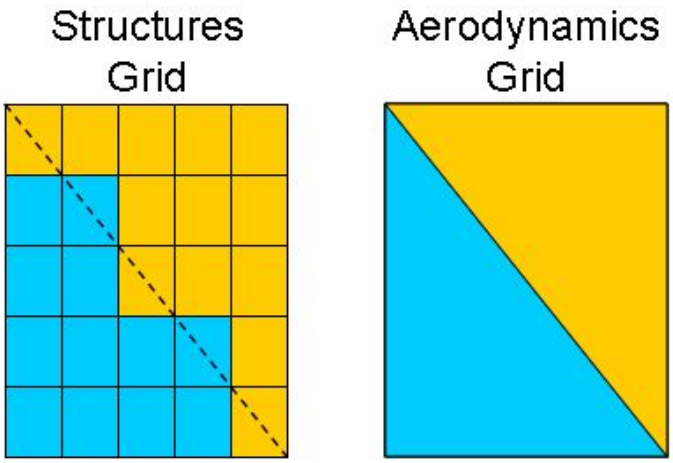

Figure 2-6: Element mapping for pressure load transfer between the coarse NASCART-GT grid and the fine LS-DYNA grid.

structural elements are mapped to aerodynamic elements by proximity of the quadrilateral element centroid to the larger triangular element's centroid. For simplicity, no interpolation or element cutting is performed when mapping elements. For a curved geometry, this leads to elements on the diagonal mapping to the triangle element with larger radius. A simple example of the element mapping for pressure transfer is shown in Figure 2-6. In theory this leads to a bias towards the pressure of triangular elements at a larger radius, but in practice the difference in pressure between these two triangles is very small since NASCART-GT is interpolating pressure data from a cartesian grid back to the triangular input grid, and the elements are small compared to the geometric features of the model.

2.6 Applicability and Extension of BAAT

The Ballute Aeroelastic Analysis Tool (BAAT) incorporates the methods of data transfer described in Section 2.5 and the time coupling method of Section 5.3.2. BAAT is a coupling code, and can be used to solve any problem that requires iteration between aerodynamics and structural dynamics. Data is transferred between LS-DYNA and one of the three aerodynamics tools previously described: MBSA,

NASCART-GT, or DAC, which were chosen for their applicability to analysis of thin-film ballute aerocapture. Despite this, BAAT and the coupled codes are capable of solving other coupled problems that can be modeled using LS-DYNA and MBSA, NASCART-GT, or DAC. LS-DYNA is capable of most three-dimensional structures problems, and the aerodynamics codes span the velocity and density range. Some other possible uses of BAAT include:

- Coupled analysis of iflatable aerodynamic decelerators constructed of heavier materials in the supersonic or subsonic flight regimes,
- Aeroelastic analysis of flow around micro electro mechanical devices, utilizing DAC for the low Knudsen number flow,
- Flutter of aircraft wings using Piston theory, which is implemented in MBSA.

Other applications exist that utilize the current capabilities, and extension of BAAT to use other coupled codes is possible. BAAT is written in a modular way, using classes in C++, to facilitate future extensions and code upgrades.

2.7 Contributions

This thesis develops a variable-fidelity aeroelastic analysis capability for thin-film ballute aerocapture and applies it to a representative ballute trajectory. The following summary lists the contributions of this research.

First hypersonic aeroelastic solution for a thin-film ballute using inviscid perfect gas aerodynamics: To date, no thin-film ballute aeroelastic solutions in the hypersonic flight regime have been published for either static or dynamic analysis. This thesis will produce static aeroelastic solutions, using non-linear structural analysis and inviscid perfect gas fluid dynamic analysis, for a representative ballute aerocapture trajectory. Grid convergence will be demonstrated for both the structural and aerodynamic models used in the analysis. Static deformed shape, drag,

and stress level will be predicted at many points along the representative aerocapture trajectory to demonstrate the utility of the tool for drag performance and static stress prediction. This will eliminate uncertainty in the ballute design process and help ballutes move towards flight test.

A variable-fidelity hypersonic aeroelastic analysis tool for thin-film ballutes: In addition to performing analysis, this research will produce the Ballute Aeroelastic Analysis Tool (BAAT) that can be used to solve general coupled design problems in the continuum, transitional, and rarefied flight regimes at hypersonic speeds. Coupling of structures and either high- or low-fidelity aerodynamics is fully automated, and requires only a structural grid and input files. BAAT will be validated using wind tunnel tests of flexible models performed by the ISP program. Use of BAAT will allow ballute designers to move from assuming that aeroelastic effects will not be damaging, to actually analyzing thin-film ballutes on aerocapture trajectories with physics-based methods.

A first-order, unsteady, hypersonic aerodynamics & moving boundary aerodynamics tool: The most common high-speed, unsteady aerodynamic tool used in aeroelastic analysis is Piston theory, which is not applicable to blunt bodies at flow Mach numbers in the aerocapture regime. An engineering approximation has been developed as an addition to modified Newtonian analysis to include a first-order estimate of damping due to the fluid. This unsteady, hypersonic aerodynamics approximation provides a rapid dynamic aeroelastic analysis method in the hypersonic, continuum flight regime for blunt bodies, that is suitable for conceptual design.

CHAPTER III

AEROELASTIC VALIDATION USING THE ISP WIND TUNNEL TEST MODEL

Validation of thin-film structures in a hypersonic flight condition is difficult due to the limited data available. To date, only two relevant tests have been performed, and only one provided deformation profiles. The first test aimed to demonstrate that a thin-film polymer could survive hypersonic flight conditions and obtain deflection measurements of the membrane under load. The second test acquired qualitative temperature data on the membrane surface and would have provided quantitative temperatures profiles, but testing and calibration was cut short due to funding issues. Because of these test limitations, a largely qualitative validation is performed in this chapter.

3.1 Geometry and Flight Conditions

Both tests were performed at the NASA Langley Research Center as part of NASA's In-Space Propulsion (ISP) program [20]. The first tests used both the hypersonic CF_4 tunnel and the 31 inch Mach 10 Air tunnel, and the second test only used the Mach 10 Air tunnel. This validation study selected run 15 (6 inch diameter model, 1 mil Kapton membrane, CF_4 tunnel) from the first set of tests because it is the most flexible model tested, the shock structure is visible in the available photograph, and the dynamic pressure and heat rate are low. The low dynamic pressure should minimize thermal effects on material properties in these results, providing a better deformed shape validation opportunity.

A clamped ballute configuration was tested, and was comprised of a rigid nose

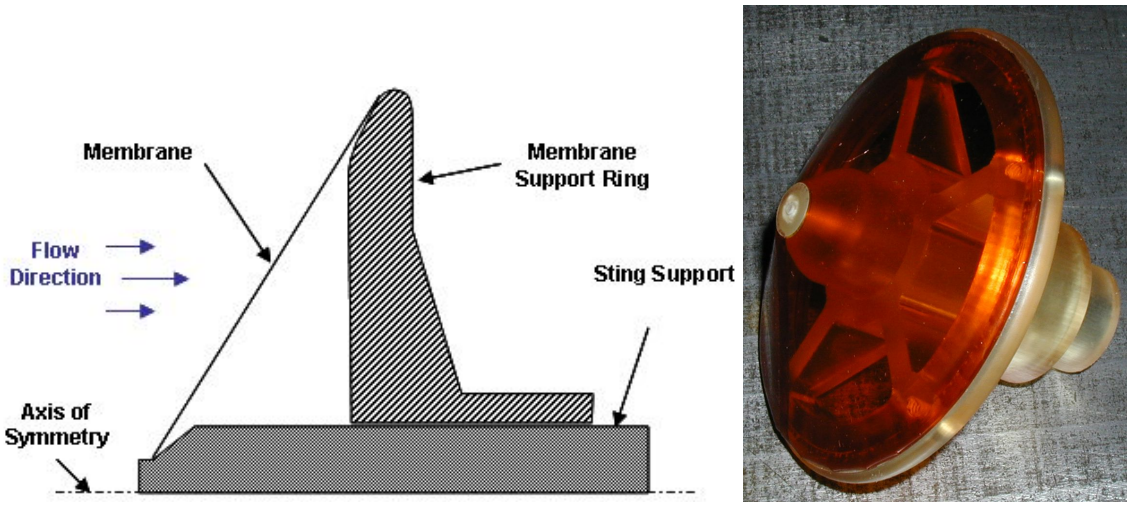

Figure 3-1: A cross section of the CF_4 wind tunnel test model prior to testing. Notice that the outer membrane support can move axially along the sting [20].

and rigid outer support with a membrane streched between. The outer support was allowed to float axially to allow for the axial deformation expected in flight. The outer diameter of the model was 15.24 cm and the rigid nose diameter was 1.3 cm. Figure 3-1 shows the test model prior to testing. The membrane is constructed of 0.254 mm (0.001 in.) thick Kapton and forms a 60 deg. half angle cone with one seam. During testing the seam was placed on the opposite side of the model from the camera so as to have the smallest affect on the results possible. Deformation data is from photographs of the model during testing, and no dynamic data is available. Figure 3-2 shows an example photograph of the deformed profile during testing and the wrinkle pattern observed after testing. Because membrane deformation remains after the loading is removed one or more of creep, plasticity, or thermal setting phenomenon take place in the test model. None of these effects are captured in the computational analyses and so exact deformations cannot be reproduced, but qualitatively the deformed shape should be similar. Unfortunately, the model deforms further during the cooling process, so post-test photographs cannot be used to generate quantitative deformation profiles.

Figure 3-2: The CF_4 wind tunnel test model during testing (left) and after testing (right) [20].

Table 3-1: ISP CF_4 wind tunnel test conditions and clamped ballute flight conditions at peak dynamic pressure at Titan.

Parameter	**CF_4 Test**	**Clamped Ballute at Peak q on titan**
Dynamic Pressure (Pa)	654.0	51.5
Atm. Density (kg/m^3)	1.46x10^{-3}	5.66x10^{-6}
Atm. Temperature (K)	254.0	166.4
Velocity (m/s)	945.0	4226.4
Sonic Speed (m/s)	168.0	259.9
Mach number	5.6	16.4

The test conditions are in the hypersonic flight regime, but do not match any specific point on a calculated ballute aerocapture trajectory at Titan. Table 3-1 shows the test conditions and the flight conditions of a clamped ballute at peak dynamic pressure along a typical Titan ballute aerocapture trajectory. The test conditions have a higher dynamic pressure than the calculated ballute trajectory leading to larger forces on the test model. The larger aerodynamic force counters the higher stiffness of the test model compared to the flight article due to unavailability of Kapton less than 0.254 mm thick. The wind tunnels are not capable of matching the flight conditions exactly, but were run as close as possible to their limits while still ensuring correct results. The test Knudsen number is 0.00046, which is within the continuum regime, making this a useful validation case for the modified Newtonian method and NASCART-GT.

The test membrane is constructed of Kapton and was estimated to be at 260°C by the test engineer (Greg Buck of NASA Langley). Experimental data for the modulus of elasticity is available at 23°C, 200°C and 500°C and was linearly interpolated to obtain the value at 260°C. At the estimated temperature the modulus is 1.479 GPa and the poisson's ratio is 0.34 [27]. Due to the lack of temperature data from the test, the surface temperature is assumed to be uniform over the membrane.

3.2 Structural Model & Grid Convergence Study

A finite element model was created of the wind tunnel test article using quadrilateral elements. Only one quarter of the model was used for computation due to the global symmetry of deformation and the local wrinkling of the surface. The membrane is modeled using the fabric material model with a 10% liner and the nose and aft support ring are assumed to be rigid. The model is fully constrained from the nose, and the aft ring is constrained radially.

The base model has 12 circumferential and 10 radial elements to simulate one

quarter of the membrane, resulting in a fairly coarse model. Four different refinement levels were made that increase the number of elements used to simulate the membrane from 120 up to 4,992. Several solution metrics were tracked, including the number of surface wrinkles formed, the maximum principle stress, and the maximum axial deflection. Surface wrinkles are important in this model because they indicate buckling of the membrane due to a compressive stress in the hoop direction. Stroud and Zender [110] showed experimentally that conic shaped shells buckle in the circumferential direction under a uniform pressure load. Figure 3-3 shows the deformed grid on each model and the number of elements used to model the membrane. For the finest grid, the number of circumferential elements is doubled as you move from the spacecraft outward. This was done to keep the minimum edge length at a reasonable size since smaller edges require small timesteps and produce long run times. The structural models were run until a steady state was reached with a uniform pressure applied to the membrane (not coupled to aerodynamic analysis). Figure 3-4 shows that the Fine and XFine models have converged for both axial deflection and principle stress, but the number of wrinkles continues to bounce between 3 and 4. The variation in number of wrinkles between 3 and 4 does not appear to impact the displacement or stress significantly, and is likely due to the use of a quarter model. The angle between the wrinkles is approximately the same in the Fine and XFine models, indicating that the orientation relative to the quarter model has changed, but the number of wrinkles in a full model is the same. Further computations will use the Fine model.

3.3 Coupled Low-Fidelity Aerodynamics Solution

The low-fidelity aerodynamic code assumes a perfect gas. GasEQ [89] was used to determine the equilibrium flow properties of CF_4 at the freestream temperature of 254 K. The resulting ratio of specific heats is 1.176 and the gas constant is 94.47 J/kg-K. The coupled code was run for 6.5 sec. (13 iterations) at which point the solution had

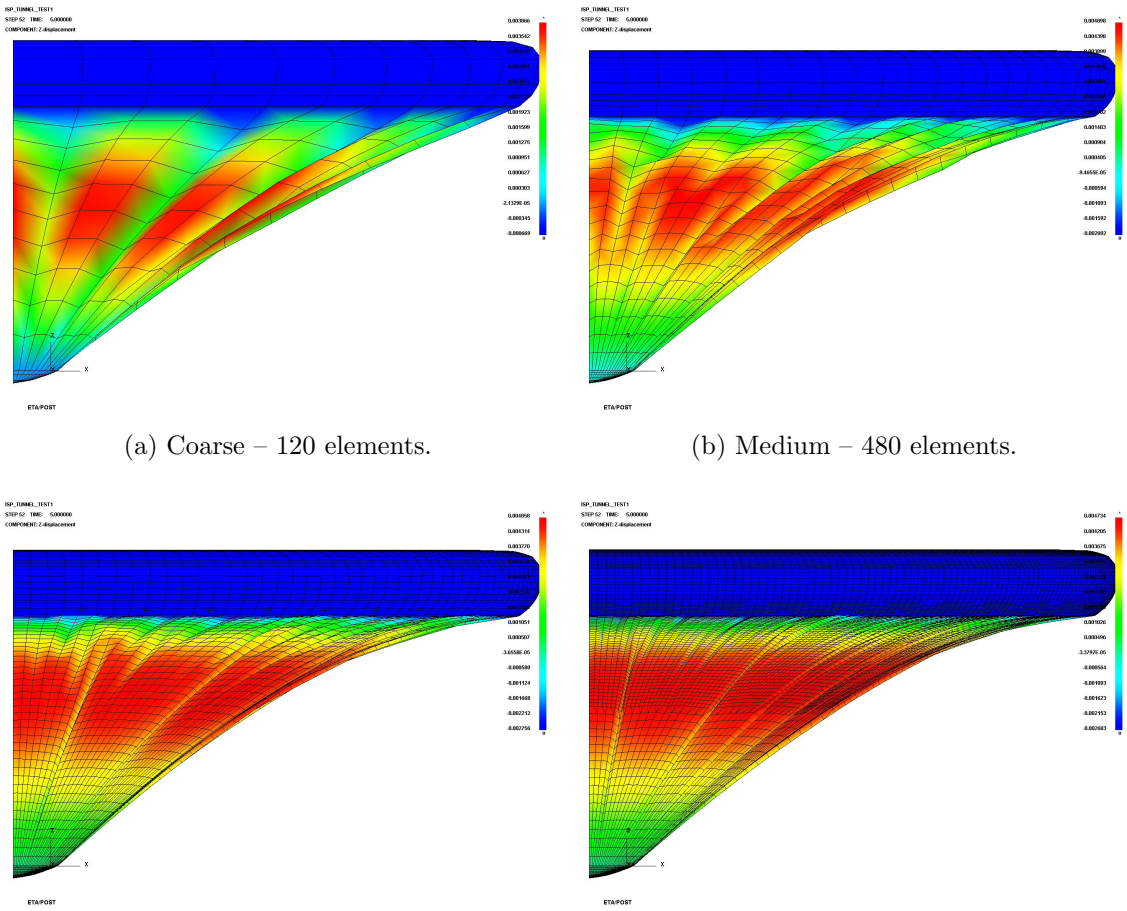

(a) Coarse – 120 elements.

(b) Medium – 480 elements.

(c) Fine – 1,920 elements.

(d) XFine – 4,992 elements.

Figure 3-3: Grids used in the convergence study of the ISP wind tunnel test model, red indicates larger displacement.

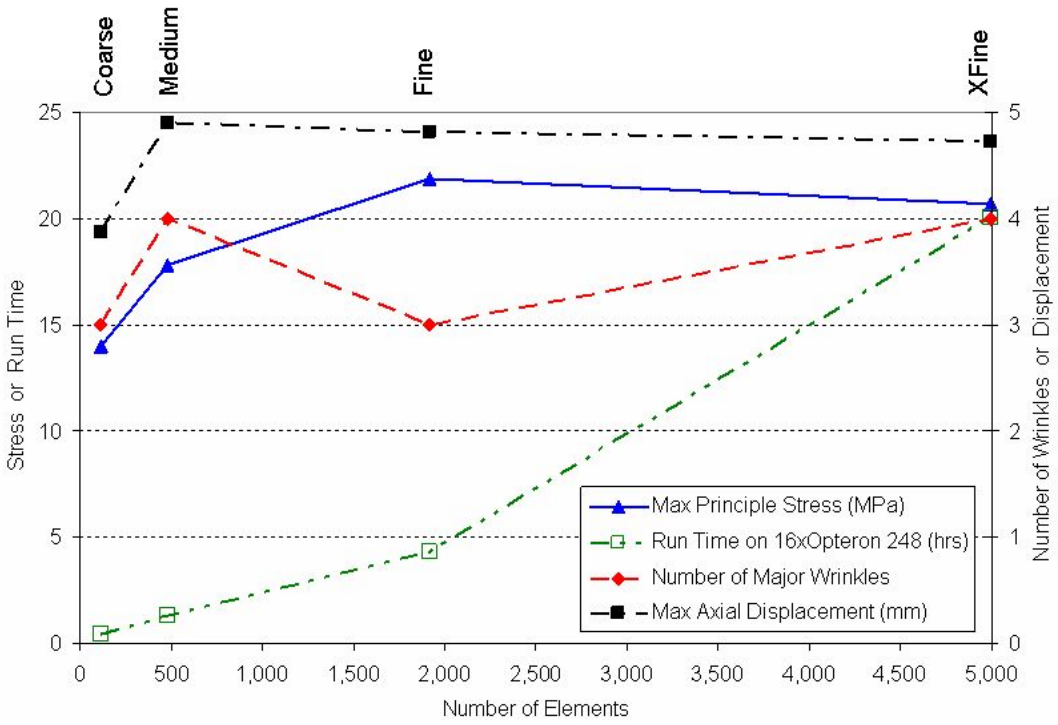

Figure 3-4: Solution metrics as the structural grid is refined. Run time is on 16 Opteron 248 processors.

reached a steady state. The resulting deformed shape is shown in Figure 3-5 with surface pressure contours. The quarter model used for computation was reflected twice to produce a complete model for visualization purposes. The large surface wrinkles observed in test (Figure 3-2) are present, but the minor wrinkles between each major wrinkle are not as prominent. Figure 3-6 shows that the membrane contour matches well, within 0.3% for the inner third and within 3% for the outer third of the model where the floating support ring has moved forward in the computation and backwards in the experiment. This difference indicates that the material must have a lower modulus (higher temperature) or expand substatially due to thermal effects. Membrane deformation in the experiment was hampered by interference with the support structure of the aft ring, but this is not expected to cause such a substantial difference in aft ring movement.

The discrepancy between the computed and experimental profiles in Figure 3-6 is

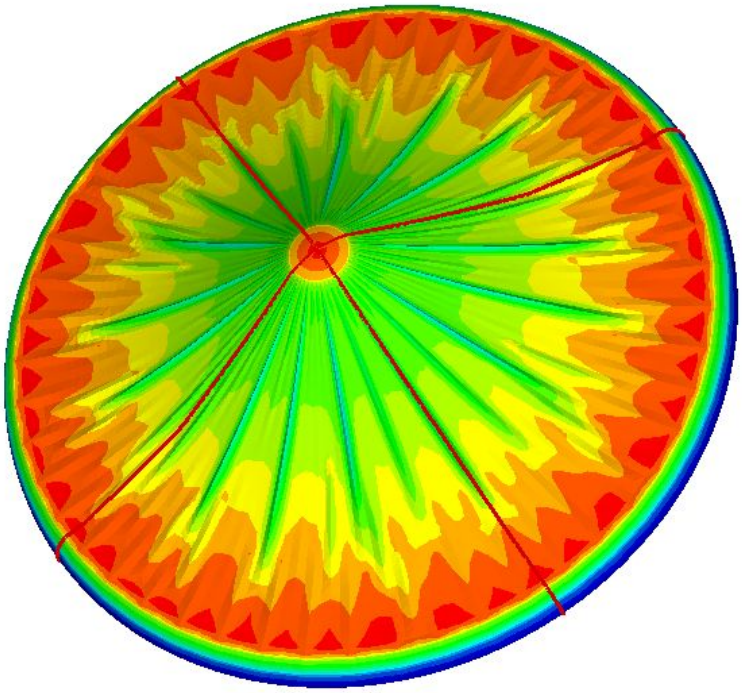

Figure 3-5: Static coupled solution, with low-fidelity aerodynamics, of the ISP wind tunnel model with surface pressure contours. Red indicates higher pressure, more blunt surfaces and the dark red lines are reflection boundaries.

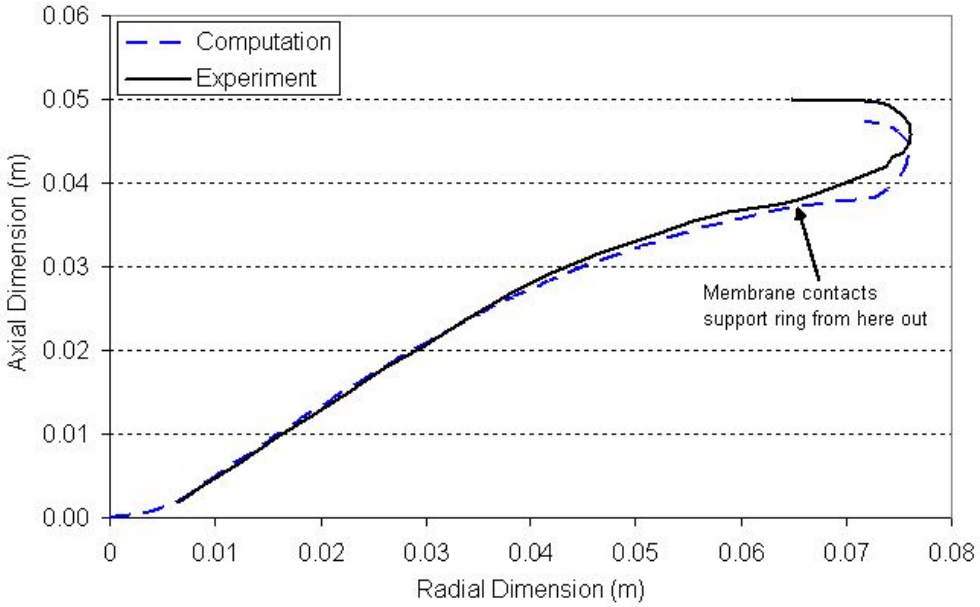

Figure 3-6: Radial profile of the static coupled solution of the ISP wind tunnel model.

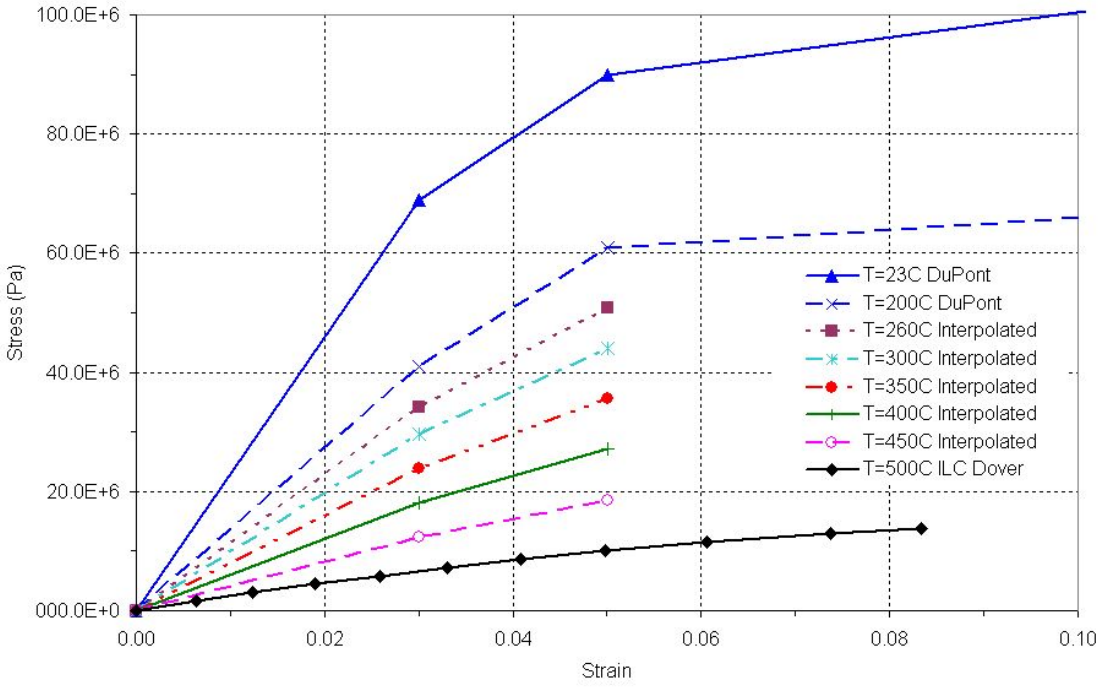

Figure 3-7: Kapton 30HN stress-strain relation at various temperatures.

likely caused by incorrect material properties, incorrect pressure distribution, or thermal expansion. The pressure distribution produced by the low-fidelity aerodynamics does not take into account the complex shock structure observed around the body that will be addressed by using high-fidelity CFD analysis in the following section. Incorrect material properties could be due to either material nonlinearity or an incorrect estimate of the material temperature. Stress-strain profiles for Kapton 30HN at 500°C, 260°C, and 23°C are shown in Figure 3-7. ILC Dover provided the data at 500°C and the data at 200°C and 23°C is from DuPont product literature [26]. The peak stress calculated for the test model is 22 MPa, which falls in the linear region of the stress-strain curve at both 23°C and 200°C. Curves are interpolated between 200°C and 500°C to estimate that the calculated peak stress of 21 MPa is still within the linear range of this material up to about 425°C. Due to the linear nature of the material in the temperatures explored, material nonlinearity does not account for the

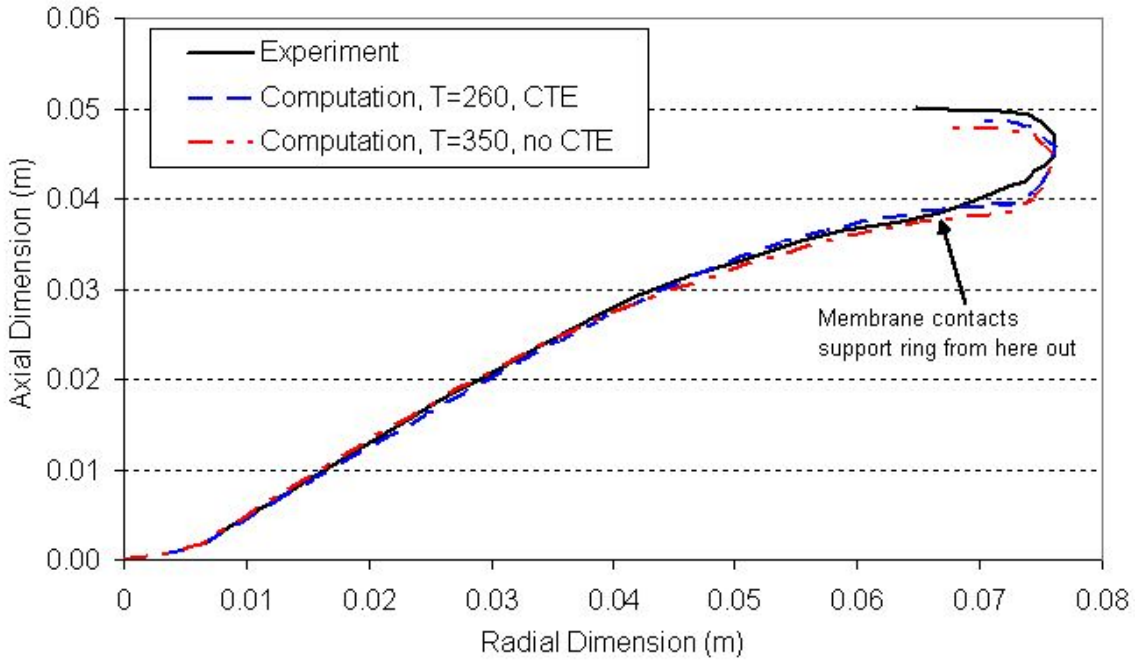

Figure 3-8: Radial profile with T=350°C, and T=260°C with thermal expansion.

discrepancy.

Models were run at 350°C without thermal expansion and at 260°C with thermal expansion. Figure 3-8 shows the radial profile of these two cases. The addition of thermal expansion causes the support ring to move aft, but not quite as far as the experiment. Even without thermal expansion, increasing the temperature to 350°C allows the support ring to move aft, but not as much as the addition of thermal expansion. From these two results it appears that some combination of thermal expansion and increased temperature will result in a nearly perfect match to experiment. Unfortunately, due to the interference of the aft support ring at a radius of approximately 0.065 m in the test, the computation will not precisely match the experiment in this region (since the computational model does not include contact and the internal support structure geometry is not known).

Trial and error was used to determine the proper temperature required to match the experimental data. Figure 3-9 shows the profile with the best fit, which includes

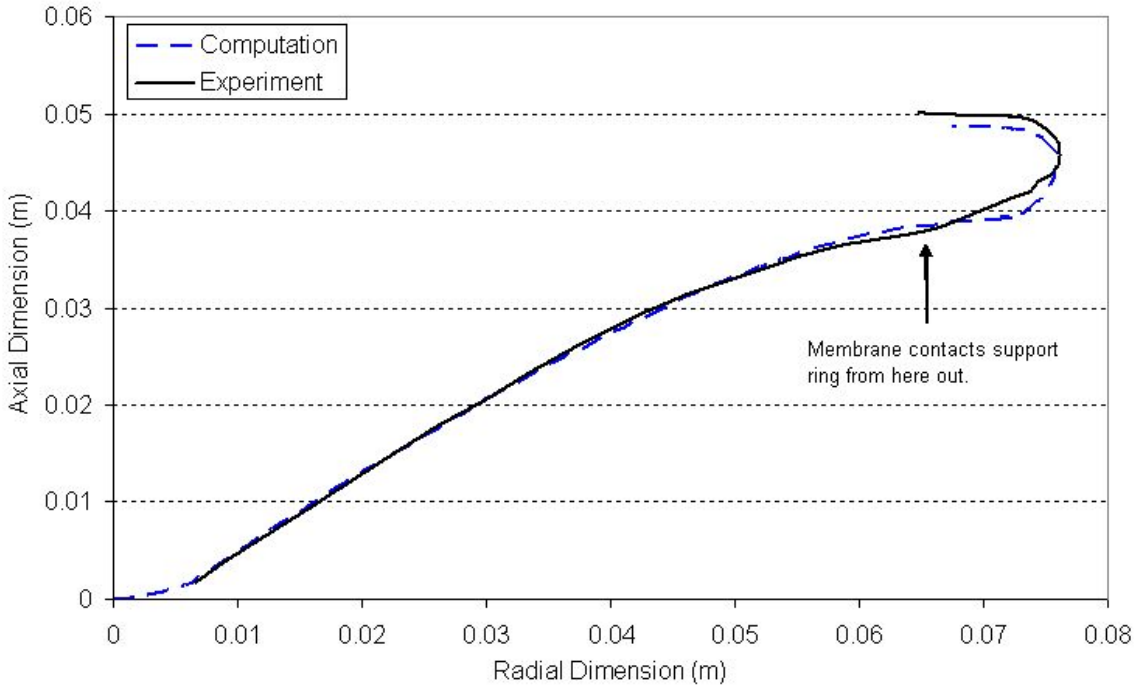

Figure 3-9: The best computational solution includes thermal expansion at 300°C.

thermal expansion at a temperature of 300°C. Increasing the temperature beyond 300°C did not increase the deflection of the aft ring, but instead caused excessive deflection of the membrane.

3.4 Coupled High-Fidelity Aerodynamic Solution

High-fidelity analysis was performed by coupling NASCART-GT to LS-DYNA. Preliminary grid studies were performed with NASCART-GT to determine the necessary grid resolution. Coupled analysis was then run with the best grid resolution for both NASCART-GT and LS-DYNA.

3.4.1 NASCART-GT Grid Convergence Study

Grid studies in NASCART-GT were performed using the deformed geometry from the wind tunnel tests. The profile used was taken from the photograph used for shock structure comparison in the left half of Figure 3-11. A three-dimensional grid was generated by sweeping the experimentally determined deformed profile 90° to form

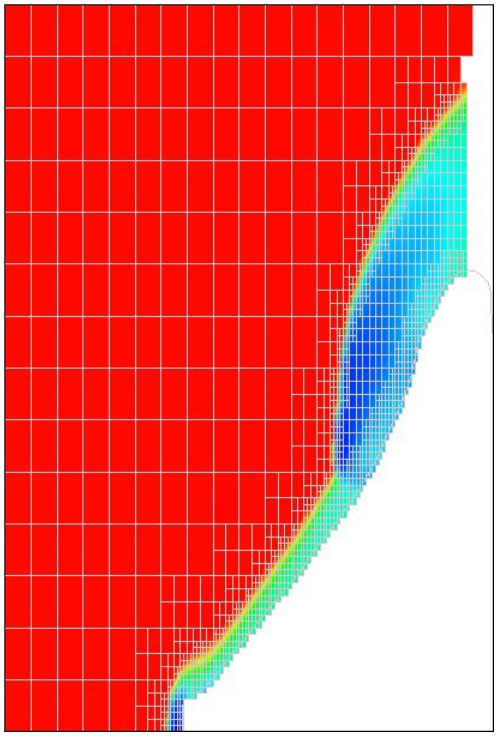

(a) C1 – 39,967 surface cells.

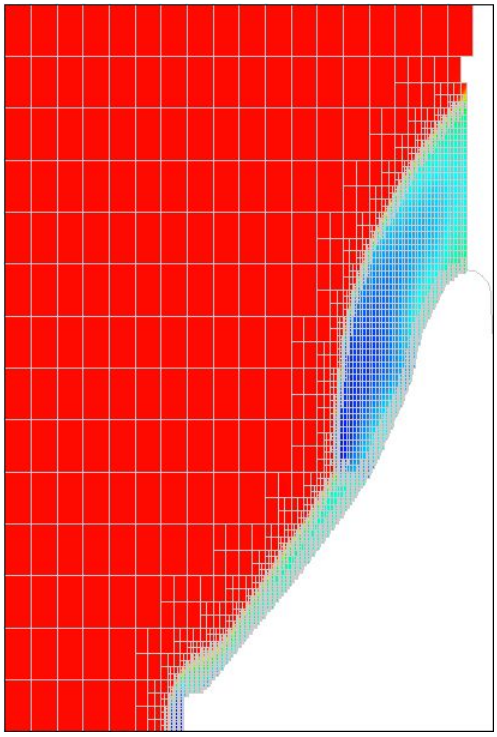

(b) M3 – 198,341 surface cells.

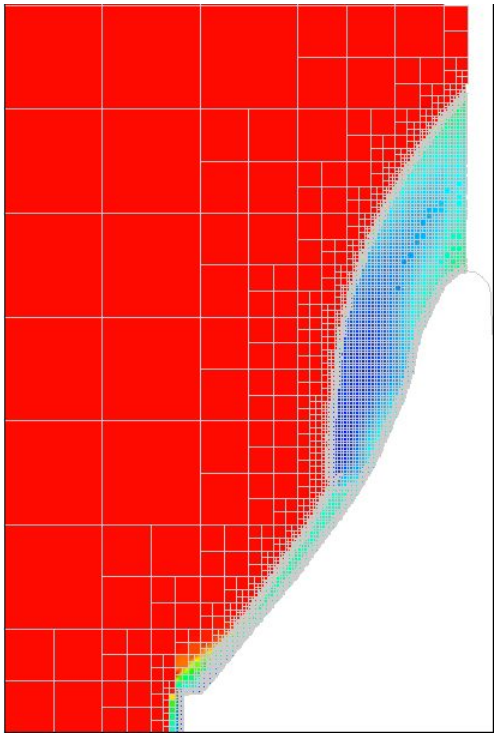

(c) F1 – 378,645 surface cells.

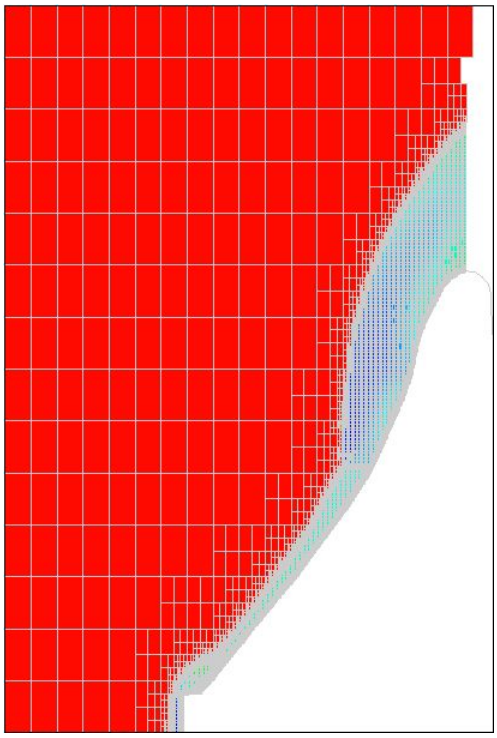

(d) F2 – 638,415 surface cells.

Figure 3-10: Grids used in the NASCART-GT convergence study of the ISP wind tunnel test model. Red indicates higher Mach number.

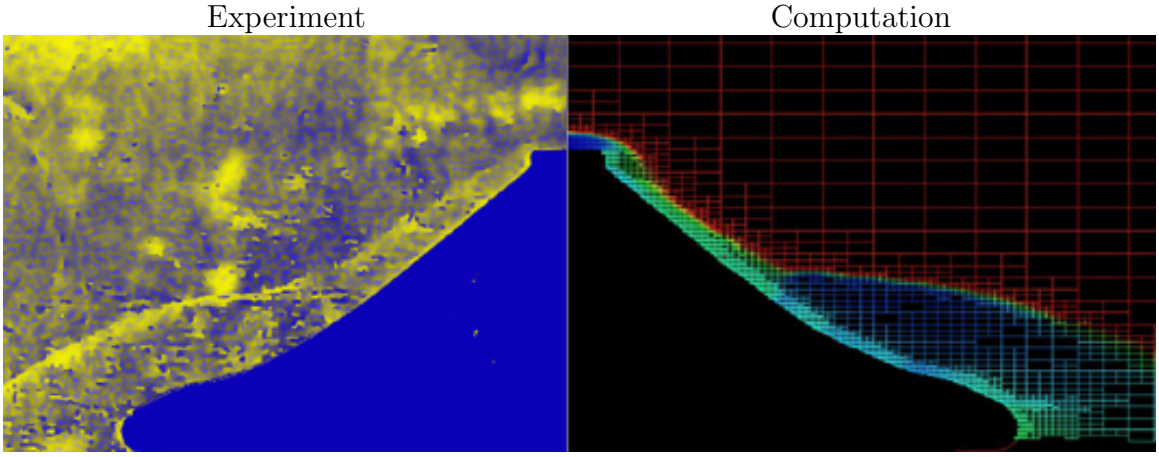

Figure 3-11: The computational solution shows good agreement with the experimentally observed shock structure.

a solid body. This approach generates an average deformed surface since it does not contain the surface wrinkle patterns. The number of cells used to define the body in NASCART-GT was then varied and the axial force coefficient (C_A) was used to judge convergence. Four of the grids used in the study are shown in Figure 3-10 with Mach number contours of the flow field. The shock structure is nearly identical in all of the grids studied, and Figure 3-11 compares the shock structure computed with NASCART-GT using the M3 grid and a photograph from the wind tunnel test. The shock structure in the photograph was enhanced by applying a different color map to the image and adjusting the contrast. Good agreement is observed between the computed and experimental shock structures.

Figure 3-12 shows the axial force coefficient for each grid used in the grid study. The grid with approximately 200,000 cells on the surface (M3 grid) appears converged, but during coupled analysis it was discovered that NASCART-GT had difficulty with the surface boundary conditions over the fine wrinkles at this grid density. Better results were obtained using the F1 grid, (approximately 380,000 cells on the surface) so this grid will be used for the subsequent coupled analysis.

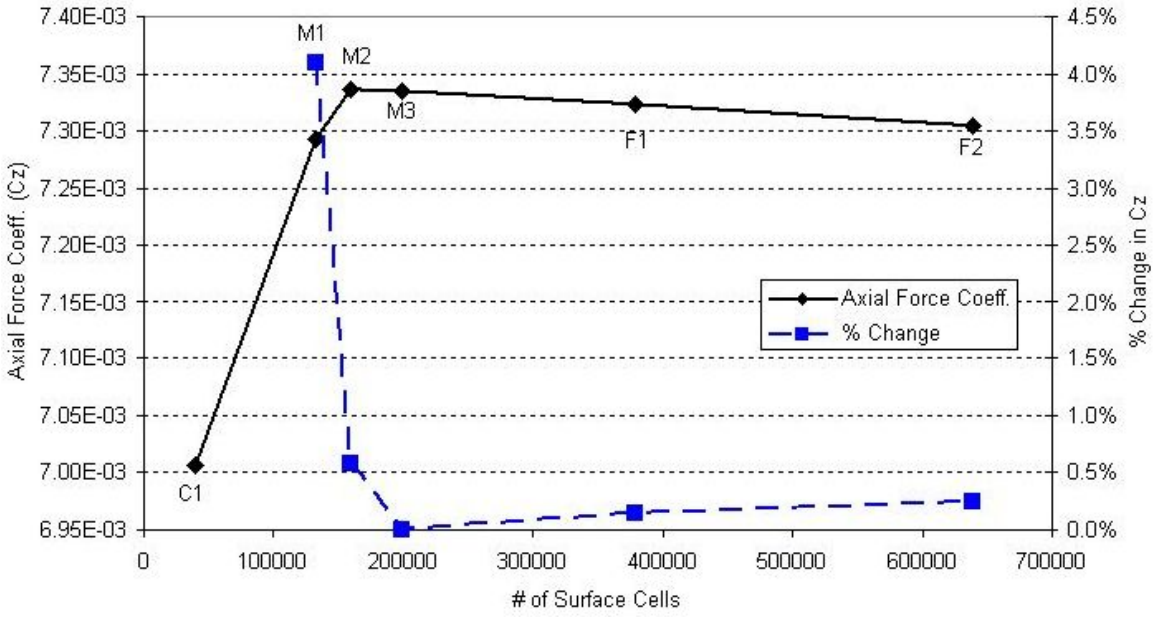

Figure 3-12: NASCART-GT grid convergence study showing good convergence for all models with 200,000 surface cells or more. Here the axial force coefficient is calculated using a reference area of 1.0.

3.4.2 High-Fidelity Coupled Results

The coupled analysis was initiated using modified Newtonian analysis for the first iteration and NASCART-GT for subsequent iterations. In the high-fidelity analysis, the structural model was run for 2.5 seconds between each iteration with artificial damping applied to allow vibrations to damp out between CFD analyses. These two enhancements were made in an effort to save computation time since only a static deformed shape is desired and the CFD analysis takes approximately 4 times longer than the structural analysis.

For each coupling iteration, NASCART-GT required approximately 5,000 iterations to converge. Figure 3-13 shows the axial force coefficient and the numerical residual both reaching constant values, demonstrating that 5,000 iterations is sufficient to converge the pressure loads.

The coupled solution was run for 6 iterations at which point the last 3 iterations

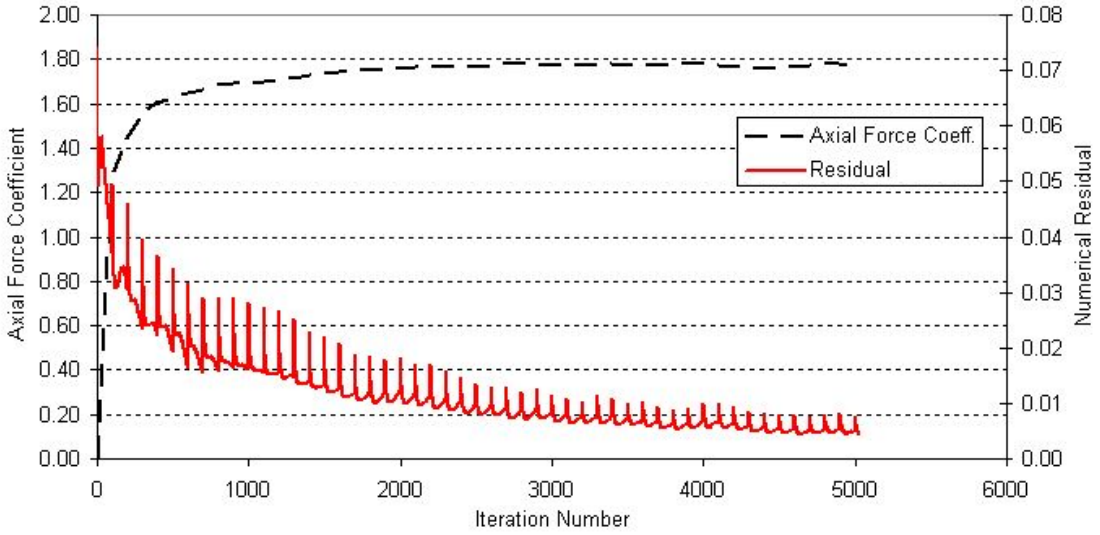

Figure 3-13: NASCART-GT convergence of numerical residual and axial load coefficient for coupled iteration 6.

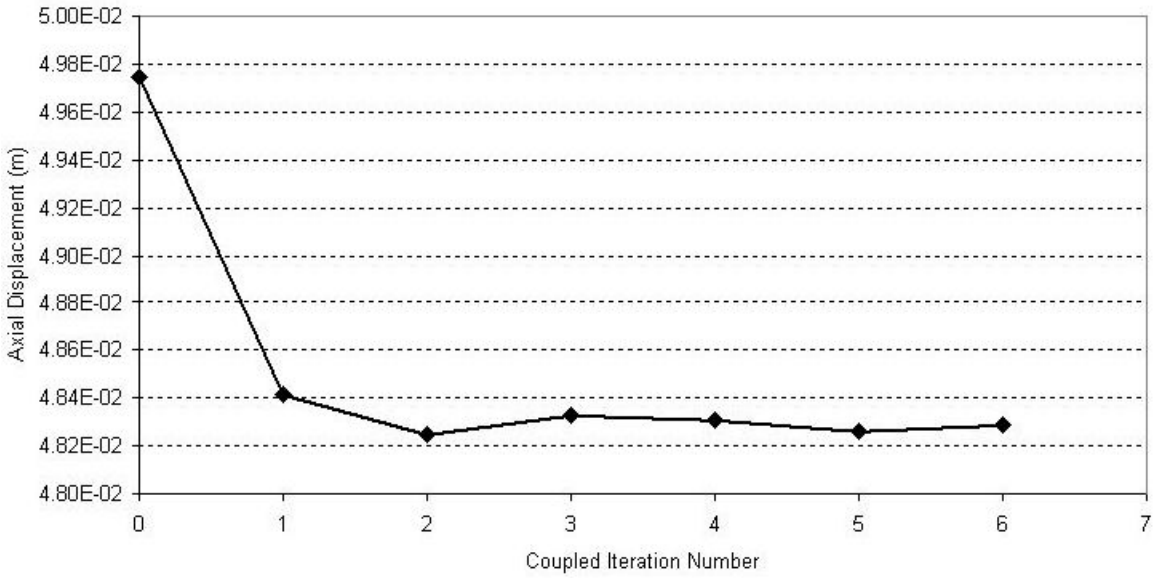

Figure 3-14: Convergence of axial displacement of the ISP wind tunnel validation case.

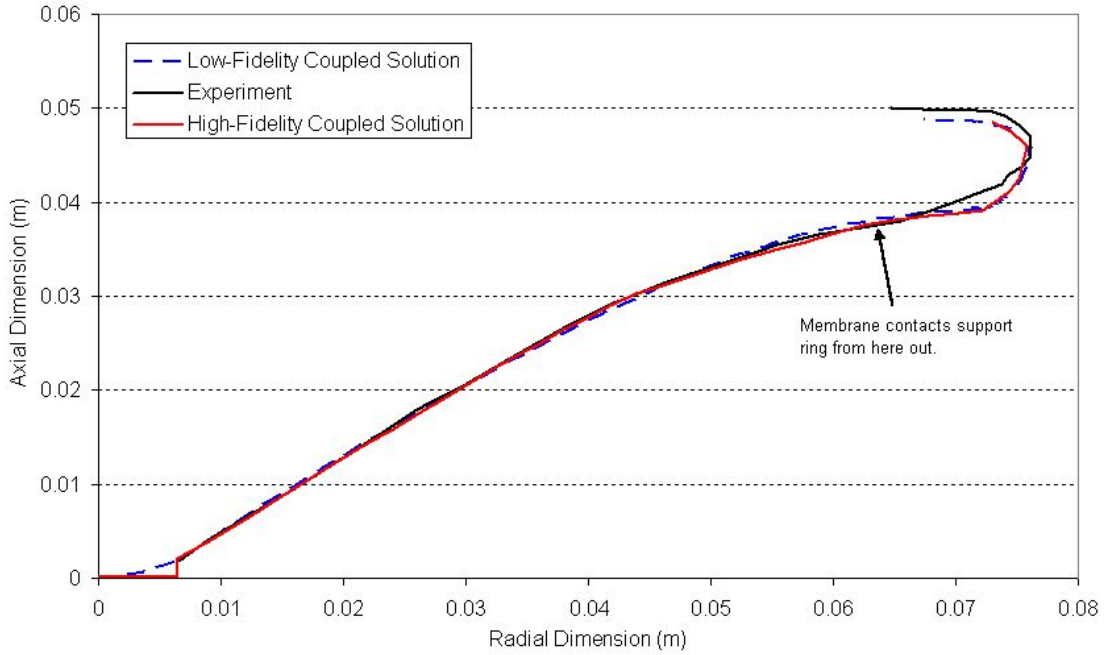

Figure 3-15: Deformed profiles from NASCART-GT and modified Newtonian aerodynamics compare well with experiment.

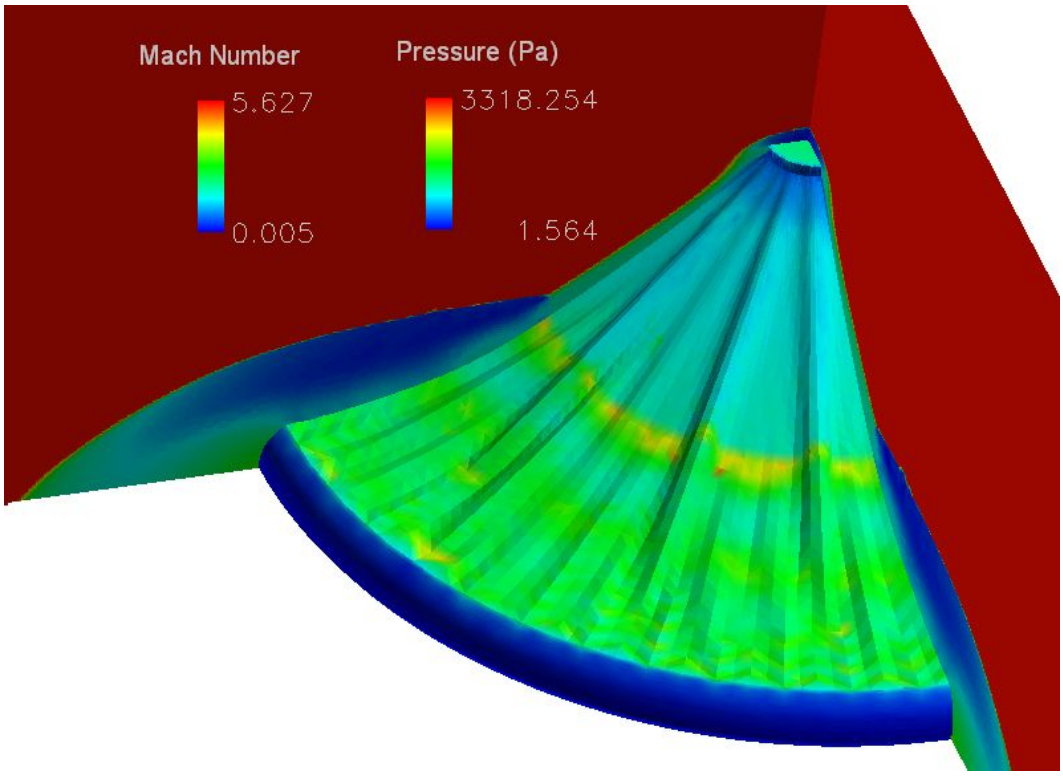

Figure 3-16: Surface pressures and flow field Mach number distribution computed by NASCART-GT on the deformed geometry.

had changed the axial deformation less than 0.1% as shown in Figure 3-14. The resulting profile of the deformed shape is shown in Figure 3-15. This deformation is very close to that obtained using the low-fidelity aerodynamic analysis (3.3). The high-fidelity solution surface pressure distribution and flow field Mach number are shown in Figure 3-16. The discontinuous high pressure ring on the surface is due to shock-shock interaction and is disturbed where surface wrinkles pass through the interaction region. The flowfield shows very similar structure to that obtained in the experiment (Figure 3-11), though the deformed shape near the outer radius of the model is slightly different and causes the shock to be less curved.

3.5 Summary and Comparison of Low- and High-Fidelity Results

When NASCART-GT pressure data is used in the coupled analysis, the results are essentially the same as for the modified Newtonian analysis (Figures 3-5 and 3-16). The primary differences are that NASCART-GT predicts constant pressure over the wrinkles, and a high pressure region due to shock-shock interaction at about 2/3 the vehicle radius. Figure 3-18 illustrates the differences in surface pressure between CFD and modified Newtonian aerodynamics. Despite the difference in pressure distribution, the deformed profiles are nearly identical, indicating that the deformed shape of this geometry is relatively insensitive to pressure distribution.

Furthermore, the stress distribution in the membrane is nearly identical for both low- and high-fidelity models. Figure 3-17 shows the stress distribution in both models and indicates that the peak stress in the high-fidelity model is 27% higher, even though the peak stress is at the nose attachment point in both models. This is in-line with the 25.6% higher drag predicted by the high-fidelity aerodynamics, since the material area and wrinkle pattern is the same in both cases. The nearly identical deformed shapes, desipite the differences in drag and stress is attributed to the Kapton membrane being thick and stiff relative to the model size.

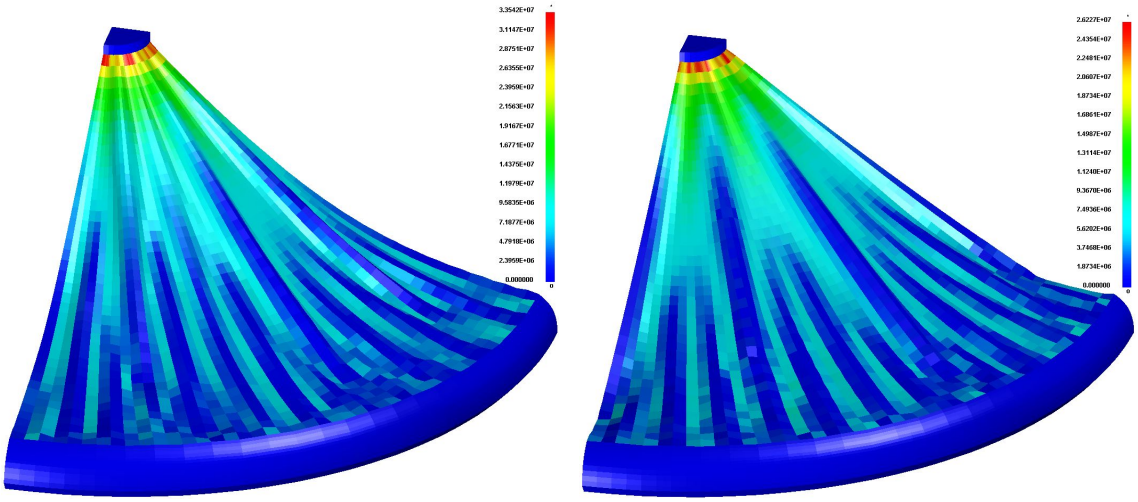

(a) High-fidelity stress distribution. (b) Low-fidelity stress distribution.

Figure 3-17: Stress distribution in the ISP wind tunnel model for both low- and high-fidelity solitions (Principal-1 stress in Pa).

Profiles from both low- and high-fidelity models match experiment very well considering the orientation of the profile in the test data is unknown relative to the surface wrinkling, no quantifiable data was obtained during the test itself, and the membrane contact with the aft support ring is unmodeled. Three-dimensional surface contours from test data could remedy this problem, but are currently unavailable.

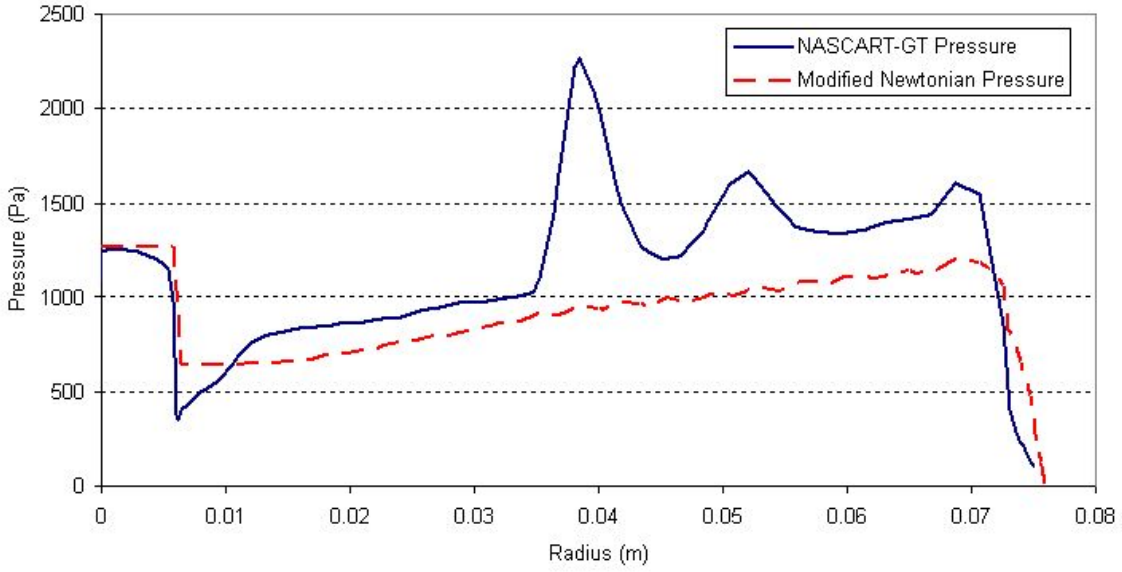

Figure 3-18: Surface pressure variation with radius for both NASCART-GT and modified Newtonian aerodynamics. The pressure spike at 0.4 m radius us due to shock-shock interaction.

CHAPTER IV

BALLUTE STATIC AEROELASTIC ANALYSIS

Aerocapture is possible at any body with a substantial atmosphere, and is of particular interest for missions to the outer planets. Titan, in particular, has been studied extensively as a target for an aerocapture mission. The mission selected as the example problem has been documented extensively in Miller et al. [87, 86], Johnson and Lyons [55], Westhelle and Masciarelli [126], Brown and Richardson [19], and James et al. [52].

4.1 Ballute Trajectory

The trajectory used in this study was computed for a 1,000 kg spacecraft inserting into a 1,000 km circular orbit about Titan with an atmospheric entry velocity of 6.5 km/s (atmospheric interface at 1,000 km). The aerodynamic drag used in the trajectory analysis assumes a rigid clamped ballute with a 12.1 m major radius, a 1.73 m minor radius, and a 60° cone half angle.

The trajectory is bounded on the steep side by a heat rate limit of 3 W/cm^2 and on the shallow limit by the minimum velocity change required to insert into a 1,000 km altitude circular orbit. Aeroelastic solutions will be calculated at two points on the steep aerocapture trajectory because the steep trajectory produces the highest aerodynamic loads. The peak dynamic pressure point will be analyzed since it is the highest loading on the trajectory, and a point in the transitional regime will be analyzed. The two conditions chosen are listed in Table 4-1. All aerodynamic analysis presented assumes a perfect gas with a constant ratio of specific heats.

Table 4-1: Trajectory data for two points on a Titan aerocapture trajectory.

	Peak Dyn. Press. Point	**Transitional Point**
Velocity (m/s)	4,266.4	6,512.0
Atm. Density (kg/m^3)	5.66x10^{-6}	2.05x10^{-8}
Atm. Temperature (K)	166	202
Atm. Pressure (Pa)	1.22x10^{-3}	2.73x10^{-1}
γ	1.424	1.416
Gas Constant (J/kg-K)	286.9	288.6
Knudsen Number	0.002	1.0
N_2 mole fraction	89.71%	92.04%
CH_4 mole fraction	1.09%	1.98%
Ar mole fraction	9.20%	5.98%

4.2 Ballute Geometry

Many options for the shape of a clamped ballute have been presented in the literature [87, 64, 62, 49, 81]. This section considers only thin-film clamped ballutes, and develops a structural grid model for use in coupled analysis.

4.2.1 Selection of a Clamped Ballute Configuration

Several clamped ballute configurations were considered, all with the same torus dimensions. Figure 4-1 shows the axi-symmetric profile of each ballute considered. Preliminary analysis was performed using Configuration 1, which was developed by Miller et al. [87, 86], but this configuration was found to buckle, even with fill pressures above 2000 Pa. The behavior was found during the grid convergence process, where the model would appear to be nearing convergence, and then suddenly diverge as the element count was increased. Figure 4-2 shows an example of this behavior for Configuration 1. Configuration 2 exhibited similar behavior.

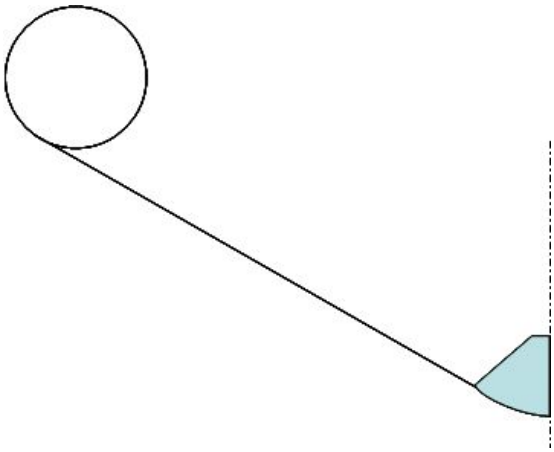

(a) Config 1 – 60° cone, forward-attach.

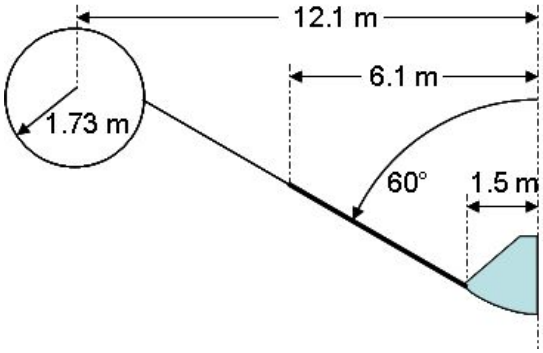

(b) Config 2 – 60° cone, mid-attach.

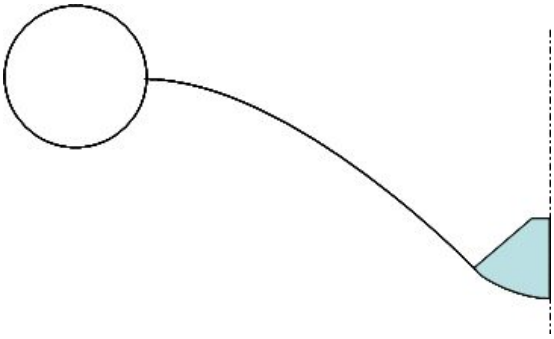

(c) Config 3 – Tension shell, mid-attach.

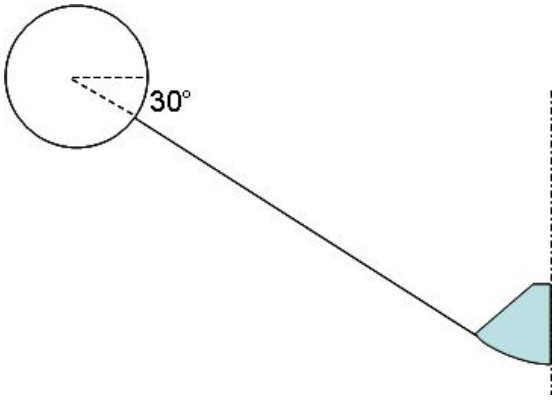

(d) Config 4 – 60° cone, 30°-attach.

Figure 4-1: Clamped ballute configurations considered for Titan aerocapture.

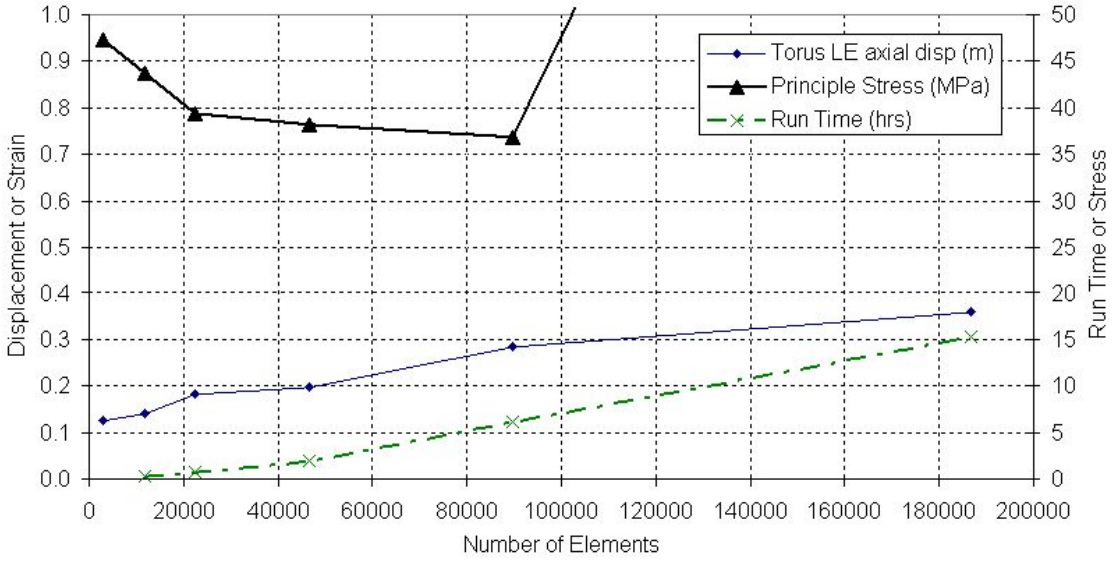

Figure 4-2: Grid metrics of Configuration 1 diverging as the model buckles.

When buckling of the torus was encountered, the effects of fill pressure and thickness on the stability of the ballute were explored. Fill pressures of 720, 800, 1000, 1200, 2000, and 2500 Pa were explored, and the torus material thickness was varied from 1.76x10^{-6} up to 3.4x10^{-4} m. After each change in fill pressure or material thickness, the grid study was restarted. Configurations 1 and 2 exhibited buckling with all fill pressures and torus material thicknesses explored.

Kyser [64] showed, mathematically, that if the conic membrane is attached to the torus in a way that twists the torus, the torus will buckle at a significantly lower load. To attempt to balance the vertical drag force on the torus with the tension from the conic membrane, the attachment point was shifted below the center of the torus (similar to Configuration 4). Angles of 45° and 30° were attempted. The model with cone attachment 45° below horizontal still caused twisting, but the model with attachment at 30° below horizontal produced no twisting of the torus at the peak dynamic pressure point conditions. Section 4.2.4 details the structural grid convergence of Configuration 4.

Many other configuration options are available, and possibly would provide a better attachment, but this study is not aimed at optimizing ballute configuration. Configuration 4 is structurally viable, and will be used for this study.

4.2.2 Structural Details of Configuration 4

Preliminary structural analysis revealed too high a stress level near the ballute to spacecraft attach point to use a polymer membrane for the entire cone so a 3.556x10^{-4} m thick Nextel fabric is used for the inner 6.1 meters of the cone. The remainder of the ballute is constructed of Upilex of 5.08x10^{-5} m thickness in the cone, and 3.4x10^{-4} m thickness in the torus.

The torus buckling equations of Weeks [124] were used as an initial guess for the fill pressure and torus material thickness, but were found to predict far too low a

fill pressure compared to the values required by finite element analysis. The increase in required fill pressure is believed to be due to a difference in loading between the analytic model assumptions and reality. The analytic model assumes a pure radial load from the centerline of the torus when, in reality, there is a radial load and a vertical load twisting the torus about its centerline. Furthermore, the radial load is not applied to the torus centerline, nor is it evenly distributed due to wrinkling. In addition, the analytic model is for small deformations and the actual model is pulled inward causing wrinkling (geometrically non-linear behavior) on the inner diameter of the torus.

4.2.3 Ballute Material Properties

The properties of Upilex are affected by temperature, and this is accounted for in the structural model. Unfortunately, ballute temperature is only known at the peak dynamic pressure point, and is applied to the ballute as a uniform temperature of 228°C. For the transitional point the temperature is unknown and so is estimated at 100°C for the purpose of this study. The temperature data is applied to the material properties, producing a lower modulus material. Thermal expansion was not included in these models since it produced a numerical instability for which a solution has not been found. More work is necessary in the area of thermal modeling to determine the actual ballute temperature, to model variable temperature material properties, and to include thermal expansion effects.

The properties of Upilex SN are listed in Table 4-2 at the two temperatures used. The modulus and Poisson ratio of Nextel 312 AF-10 fabric are essentially constant at 7 GPa and 0.20 over the temperature range from 0°C to 400°C, while the yield stress drops from 118 MPa to 88 MPa over the same temperature range [120].

Table 4-2: Material properties of Upilex.

	100°C	**228°C**
E (GPa)	4.692	3.883
ν	0.34	0.34
Yield Stress (MPa)	210.0	130.0

4.2.4 Ballute Structural Grid Convergence

Configuration 4 was modeled in LS-DYNA as a quarter model using quadrilateral shell elements. A grid convergence study was performed with this model using a fixed aerodynamic load based on the initial geometry and using between 12,736 and 450,560 elements. Aerodynamic loading is calculated using the modified Newtonian method for speed, and a sample of the grids used in the study are shown in Figure 4-3. Convergence of the structural model was based on axial displacement and VonMises stress since displacement determines the aerodynamic loading and VonMises stress is a good measure of failure for isotropic materials. Figure 4-4 shows that the model with 348,705 elements was adequately refined, and will be used for the remainder of this study.

4.2.5 Axisymmetric Structural Models

Due to the axisymmetric geometry and loading used in this study, use of an axisymmetric structural model was explored. In this test case, the axisymmetric model was loaded with a constant pressure distribution that produces a total load higher than the aerodynamic load at the peak dynamic pressure point. The resulting deformation is shown in Figure 4-5 and is a fraction of that observed in the three-dimensional quarter model (total displacement of 0.23 m compared to 0.6 m for the 3-d model). The difference is attributed to a difference in load carrying ability in the hoop direction.

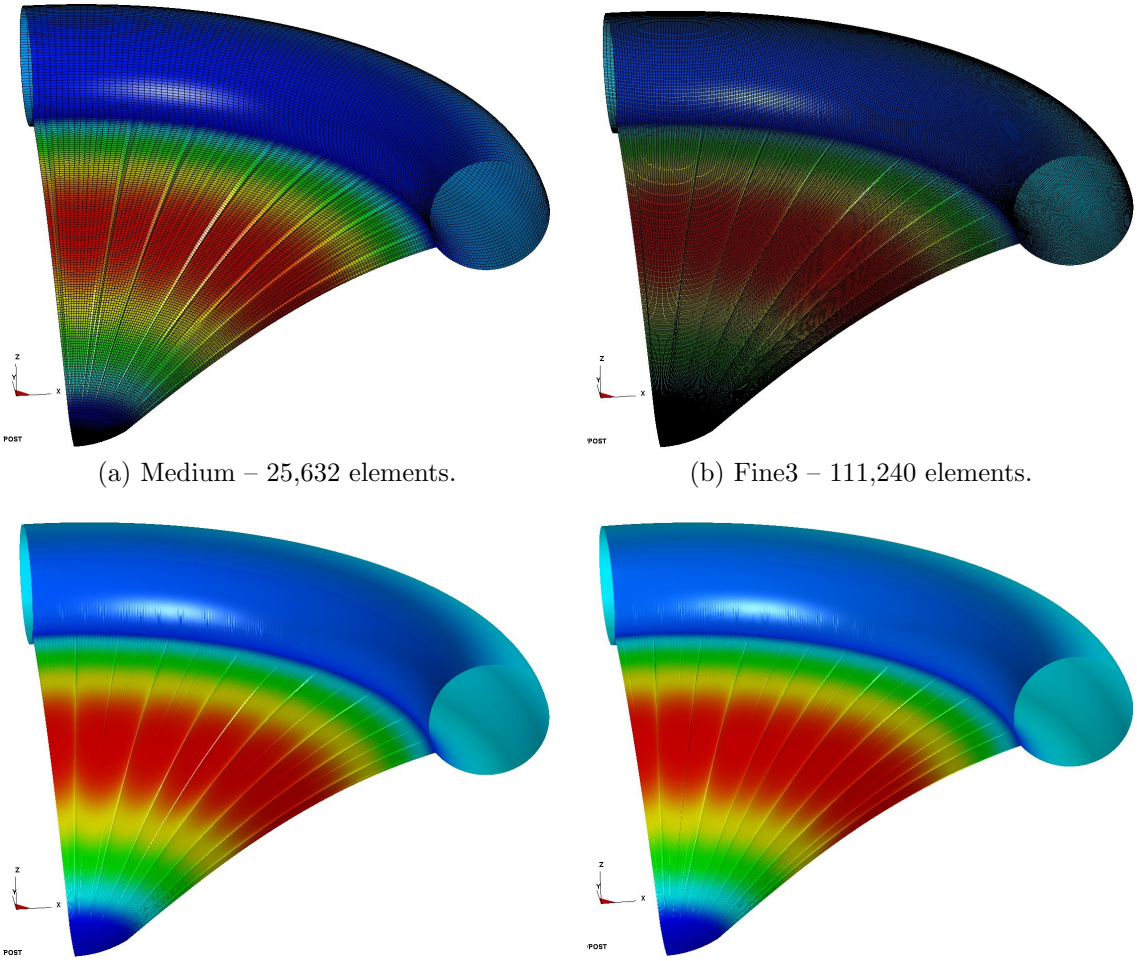

(a) Medium – 25,632 elements.

(b) Fine3 – 111,240 elements.

(c) Fine6 – 348,705 elements.

(d) Fine7 – 450,560 elements.

Figure 4-3: Grids used in the clamped ballute convergence study. Element edges are not shown for the fine grids since the model would appear black. Red indicates larger axial displacement.

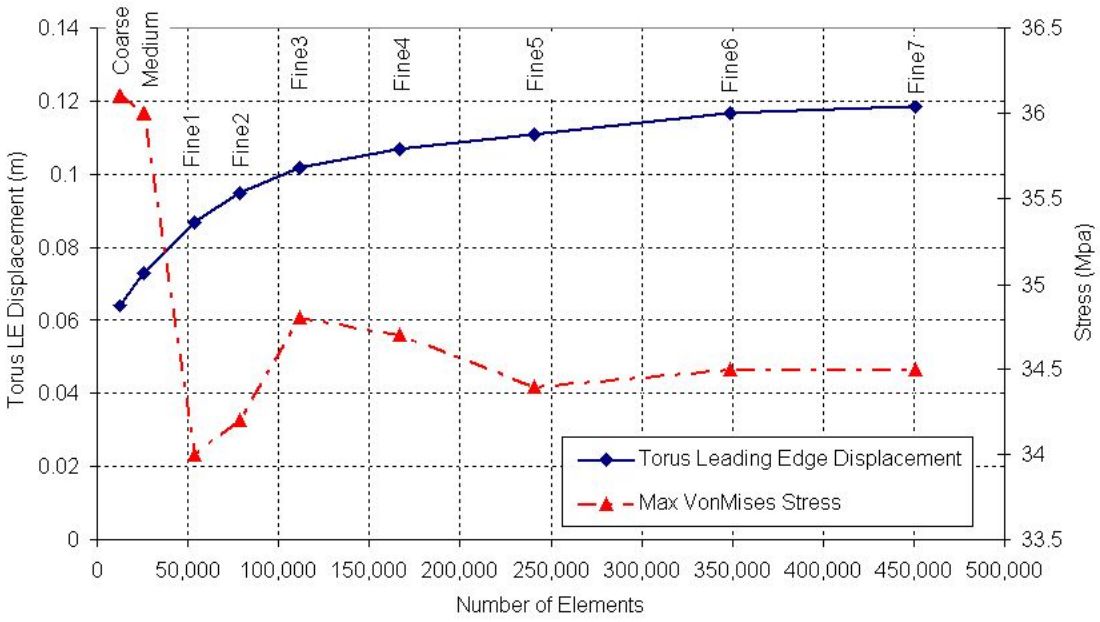

Figure 4-4: Grid metrics used to determine convergence of the clamped ballute structure model.

In the three-dimensional model the conic membrane buckles (producing wrinkles) and carries no compressive load in the hoop direction. The axisymmetric model uses isotropic material properties and carries load in the hoop direction because it cannot buckle. It may be possible to obtain the appropreate displacement with an axisymmetric model if orthotropic material properties are used to eliminate the load carrying ability in the hoop direction. However, LS-DYNA is not capable of using orthotropic material properties in an axisymmetric shell model. Furthermore, the axisymmetric model cannot predict wrinkle flutter if it exists, and the wrinkling can cause premature buckling of the torus which is also not captured in an axisymmetric model. Further exploration and application of axisymmetric models is left for future work.

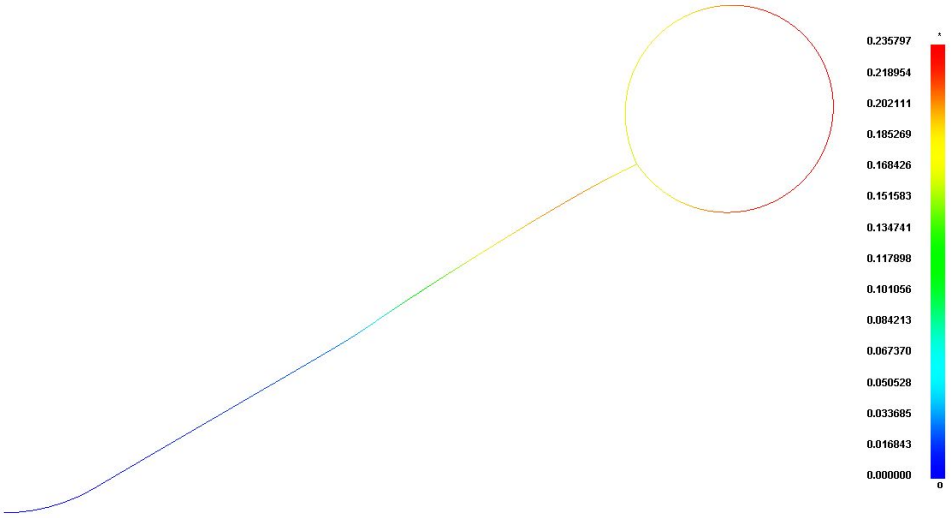

Figure 4-5: Deformation (in meters) of the axisymmetric model is a fraction of that observed in the three-dimensional quarter model.

4.3 Results Using Low-Fidelity Aerodynamics

The two trajectory points listed above were both run using the low-fidelity aerodynamics tools to estimate the deformation. A low-fidelity structural grid (the Fine3 model with 111,240 elements) will also be used with this analysis to reduce computation time since the intent of the low-fidelity tool is to provide a rapid design tool. This introduces a 15% difference in displacement compared to the high-fidelity model. Both points fall in the transitional regime as defined in Section 2.4.3 and will use the bridging function to compute surface pressures.

4.3.1 Peak Dynamic Pressure Point Analysis

The peak dynamic pressure case is nearly in the continuum regime and primarily derives surface pressure from the modified Newtonian analysis. The resulting axial displacement of the torus is 0.13 meters in the flow direction and the maximum VonMises stress is 37.1 MPa, well below the yield stress. The deformed shape with surface pressure contours is presented in Figure 4-6 and shows clearly defined surface wrinkles.

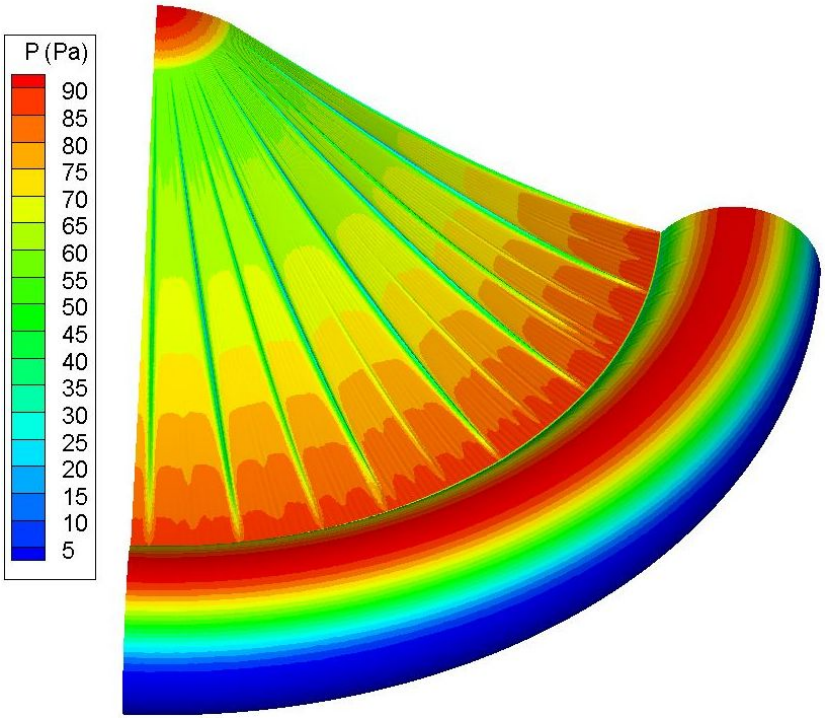

Figure 4-6: Deformed clamped ballute at peak dynamic pressure with surface pressure contours in Pa.

4.3.2 Transitional Results

The transitional regime case is nearly in the rarefied regime and is mostly influenced by the collisionless DSMC calculation. Due to the substantially lower atmospheric density the axial deflection of the torus is -0.7 meters (moving forward) and the maximum VonMises stress is 22.5 MPa. The deformed shape with surface pressure contours is shown in Figure 4-7. At this flight condition the pressure is not high enough to stretch the conic membrane taught, and the wrinkles that have formed are not fully stretched, as seen in the peak dynamic pressure analysis. The wrinkles that have formed in the membrane wander on the surface and have secondary kinks in their structure, causing locally high stresses despite the realatively low drag load. The edge where the fabric and polymer membrane join is visible as the smaller diameter ring of lower pressure at the middle of the cone since the deflection there changes due to the changing material properties.

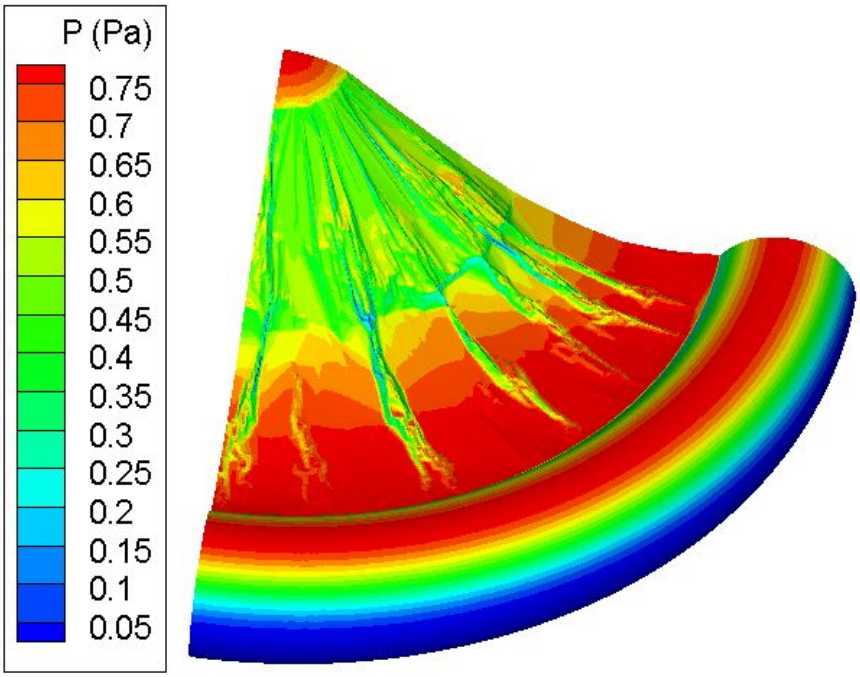

Figure 4-7: Deformed clamped ballute in transitional regime with surface pressure contours.

4.4 Results Using High-Fidelity Aerodynamics

The same two trajectory points used in the above low-fidelity analysis were run using the high-fidelity aerodynamics tools to determine a more accurate deformation. A high-fidelity structural grid (the Fine6 model with 348,705 elements) will be used with this analysis.

4.4.1 Continuum Analysis at the Peak Dynamic Pressure Point

The peak dynamic pressure point has a Knudsen number of 0.002, which is just outside the continuum range according to the analysis of Section 2.4.3, but in the area of overlap between CFD and DSMC analyses in Figure 2-4. Due to the relativiely high density at this point, DSMC analysis is computationally too expensive, so NASCART-GT will be used.

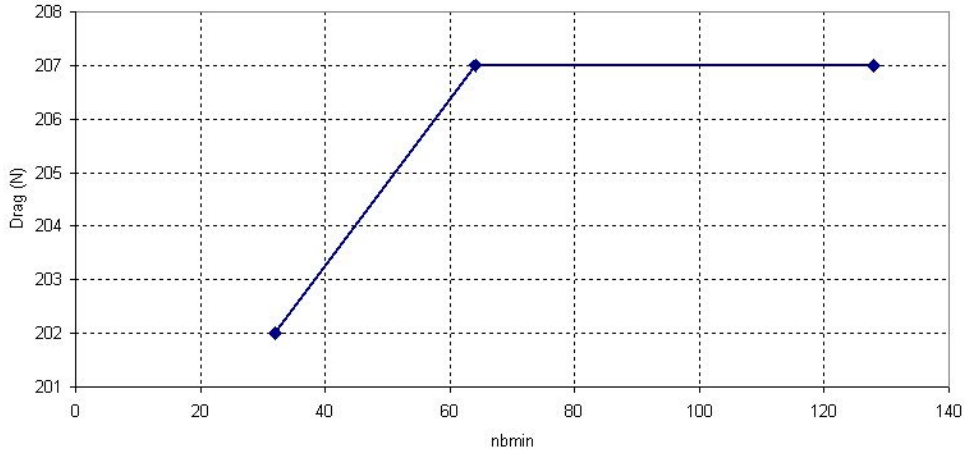

Figure 4-8: Computed drag force indicates that grids with *nbmin* greater than or equal to 64 are grid independent.

4.4.1.1 Grid Convergence in NASCART-GT

To verify that the grid resolution was not affecting the results from NASCART-GT, a convergence study was performed using the undeformed clamped ballute geometry. The parameter *nbmin* was varied from 32 up to 128 to increase the grid density. Drag is used as the convergence metric since it is a significant contributor to the deformation of the structure. Figure 4-8 shows the drag as the grid density is varied. The change in drag between the grids with *nbmin*=64 and *nbmin*=128 is less than 1%. The surface pressure distribution for the grids with *nbmin*=64 and 128 are shown in Figure 4-9, and it is apparent that the grid resolution causes a decreased pressure at the attachment of the cone and torus near the symmetry plane for the coarser model. For this reason, the grid with *nbmin*=128 (Figure 4-10) will be used for the coupled analysis presented in the following section.

4.4.1.2 Results of Continuum Analysis at the Peak Dynamic Pressure Point

A coupled case using a quarter model was run using NASCART-GT and the Fine6 structural model and the *nbmin*=128 aerodynamic grid. Due to the computational grid generation process in NASCART-GT, the structural grid is coarsened for input

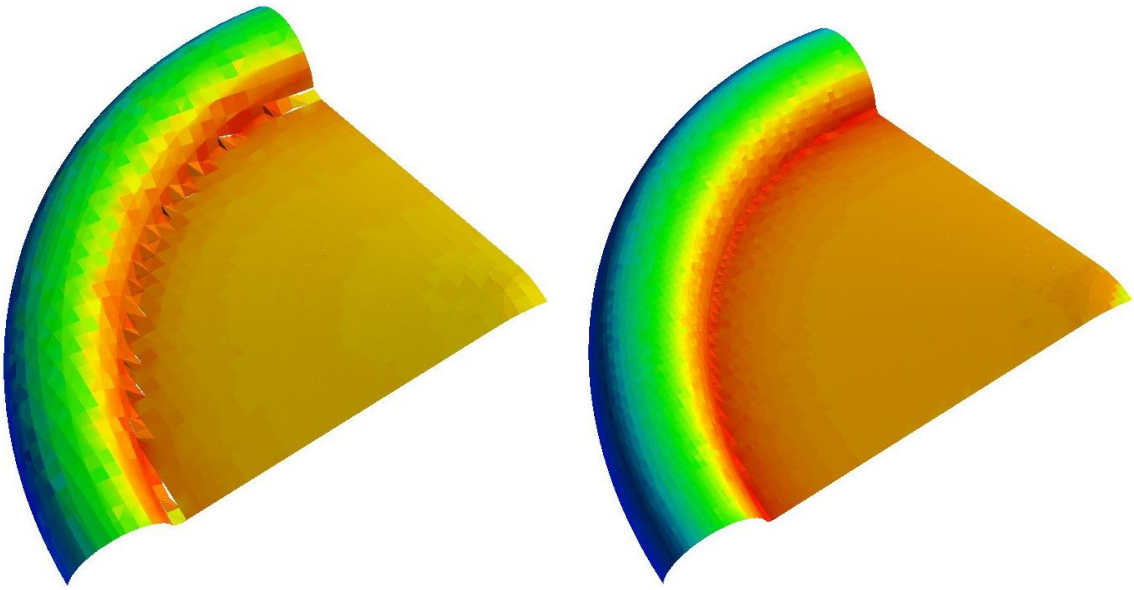

(a) $nbmin = 64$. (b) $nbmin = 128$.

Figure 4-9: Surface grids computed by NASCART-GT. The coarser grid does not properly capture the inside corner and underpredicts pressure near the symmetry plane. Red indicates higher surface pressure.

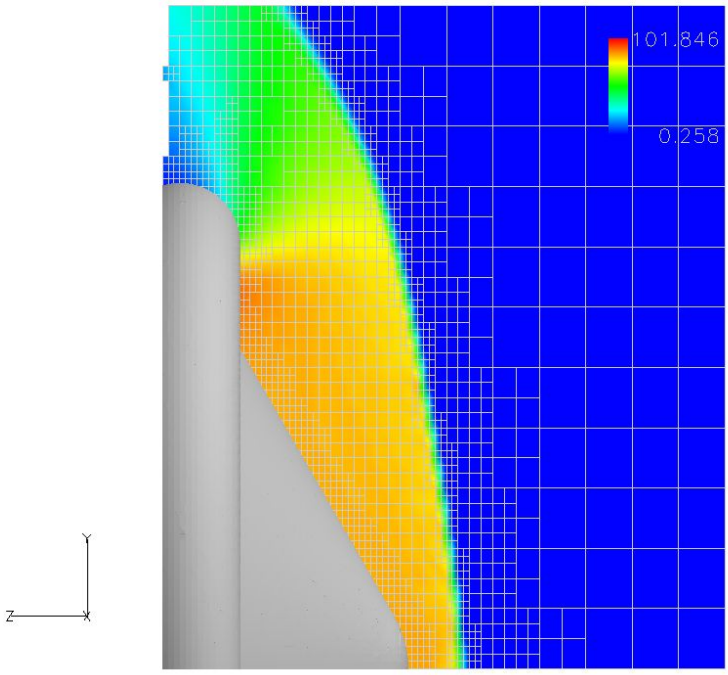

Figure 4-10: Pressure countours (in Pa) around the undeformed clamped ballute model with $nbmin$=128.

to NASCART-GT. The surface input grid to NASCART-GT shares every fifth node in the radial and circumferential directions with the structural model so that no interpolation is required for displacement transfer. The pressure mapping process is described in detail in Section 2.5. Grid coarsening causes the surface wrinkles to be smeared, but the NASCART-GT cartesian grid does not fully capture them, so no resolution is lost. Figure 4-11 shows the structural grid, the NASCART-GT input grid, and the NASCART-GT computational grid from the last coupling iteration.

The solution took 5 iterations to converge (Figure 4-12), and 5 days of computer time when running NASCART-GT on 21 processors (15 AMD Opteron 248 and 6 AMD Opteron 280) and LS-DYNA on 31 processors (15 AMD Opteron 248 and 16 AMD Opteron 280). The resulting deformed shape with surface pressure and free stream Mach number is shown in Figure 4-13. Close inspection of the pressure on the deformed body indicates some pressure variation along the two symmetry planes. A full three-dimensional model was run, and it was determined that the pressure variations are due to the symmetry conditions since they do not exist in the full model. The pressure variation is limited to within two aerodynamic computational cells of the boundary and is less than 5% different than pressures in the full model. Due to the small variation and proximity to the boundary, these variations will be neglected, and no data along either symmetry plane will be used.

The deformation results in a peak VonMises stress of 38.9 MPa and a peak principal stress of 41.1 MPa, both which occur in the membrane where it attaches to the fabric inner cone. Figure 4-13 shows the VonMises stresses of the deformed configuration, with the rigid spacecraft in dark blue.

4.4.2 Transitional Regime Analysis

The transitional case was run using the DAC software as a point of comparison for the low-fidelity aerodynamics tool.

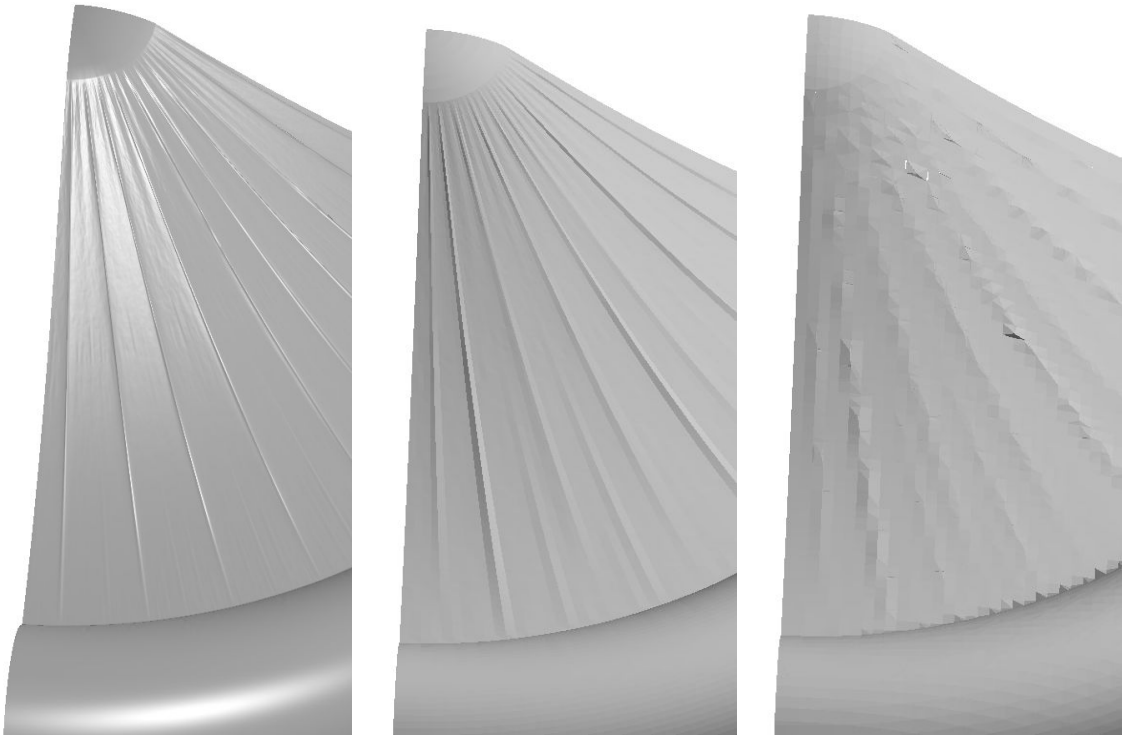

(a) Structural grid. (b) CFD input grid. (c) CFD computational grid.

Figure 4-11: Comparison of the three surface grids used in high-fidelity coupled analysis with NASCART-GT show that no detail is lost by coarsening the input grid.

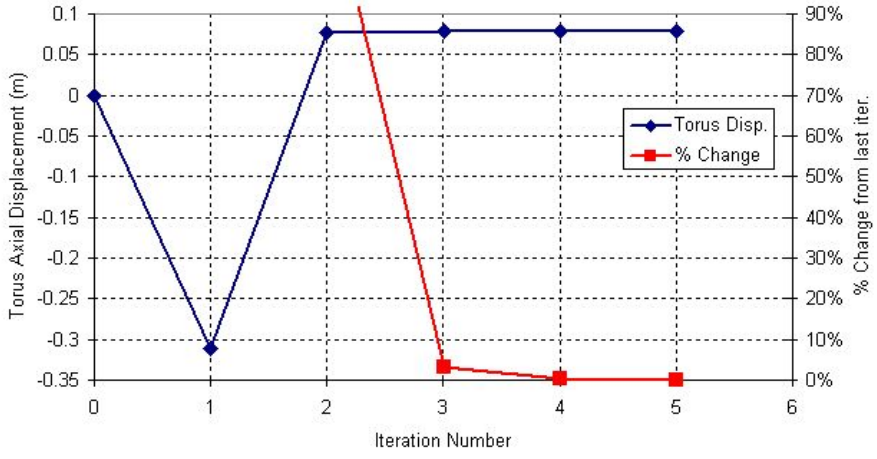

Figure 4-12: Convergence of the high-fidelity coupled solution using NASCART-GT.

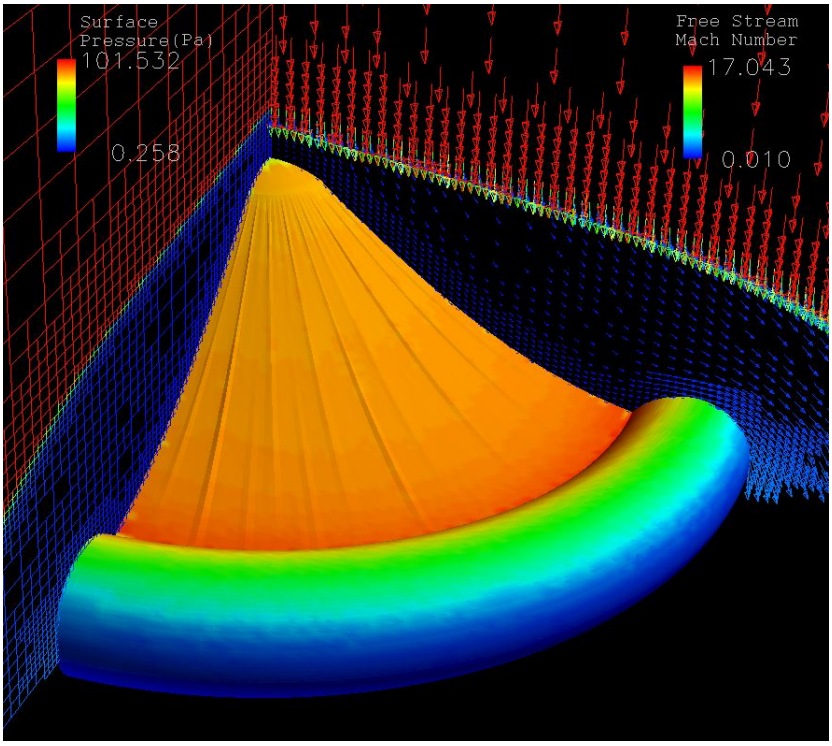

Figure 4-13: Surface pressure countours and free stream Mach number around the deformed ballute, showing the input surface grid.

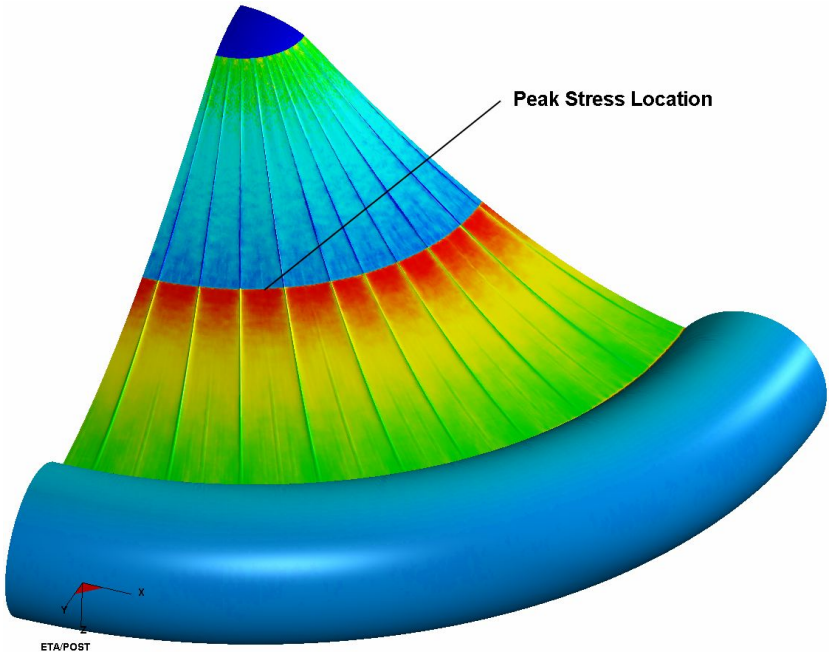

Figure 4-14: Peak VonMises stress occurs at the seam between fabric and membrane on the deformed clamped ballute. Red indicates higher stress.

4.4.2.1 DSMC Grid Study

DAC utilizes a cartesian grid which affects the execution time and accuracy of results. A trade-off can be made between the number of iterations to run and the number of real-to-simulated (RTS) molecules. The primary constraint on the grid is to have cells smaller than one local mean-free-path (λ) so that collisions occur between molecules within reasonable spatial proximity. DAC can adapt the grid to meet the local λ requirement on cell size, but the process requires manual input and would require substantial work to automate. The primary goal of the grid study is to find the fastest combination of grid size and RTS molecule ratio that produces good force output and does not require adaptation. Furthermore, the dimensions of the simulated domain have an affect on the solution, and this will be studied using the best grid size and RTS molecule count.

For this flight condition the free stream λ is approximately 25 meters. This study looks at grids with cell dimensions ranging from 1 meter down to 0.12 meters in 4 steps, and with RTS molecules ranging from $1x10^{18}$ to $1x10^{14}$. Figure 4-15 shows a slice through the flow field for each grid used in the study and the flow field temperature using $1x10^{14}$ RTS molecules. The back of the body was closed off to produce a solid geometry for automatic mesh generation and because the flow in the wake does not affect the pressure on the forebody. The grid size is overlaid on the flow field temperature results since DAC produces a different grid for results output than is used for the computation. All simulations assume a non-catalytic wall with diffuse particle interaction and only translational and vibrational modes of the gas are considered.

Each grid test was run until the forces converged, and the execution time required to reach a converged solution is shown in Table 4-3 along with the resulting axial force. For each grid and RTS molecule count, the solution was considered converged when the change in the forces or moments was less than 0.1% for at least three consecutive output intervals. The coarse grid did not converge in five times the number

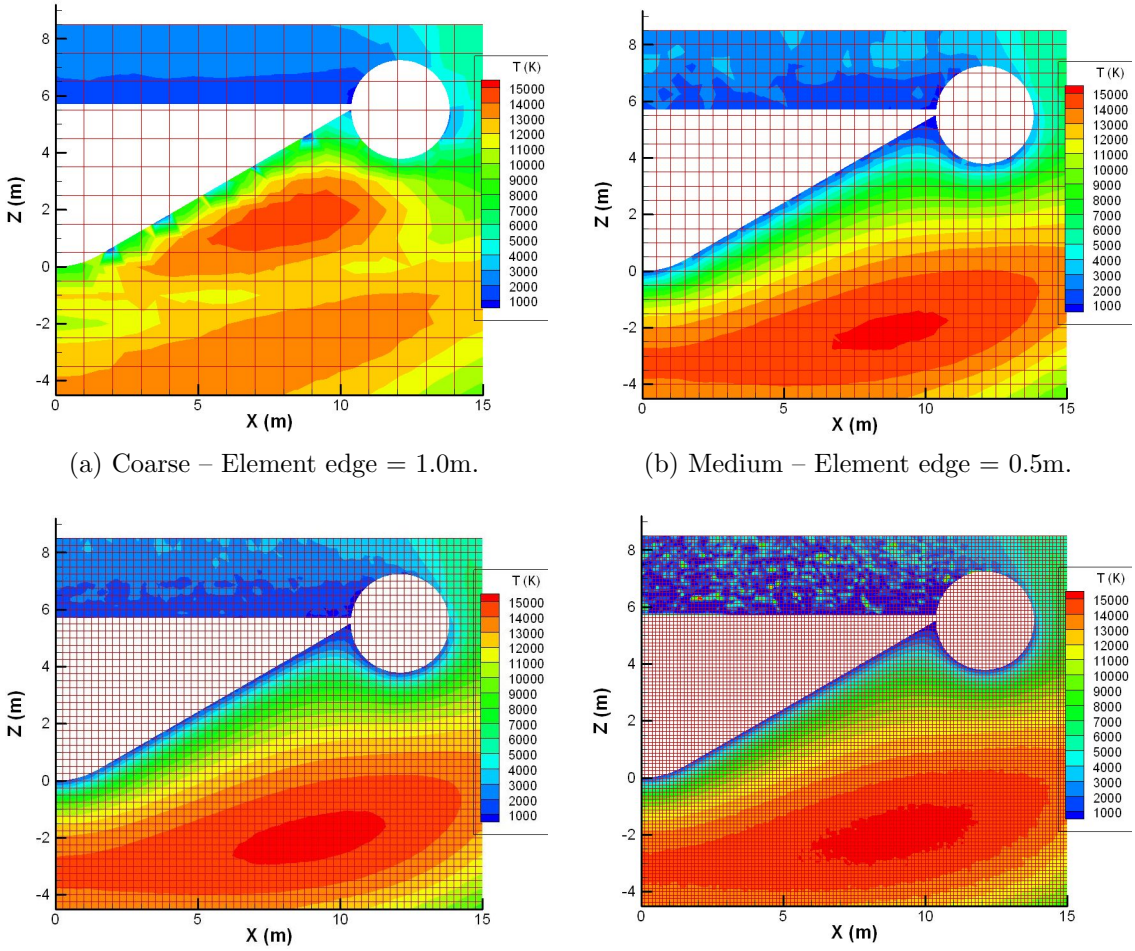

(a) Coarse – Element edge = 1.0m.

(b) Medium – Element edge = 0.5m.

(c) Fine – Element edge = 0.25m.

(d) XFine – Element edge = 0.125m.

Figure 4-15: The grids used in the DAC grid convergence study.

Table 4-3: Time to converge each run (min) and axial force (N) in the DAC grid convergence study. Green indicate the fastest run times with good drag values, and red indicates runs with poorly predicted drag.

RTS **Molecules**	**Medium**	**Fine**	**XFine**
$1x10^{14}$	41 / 126.9	36 / 126.8	39 / 126.6
$1x10^{15}$	4.5 / 126.9	3.1 / 126.5	21 / 126.1
$1x10^{16}$	1.3 / 126.5	1.1 / 125.6	3.3 / 125.2
$1x10^{17}$	0.4 / 124.9	0.5 / 125.8	2.3 / 133.4
$1x10^{18}$	0.4 / 128.9	0.5 / 134.7	1.8 / 134.6

Table 4-4: Computational domain dimensions and axial force using the Fine grid with $1x10^{15}$ RTS molecules.

Domain Number	**1**	**2**	**3**	**4**	**5**	**6**	**7**	**8**
Domain width (m)	15	15	15	20	20	20	20	25
Axial length (m)	11	13	15	19	25	28	32	32
Axial force (N)	132.0	126.5	123.1	120.7	118.9	118.5	118.2	118.4
Chng in axial force	-	4.2%	2.7%	2.0%	1.5%	0.3%	0.3%	0.2%

of iterations required to obtain a converged solution in the other three grids, so adaptation was performed in an attempt to obtain a solution. The adapted grid produced the same forces and moments as the other three grids, but required substantially more time and grid adaptation, ruling it out for use in coupled solutions. As the RTS molecule count increased (fewer simulated molecules) the resulting axial force started to vary. The Medium, Fine, and XFine grids all produced the same axial force without grid adaptation (using $1x10^{14}$ RTS molecules), but the time required was minimum for the Medium grid. Since the time required for the Medium and Fine grids with $1x10^{16}$ and $1x10^{15}$ RTS molecules respectively is very small compared to the time to run the structural model, the Fine grid was chosen because it can resolve the surface wrinkles more accurately. The Fine grid with $1x10^{15}$ RTS molecules will be used to study the domain size and for coupled solutions.

Since the front of the shock is not quite included in the domain used for the grid

study, the domain size was explored. Domain dimensions and axial force are listed in Table 4-4 along with the relative change in axial force. The Fine grid pictured in Figure 4-15c is domain size 2 in this study, with one smaller domain and 6 larger domains explored. Domain size 8 increases the width over domain size 7 and shows that increasing the width of the domain does not affect the solution. Domain size 6 appears to have reached a converged axial force with a relative change in force of less than 1.0%, and will be used for the coupled solution. Figure 4-16 shows the flow field temperature of domain size 6 and the thicker shock compared to Figure 4-15c.

4.4.2.2 Transitional Results

A static coupled solution was computed for a quarter model of the clamped ballute using the Fine6 structural grid and the Fine aerodynamic grid with domain size 6. A quarter model was chosen because off-axis deformations are not expected and surface wrinkles can still be captured. The model includes a backface to close the body (as seen in Figure 4-15a) for aerodynamic analysis which is not included in the structural analysis. Elements on the torus which are internal to this structure have no aerodynamic pressure applied to them since they are in the wake where the pressure is very low.

The structural analysis was run for 30 seconds between each coupling to allow the solution to damp out any oscillations between aerodynamic analyses. Since the above grid study was performed on an undeformed geometry, the aerodynamic analysis was run for 4000 iterations to leave a sufficient buffer such that the solution is statistically significant even if it takes longer than for the undeformed shape. Figure 4-17 shows the forces from the DAC model converging (at iteration 1000) well before the run completes on the final coupling iteration. The resulting deformation is shown in Figure 4-18 with surface pressure contours on the body and temperature contours on the flowfield slice. The convergence history of the axial displacement of a node on the

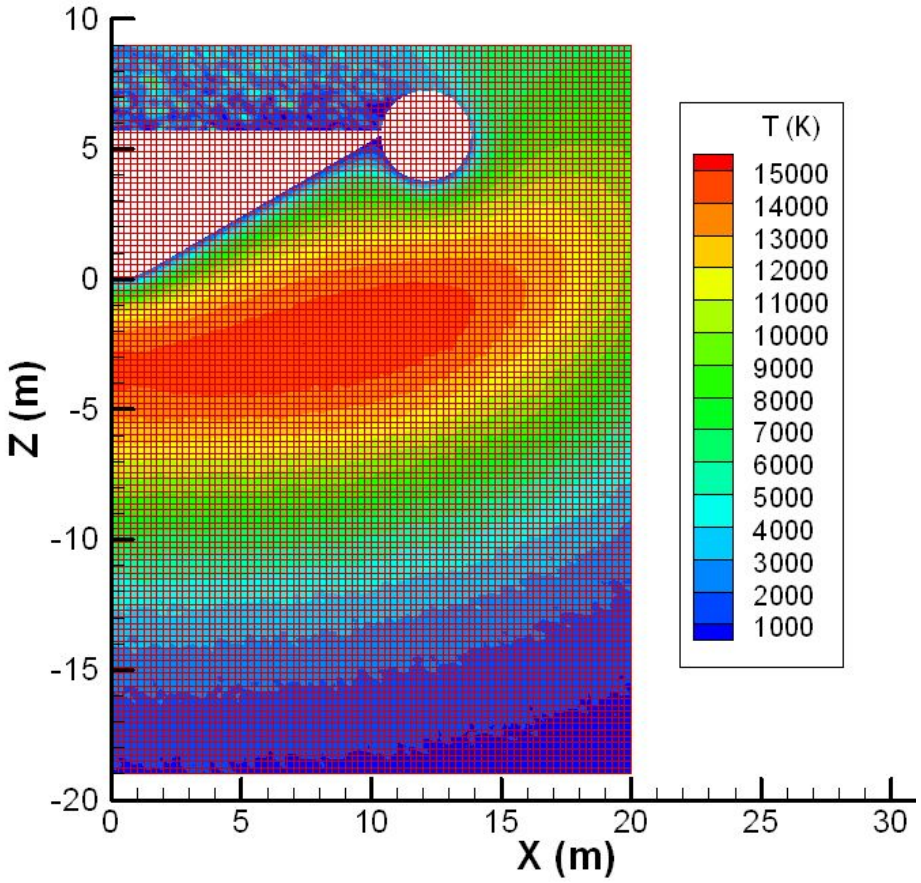

Figure 4-16: Flow field temperature in domain size 6.

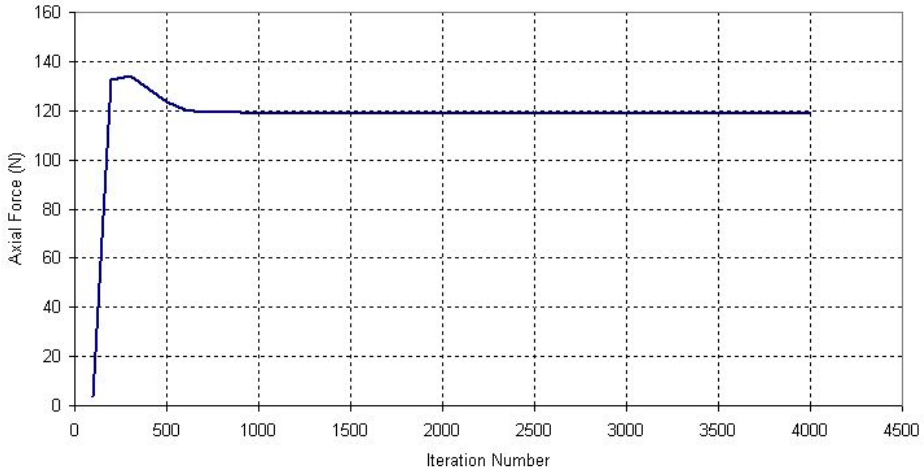

Figure 4-17: Converged forces on the final coupling iteration for DAC.

leading edge of the torus is shown in Figure 4-19. The drag on the deformed body is 118.7 N, well within 1% of the undeformed body, indicating that coupled analysis is not necessary in the upper end of the transitional regime to get accurate drag predictions for performance analysis. This should be expected since the deformation is much smaller than the shock stand-off distance and, as such, will not have much affect on the flow field.

4.5 Comparison of Low- and High-Fidelity Results

At the peak dynamic pressure point there is good agreement between the low- and high-fidelity solutions for stress and drag, as seen in Table 4-5. Peak stresses occur in the same location (at the joint between fabric and membrane) in both models. The axial deflection of the torus is significantly different despite the small difference in overall drag, which is due to the difference in pressure distribution.

There are two key differences in the pressure distribution betwen the low- and high-fidelity models. In the high-fidelity model there is a detached shock wave that encompasses the entire body, and a pocket of high pressure at the torus/membrane

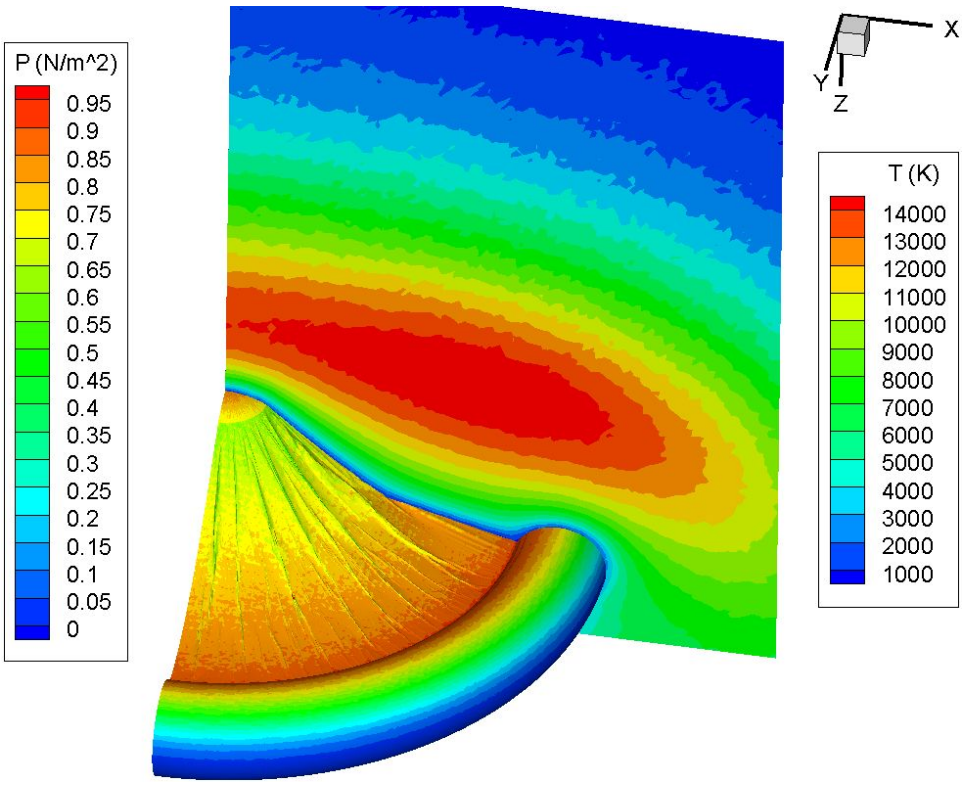

Figure 4-18: The deformed clamped ballute in the transitional regime with surface pressure contours in Pa and flowfield temperature in Kevlin.

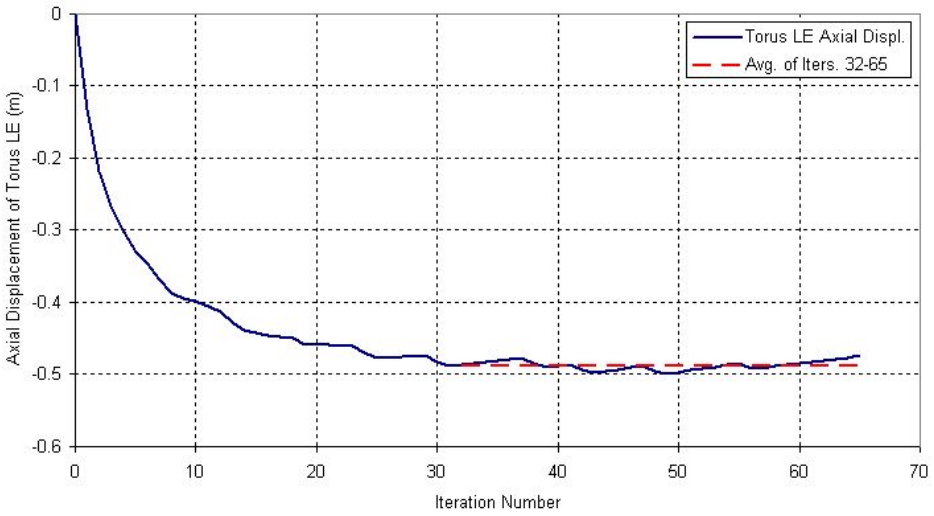

Figure 4-19: Axial displacement of the torus after each coupling iteration. Forward displacement is negative.

Table 4-5: Metrics for the clamped ballute at peak dynamic pressure.

Metric	**Mod. Newtonian**	**CFD**	**Difference**
Axial Deflection of Torus (m)	0.13	0.079	69%
Max. VonMises Stress (MPa)	37.1	38.9	4.8%
Max. Strain (%)	0.39	.549	40%
Nose Pressure (Pa)	94	89	5.6%
Drag (N)	10,662	11,493	8%
Approximate Computation Time*	23 hrs.	5 days	420%

*CFD uses 21 AMD Opteron 248 cores and FEA uses 31 cores

attachment. The low-fidelity model lacks this high pressure region, but instead predicts approximately 50% higher pressure on the front face of the torus. This difference in pressure distribution accounts for the 8% difference in total drag on the quarter model and the difference in the axial displacement of the torus.

At the transitional regime point on the trajectory, analysis was performed using both low-fidelity impact methods and DSMC aerodynamics. Several significant differences are observed including the torus axial deflection and the peak VonMises and principal stress in the membrane (Table 4-6).

The difference in torus axial deflection is caused by the pocket of high pressure at the junction of the conic membrane and torus in the DSMC calculations. This produces a moment that rolls the torus outwards compared to the low-fidelity analysis.

The difference in the peak VonMises stress is due to slight differences in the wrinkle formation, which is influenced by the local surface pressure around the wrinkles. Figure 4-20 shows a close-up of the peak stress location and the difference in wrinkle shape for both low- and high-fidelity models. In the low-fidelity analysis, the pressure on the wrinkles is substantially lower than the surrounding areas, which allows the wrinkles to be less well defined. In the DSMC results, the pressure is much closer to the surrounding area over the wrinkles, forcing them to become better defined and

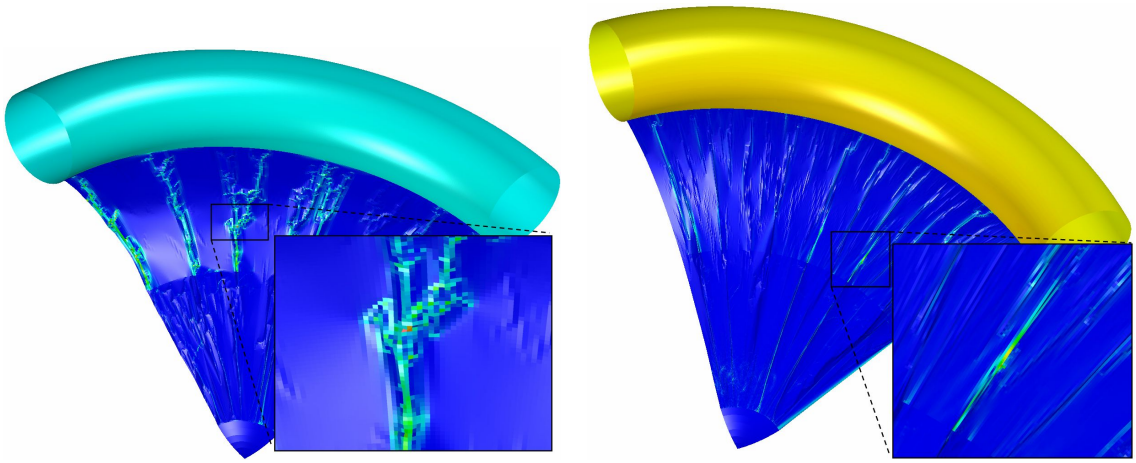

(a) Low-fidelity model. (b) High-fidelity model.

Figure 4-20: Peak stress location and wrinkle shape differs between the low- and high-fidelity models in the transitional point analysis.

much narrower. Due to the lower pressure, the wrinkles in the low-fidelity analysis have kinks in them which produce locally high stress levels. Furthermore, the peak stresses in the low-fidelity model occur at bends with small radii, and the element formulation used does not support bending, nor does it have sufficient resolution to properly capture such small radii. In Section 5.2 it will become apparent that this point in the trajectory provides insufficient drag to fully stretch the ballute.

The predicted drag is 13% lower in the DSMC analysis which is probably sufficient for conceptual design considering the low total drag. The difference is likely due to the low-fidelity aerodynamics computing low pressure at the joint between the torus and membrane, whereas the DSMC analysis predicts high pressure in that region. This causes the lower integrated drag on the low-fidelity model and a different loading, with the high-fidelity model being stretched more radially than the low-fidelity model, contributing to the better formed wrinkles in the high-fidelity model.

Table 4-6: Metrics for the clamped ballute in the transitional regime.

	Collisionless DSMC	**DSMC**	**Difference**
Axial Deflection of Torus (m)	-0.7	-0.47	49%
Max. VonMises Stress (MPa)	22.5	6.5	246%
Max. principal Stress (MPa)	13.6	7.5	81%
Max. Strain (%)	0.39	0.06	5.5%
Nose Pressure (Pa)	0.80	0.83	3.8%
Drag (N)	105.0	118.7	13%
Approx. Computation Time*	15 hrs.	22 days	3570%

*Time using 32 AMD Opteron 248 cores

4.6 Summary

The deformed shape of a ballute was calculated at two points on a Titan aerocapture trajectory, one at peak dynamic pressure (using modified Newtonian analysis and NASCART-GT) and the other in the transitional regime (using collisionless DSMC and DAC). The resulting deformation and stress indicate that the ballute could survive the flight environment. Heating and accurate surface temperature prediction at these points requires further analysis.

Using continuum methods at the peak dynamic pressure point there was good agreement between the low- and high-fidelity models for drag and stresses. Axial displacement of the torus, however, was different by 69%, though this had little affect on the other metrics. Considering the computational time difference, the low-fidelity analysis provides sufficient accuracy for conceptual design studies where drag and VonMises stress prediction of the deformed shape is sufficient.

Comparison of the impact method aerodynamics and DSMC in the transitional regime indicate that the impact method is sufficient for trajectory analysis (drag

prediction 13% lower for low-fidelity methods on this configuration) but not for determining static stresses. The low total load at this point on the trajectory and the low stresses indicate that this point is not a design driver, and so only drag information from this point would be of interest during conceptual design.

From a conceptual design perspective, the parameters of interest (peak stress on the trajectory and drag at each point) are represented with sufficient accuracy by the low-fidelity methods for this configuration. When computation time is considered, the low-fidelity solutions provide a good compromise of time and accuracy.

CHAPTER V

AEROELASTIC ANALYSIS OF A TITAN BALLUTE

The goal of ballute aerocapture is to insert a spacecraft accurately into orbit about a planetary body with an atmosphere through drag modulation. Knowing when to discard the ballute requires accurate knowledge of the atmosphere properties and the drag provided by the ballute, which varies due to the flexible nature of inflatables. Ballute mass, as with all interplanetary missions, is of primary importance. Driving the system mass down requires accurate knowledge of the stress and structural stability of the ballute so that material thickness and mass can be reduced without compromising the mission. These goals, accurate drag knowledge and minimum mass, require coupled aerodynamic and structural dynamic analysis and should be included as part of the system design process.

5.1 Flight Conditions

Trajectories for aerocapture at Titan have been computed by Miller et al. [87] for a clamped ballute with identical frontal area to the one used here. Points have been selected on the steep entry trajectory of [87] that capture the dynamic pressure rise as the ballute passes through the atmosphere. The steep trajectory was chosen because the dynamic pressure, and hence aerodynamic loading, is higher than on shallow trajectories and will represent a worst-case loading condition. The conditions along this trajectory selected for analysis are listed in Table 5-1.

The material temperature for the analysis is taken from thermal analysis of the clamped ballute in Reference [87] and is an average temperature of the Upilex material at the peak heating point on the trajectory. In Reference [87] it is shown that the material temperature scales with the heat rate because radiation and the aerodynamic

Table 5-1: Titan aerocapture trajectory data points used for design analysis.

Flight Time	**Alt.**	**Relative Velocity**	**Density**	**Temp.**	**Dyn. Press.**	**Mole Fraction**			**Number Density**	**Material Temp.**	**Upilex Modulus**
						N_2	CH_4	Ar			
s	**km**	**m/s**	**kg/m^3**	**K**	**Pa**	**%**	**%**	**%**	**1/m^3**	**deg. C**	**MPa**
0	1,415.2	6,467.7	5.658×10^{-11}	203.7	0.001	78.48	20.54	0.98	7.962×10^{13}	-200	4.70×10^{9}
50	1,213.7	6,486.3	3.913×10^{-10}	203.8	0.008	88.66	9.39	1.94	5.859×10^{14}	-67	4.70×10^{9}
100	1,028.4	6,503.8	2.936×10^{-9}	204.0	0.062	92.46	3.87	3.66	5.051×10^{15}	49	4.70×10^{9}
148	868.5	6,512.0	2.053×10^{-8}	202.1	0.44	92.04	1.98	5.98	4.290×10^{16}	139	4.56×10^{9}
175	787.5	6,500.1	6.336×10^{-8}	193.8	1.34	91.26	1.53	7.21	1.484×10^{17}	178	4.35×10^{9}
197	726.6	6,461.9	1.622×10^{-7}	184.4	3.39	90.69	1.34	7.97	3.985×10^{17}	204	4.14×10^{9}
215	680.8	6,385.6	3.504×10^{-7}	176.5	7.14	90.33	1.24	8.43	8.832×10^{17}	219	4.00×10^{9}
230	645.7	6,261.4	6.562×10^{-7}	170.7	12.86	90.09	1.19	8.72	1.725×10^{18}	229	3.94×10^{9}
241	621.9	6,114.0	1.020×10^{-6}	167.4	19.06	89.96	1.16	8.88	2.767×10^{18}	234	3.90×10^{9}
252	600.0	5,900.0	1.540×10^{-6}	165.0	26.90	89.86	1.13	9.01	4.449×10^{18}	237	3.83×10^{9}
262	581.6	5,640.6	2.187×10^{-6}	163.9	34.79	89.79	1.12	9.09	6.618×10^{18}	238	3.82×10^{9}
272	565.0	5,313.5	2.997×10^{-6}	163.6	42.30	89.75	1.11	9.14	9.126×10^{18}	237	3.83×10^{9}
282	550.3	4,928.9	3.957×10^{-6}	164.3	48.06	89.73	1.10	9.17	1.243×10^{19}	235	3.88×10^{9}
298	530.8	4,266.4	5.663×10^{-6}	166.4	51.54	89.71	1.09	9.20	1.845×10^{19}	228	3.88×10^{9}
313	515.3	3,601.8	7.505×10^{-6}	168.9	48.68	89.71	1.09	9.20	2.507×10^{19}	217	4.05×10^{9}
327	504.0	3,056.6	9.176×10^{-6}	171.1	42.86	89.72	1.09	9.19	3.102×10^{19}	202	4.15×10^{9}
340	495.3	2,618.8	1.068×10^{-5}	172.9	36.61	89.73	1.09	9.18	3.666×10^{19}	186	4.28×10^{9}

heating dominate the thermal analysis. Furthermore, the material has very little mass, and conduction through the material is low. For this analysis, the temperature at the peak heat rate point is scaled over the trajectory so that it has a similar shape to the heat rate curve.

5.2 Static Deformed Shape Along a Trajectory

Static analysis at 17 points along a Titan aerocapture trajectory was performed using the low-fidelity clamped ballute studied in Section 4.3. Such analysis was not included in Reference [86] since a tool that provided sufficient accuracy within the computational efficiency required for conceptual design was not available. As shown previously, the low-fidelity drag and stress results are in good agreement with high-fidelity results, and will be used here to show trends on a Titan aerocapture trajectory. The time to analyze all 17 points was approximately 21 days; the amount of time required to analyze one to three points using high-fidelity analysis (depending on the flight regime).

Several parameters of interest to designers are shown in Figure 5-1 along the trajectory. As expected, the drag, stress, strain, and displacement are correlated to the dynamic pressure. However, the correlation is only for dynamic pressures above 1 Pa (time greater than 175 s). At lower dynamic pressures, the deformation is dependent on the initial deployed shape.

Figure 5-2 shows the deformed shape at a dynamic pressure of 0.008 Pa. The initial conical shape of the geometry is clearly visible in the fabric section of the model (radius less than 6.1 m, shown in magenta) and the Upilex section has drifted forward. The bending point is in the Upilex, and the shape does not make physical sense, indicating that the load is insufficient to overcome the material stiffness. Furthermore, the low-fidelity aerodynamics will under-predict the pressure in a cavity facing the flow and will not force the geometry into a curved shape as observed for higher

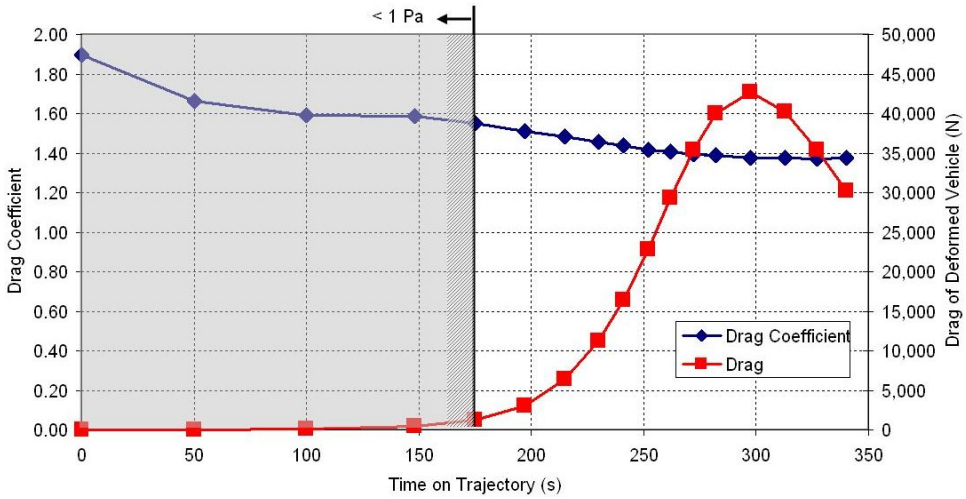

(a) Drag and C_D of the deformed shape.

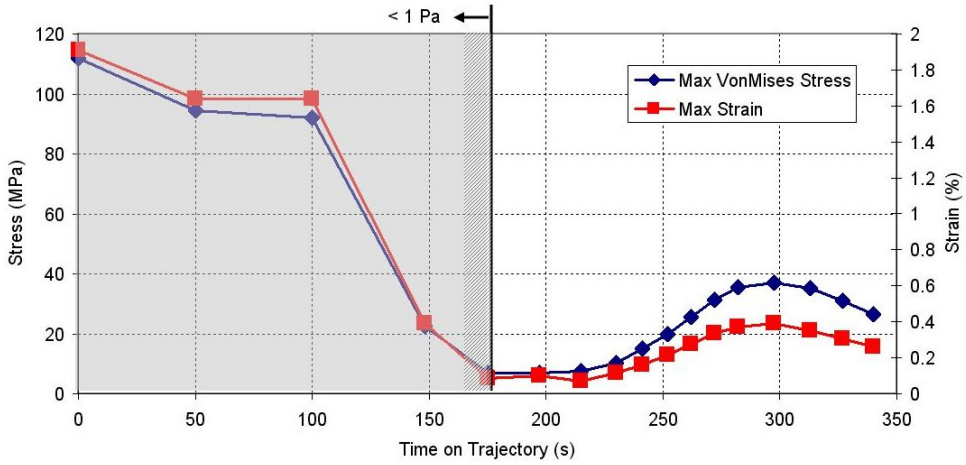

(b) Peak VonMises stress and strain.

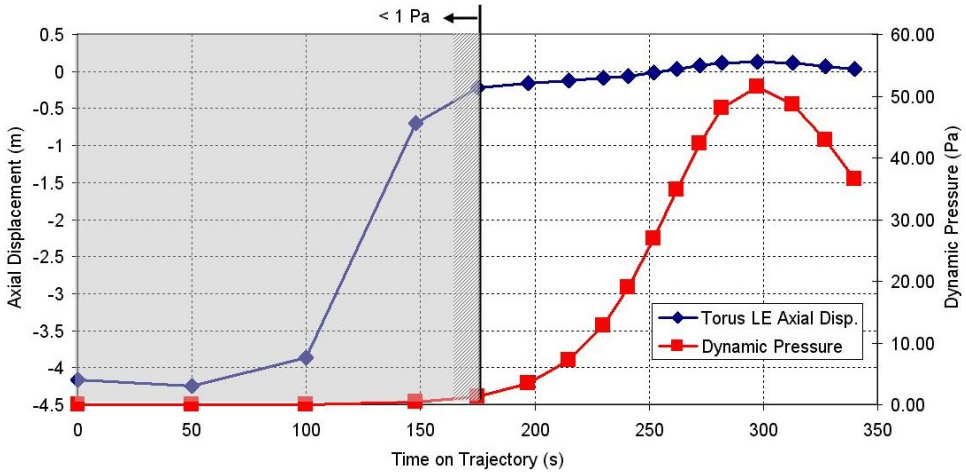

(c) Torus axial displacement and dynamic pressure.

Figure 5-1: Drag, displacement, stress, and strain correlate with dynamic pressure for dynamic pressure greater than 1 Pa.

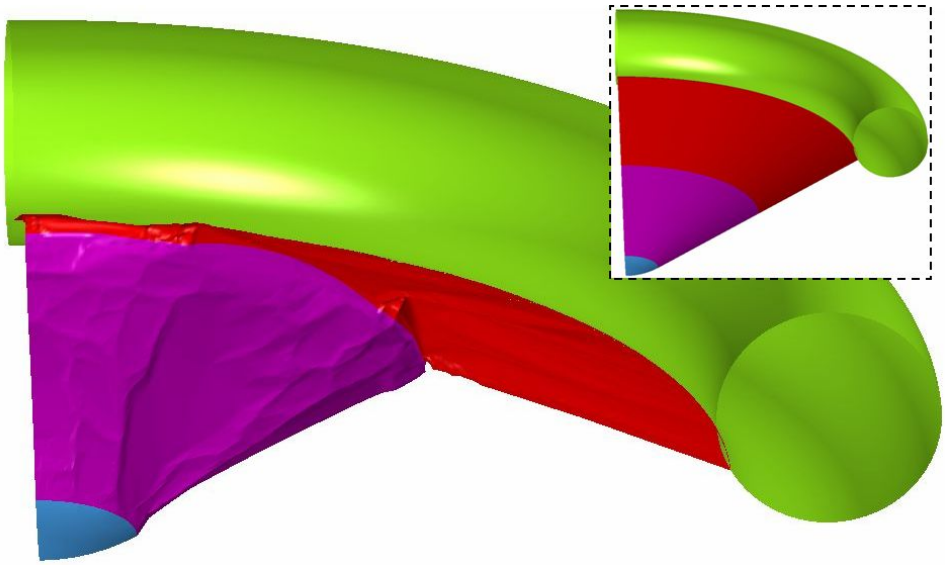

Figure 5-2: For low dynamic pressures (< 1 Pa) the deformed shape is dependent on the initial shape (shown in the inset) and does not accurately reflect the flight configuration.

dynamic pressure cases.

At low dynamic pressures, the peak VonMises stress and strain both occur in the folded wrinkles of the membrane, and the magnitude is likely not accurate because the element formulation does not support bending. Furthermore, due to the small bend radius, a much finer model would be required to accurately resolve the local stresses. Therefore, the results below a dynamic pressure of approximately 1 Pa do not accurately represent the flight configuration or stresses. The dependence on the initial deployed shape also brings into question the possibility of the ballute recontacting the spacecraft before the dynamic pressure is sufficiently high to deform the ballute in a predictable way. It is suggested that the torus be supported during inflation and prior to reaching 1 Pa of dynamic pressure.

At higher dynamic pressures the deformed shape and stresses appear reasonable. Figure 5-3 shows the deformed shape of the ballute at several points on the trajectory, highlighting the small variation in displacement for large dynamic pressures. Large displacements occur when dynamic pressure is low due to the torus drifting freely as

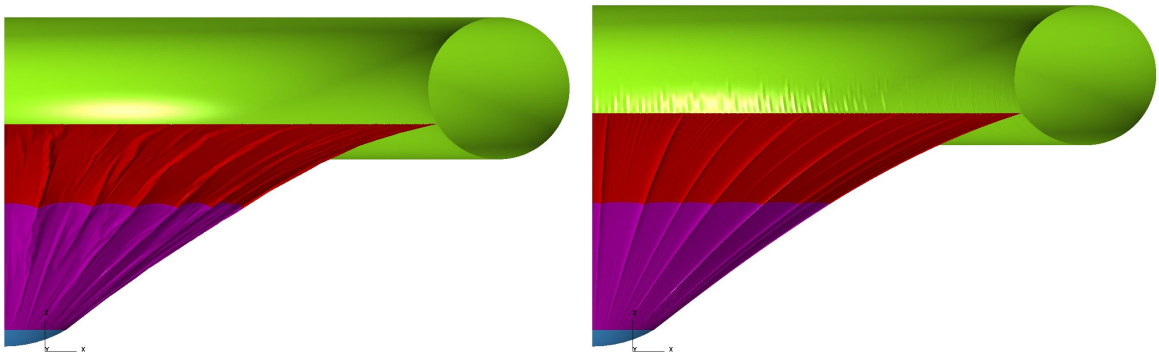

(a) Flight time = 175 s, q = 1.3 Pa.

(b) Flight time = 298 s, q = 51.5 Pa.

Figure 5-3: Variation in ballute displacement is small when dynamic pressure is greater than 1 Pa. The difference in torus axial displacement seen here is 0.36 m.

discussed previously.

Peak strain is approximately 0.4%, which is in the linear region of the Upilex stress-strain curve. Analysis at the peak dynamic pressure point indicates a peak stress of 37.1 MPa, which occurs in the Upilex at the Nextel/Upilex joint. According to thermal analysis at this point [87] the material temperature is approximately 200°C. At this temperature Upilex can withstand more than 130 MPa, indicating that mass savings might be possible while maintaining a significant factor of safety.

5.3 Low-Fidelity Flutter Analysis

To determine the survivability of a ballute during an aerocapture maneuver, it is important to know if the structure flutters in the design flight regime. This analysis will use the low-fidelity model of Section 4.3 and a newly developed low-fidelity unsteady aerodynamics code. The effect of coupling time step and flight velocity will be determined.

The general solution proceedure involves running a dynamic analysis at a given flight velocity and coupling time step to obtain the displacement history of the model. A representative node is then chosen that exhibits the dynamics of interest. The dynamics of that node are analyzed to determine if the amplitude of oscillation is

increasing or decreasing, and the primary frequency and damping ratio are determined. The primary goal of this first-order analysis is to determine if the ballute has the potential to flutter at the peak dynamic pressure point on the Titan aerocapture trajectory (presented in Section 5.1).

5.3.1 Engineering Estimate of Unsteady Aerodynamics

Many approximate methods for calculating surface pressures due to unsteady aerodynamics have been developed over the years. The most common of these is piston theory. A higher accuracy version (third order piston theory) was also explored for the moving boundary case because it had been shown by McNamara et al. [79] to produce superior results (compared to standard piston theory) for supersonic flutter solutions. However, piston theory requires a slender body and that the natural log of the Mach number times the vehicle thickness to length ratio ($\ln(MT)$) be less than unity. The minimum Mach number encountered by a clamped ballute at Titan is about 6 and the length is typically similar to its width, so $\ln(MT)$ is approximately 1.8, above the usable range of piston theory. The inaccuracy of static surface pressures predicted by piston theory with increasing velocity and bluntness was observed relative to modified Newtonian pressures and agrees with previous findings [68].

The pressure perturbation method of Hunter [50] was explored because it could be perturbed from a more accurate base pressure given by the modified Newtonian method. Unfortunately this method is also very inaccurate for blunt bodies since it is derived from the wave equation. Because neither piston theory nor the Hunter pressure perturbation method produce accurate surface pressures on blunt bodies, another method is needed for ballute analysis.

In this investigation, the local surface element velocity is added to the flow field velocity to determine a local pressure on each surface panel. This formulation produces the same pressure on an element moving at velocity $y+dy$ as it does for an

element on a body moving at velocity y with a perturbation velocity of dy, just as piston theory does in its realm of applicability. Calculation of pressure, heat transfer, and shear is then based on the local velocity at each element. The equations in Section 2.4.3 are then modified to use $\vec{V}_{local}$ instead of the free stream velocity.

$$\vec{V}_{local} = \vec{V}_{\infty} - \vec{V}_{element} \tag{5-1}$$

$|\vec{V}_{local}|$ is substituted for V_{∞} in Equation 2-6, and is used to compute M_{local} which is substituted for M_{∞} in Equation 2-5 in the continuum regime.

$$M_{local} = |\vec{V}_{local}|/\sqrt{\gamma RT} \tag{5-2}$$

The value of Ψ, used for the continuum heating, is left unchanged with the inclusion of $\vec{V}_{local}$ in the aerodynamics. In the rarefied regime, Equation 5-3 shows how the speed ratio, s, is updated to use $\vec{V}_{local}$, for substitution into Equations 2-1 to 2-3.

$$s_{local} = |\vec{V}_{local}|/\sqrt{2RT} \tag{5-3}$$

This method provides some damping due to the fluid, is valid for blunt bodies, and is straightforward to implement. Unfortunately, no applicable validation data was found.

5.3.2 Time Coupling

Loose coupling can be performed in a number of ways, including serial and parallel processing methods and using implicit or explicit time integration. Parallel methods can offer faster run times if the time required by each analysis code is similar; however, this is rarely the case when using CFD or DSMC for the aerodynamics. When the runtime is significantly different for each analysis code, and especially when each code is capable of running on multiple processors, serial methods have comparable speed to parallel methods and offer a substantially simpler implementation [28]. Implicit methods offer the allure of larger time steps due to increased stability, but often are

not faster due to the increased number of calculations required per time step to solve the matrix inversion problem [103].

The simple serial method [102] is the most straightforward explicit method to implement and iterates back and forth between the analysis codes. In this method, the time steps are synchronized between the aerodynamics and structural dynamics analyses. This produces correct results, but introduces energy errors due to the one-time-step lag in data transfer between the analysis codes. For example, each analysis code is run from time t to time $t+dt$, during which each code is using boundary conditions supplied from the other code at the previous time step. This method is first-order accurate in time and so requires very small time steps to maintain stability. The error introduced by this method is addressed by the improved serial staggered method developed by Farhat et al. [66].

The improved serial staggered (ISS) method is an explicit method that staggers time steps by one half between the analysis codes to improve the accuracy and increase the stability of the method. While no mathematical proof of time accuracy exists, test problems show that the method allows time steps of the size usually only possible with implicit methods [28] without requiring a matrix inversion, and has been shown to be significantly more accurate than other explicit methods for a given time step size [101]. Figure 5-4 shows the data flow and time stepping for the ISS method schematically. The method can also handle sub-cycling of either analysis making the coupling time step independent of the aerodynamic or structural dynamic time step. Several implicit methods [75, 90] and explicit methods [28] were investigated, but none offered the performance of the ISS method without significantly greater implementation complexity.

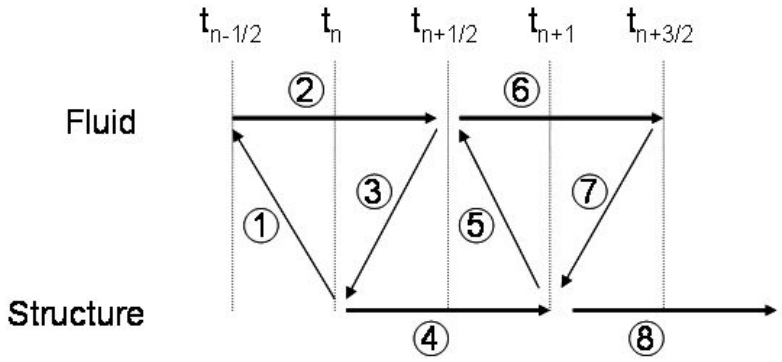

Figure 5-4: Schematic of the improved serial staggered time stepping algorithm.

5.3.3 Determination of Damping Ratio

The coupled analysis produces the displacement of each node in the model over time. This must be parsed for a node of interest and from that node's displacement history it must be determined if the amplitude of oscillations are decreasing, constant, or increasing (negative, zero, or positive damping, respectively). As the flight velocity increases, the point where the damping changes from negative to positive is considered the flutter boundary. Figure 5-5 shows a sample response and the frequency content of the response. Higher frequency oscillations are initially present in the data, but are much lower amplitude than the primary frequency, making the frequency of interest easier to determine. The damping observed in all cases is low, requiring more periods to determine the damping ratio accurately.

Several methods are available to determine the frequency and damping ratio, the most popular of which are logarithmic decrement analysis (LDA), Hilbert transform analysis (HTA), and moving block analysis (MBA). Naghipour et al. provide a good explanation of these methods in the context of modal testing of beams [96]. Smith and Wereley compared these methods on a known signal with varying amounts of noise and found the HTA method to produce the best damping ratio at all levels of noise [108]. These three methods are implemented for this work, with HTA being the primary source of damping and frequency data and with the other two used as sanity

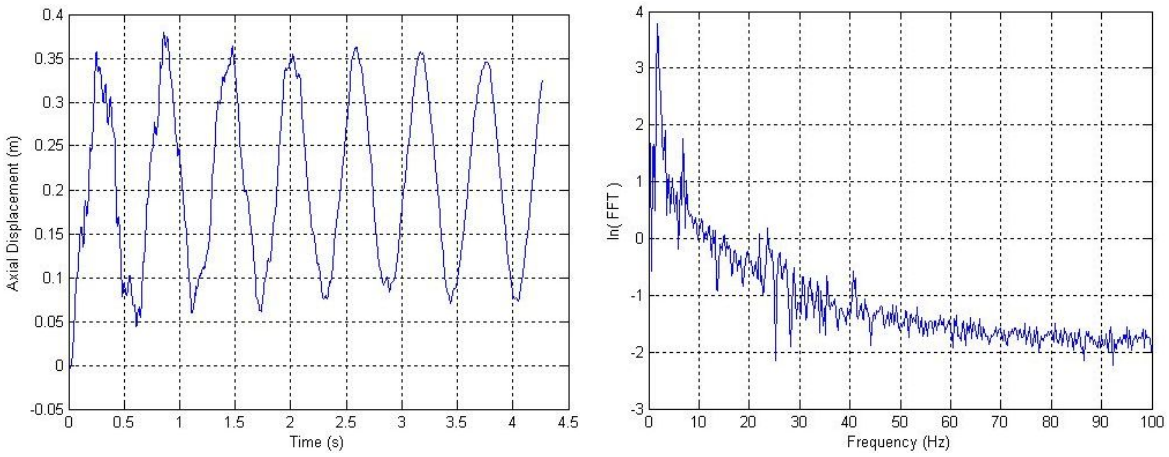

(a) Response of a torus LE node.

(b) Frequency spectrum of the response.

Figure 5-5: The response and frequency spectrum of a node on the leading edge of the torus. A single frequency, at 1.75 Hz, dominates the response.

checks.

Logarithmic decrement analysis is the most intuitive method, since the sign of the damping ratio can often be observed by plotting the natural log of the amplitude of successive peaks. If the natural log of the amplitude is plotted over time, a line can be fit using least squares regression, with the slope of this line being the damping ratio times the natural frequency. If the frequency of the peaks is known, then the damping ratio can be found. Since the oscillation is not about zero, the amplitude is calculated by dividing the difference between the peak value and the following minimum value by two. Any noise in the data can invalidate this method since the output is dependent on only a handful of points from the data set. The method usually evaluates the sign of the damping ratio properly, but often the value of the damping ratio is significantly different than the HTA or MBA methods, and so is useful only to determine if the amplitude is growing.

Hilbert transform analysis produces an envelope signal that is useful for determining the instantaneous properties of the signal [119], which can be averaged or curve-fit to obtain net behavior. The slope of a straight line fit to the instantaneous values

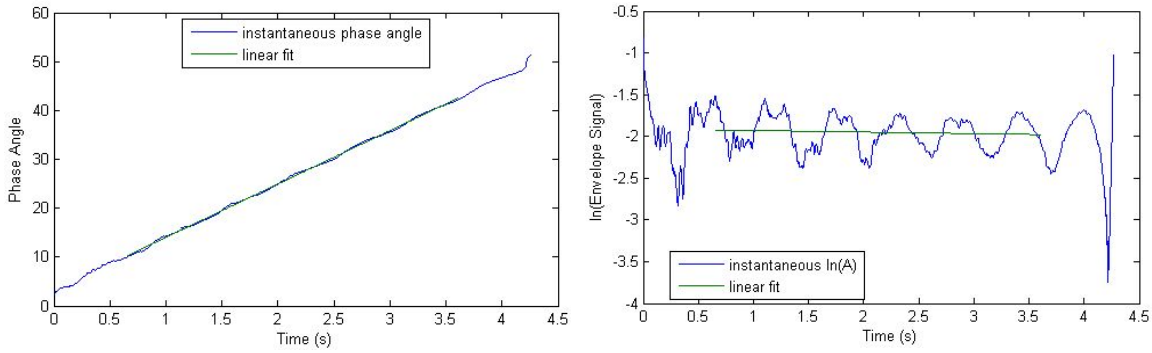

Figure 5-6: Noise at the end of the envelope and phase signals in HTA often requires that points be ignored to obtain a good curve fit.

is the damping ratio times the natural frequency [119]. The damped frequency can be found by fitting a curve to the slope of the phase of the transformed signal [108]. Noise near the end of the envelope signal and phase (Figure 5-6) often require that several points in the data set be neglected to obtain the best results.

Moving block analysis was introduced in the 1970s, and one of the first applications published was by Hammond and Doggett [45]. The concept involves breaking the response into sequential blocks and finding the magnitude of each using the fast Fourier transform (FFT). A curve is fit to the resulting magnitudes, and the slope is the damping ratio times the natural frequency. The process is shown pictorially in Figure 5-7. The process used here differs slightly in that the frequency is known from the application of HTA. The precise block length is important in determining the magnitude [45, 16], and so the block length is calculated by finding the discrete frequencies represented by an FFT of length N. The length, N, is varied and the block length that can represent the desired frequency the closest is used in the analysis.

The three methods discussed here, LDA, HTA, and MBA, were implemented as MATLAB functions to increase analysis speed and to avoid user errors. Run times for all three methods are under one minute, and are negligible compared to the aeroelastic computations.

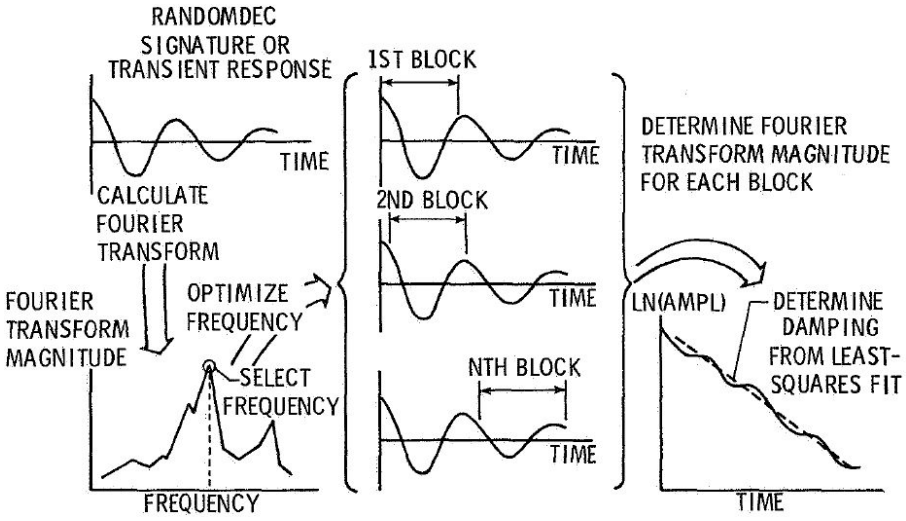

Figure 5-7: Schematic of the MBA method [45].

5.3.4 Dynamic Results

Dynamic analysis of the clamped ballute model was run using the Fine3 structural grid from Section 4.2.4, and the engineering estimate of unsteady aerodynamics of Section 5.3.1. The model initially inflates the torus, then rapidly applies the aerodynamic load, which initiates oscillation in the model.

Analysis was run at several flight velocities ranging from 4,266 m/s at the peak dynamic pressure point on the trajectory up to 5,200 m/s, and at three different coupling time step sizes; 0.01, 0.005, and 0.0025 seconds. Due to the limited number of restarts possible with LS-DYNA on the linux platform, for most runs the total simulated time was limited to the time step size times 1000. Table 5-2 shows the run time in seconds for each dynamic case that was computed.

The lowest frequency observed in the ballute is an axial oscillation of the torus, which is captured in the displacement history of a node on the leading edge of the torus (node 65524 in the structural model). A second oscillation was observed in the conical membrane at a higher frequency and is captured by the displacement history of a node in the middle of the conical membrane (node 32520 in the structural model). The locations of both tracked nodes are shown in Figure 5-8 along with arrows indicating

Table 5-2: Time lengths of the dynamic ballute simulations in seconds. Simulation time decreases with time step size due to restart limits in LS-DYNA and compute time.

Flight Velocity (m/s)	**Time Step Size (s)**		
	0.01 s	**0.005 s**	**0.0025 s**
4,266	4.28	4.145	3.6225
4,800	5.01	4.145	2.4975
4,900	4.28	4.245	2.4975
5,000	3.09	4.250	2.4975
5,100		4.350	2.4600
5,200		4.990	
5,300		4.630	
5,400		4.295	

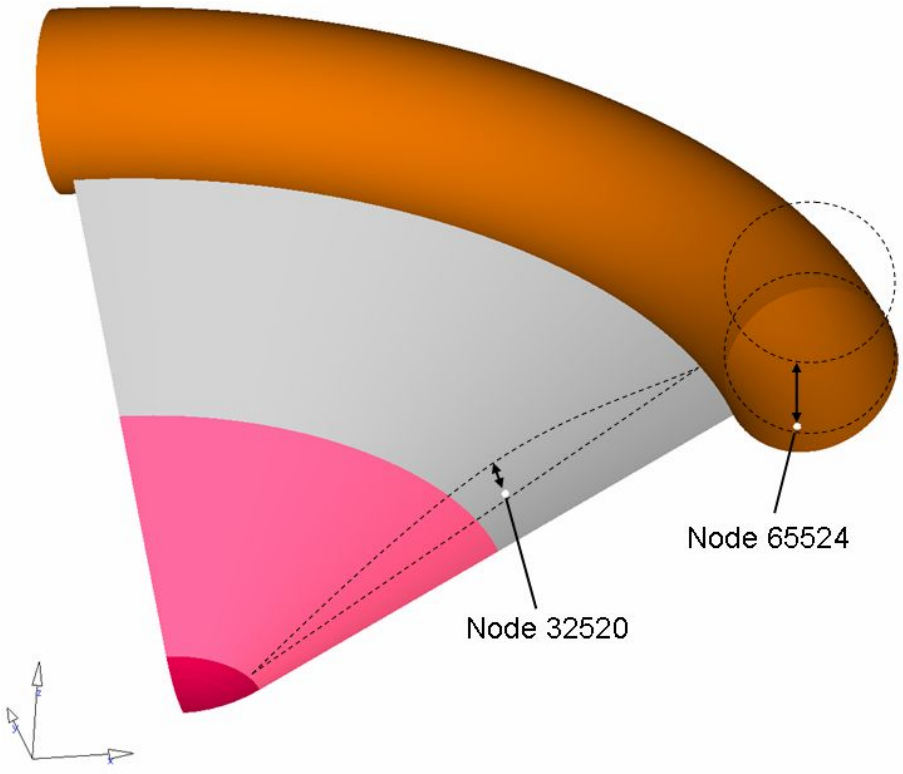

Figure 5-8: Location of nodes used to capture the two primary frequencies observed.

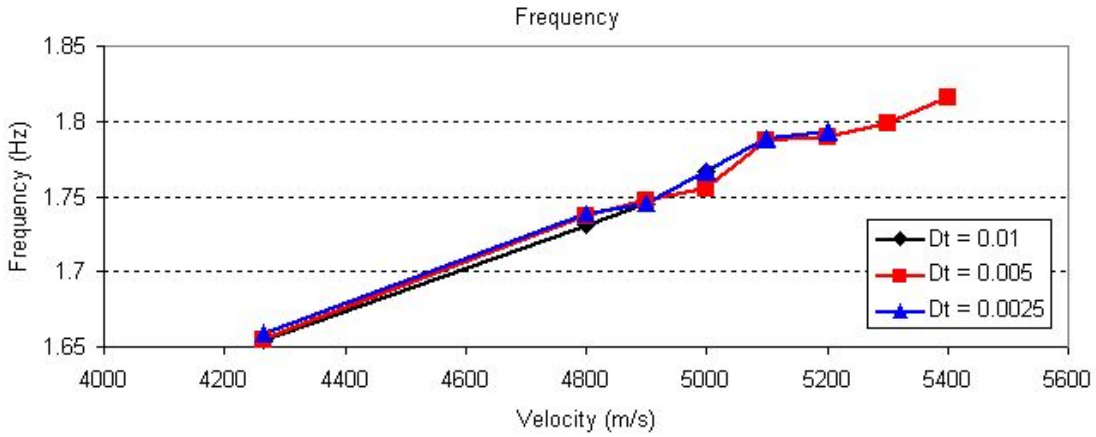

Figure 5-9: The frequency of axial oscillation increases roughly linearly with flight velocity.

the direction of oscillation at each point.

Analysis of the dynamic response at node 65524 indicates that this mode is damped at the peak dynamic pressure point at all time step sizes using all analysis methods except for MBA at a time step of 0.01 s. Observation of the response at 4,266 m/s and all time step sizes indicates that the amplitude of oscillation is decreasing, indicating that MBA incorrectly characterized the motion. At higher velocities, some correlation is observed between the different time step sizes, though a time step of 0.01 s appears to be insufficient to capture the damping effect of the fluid. Even with smaller step sizes, the damping appears to be increasing with decreasing time step size, indicating that smaller timesteps are still needed. Figure 5-9 shows the frequency of the axial motion, to be between 1.65 Hz and 1.85 Hz. Unfortunately, due to restrictions in LS-DYNA and the available hardware, smaller step sizes allow less than 1.5 s of response to be computed, which does not capture enough of the response at node 65524 to determine the damping ratio (less than 3 cycles).

Figure 5-10 shows the damping ratio to be negative for time step sizes of 0.005 and 0.0025 s, and at all velocities except for 4,900 and 5,100 m/s as computed using MBA. At 4,900 and 5,100 m/s the results are less clear, with MBA indicating positive

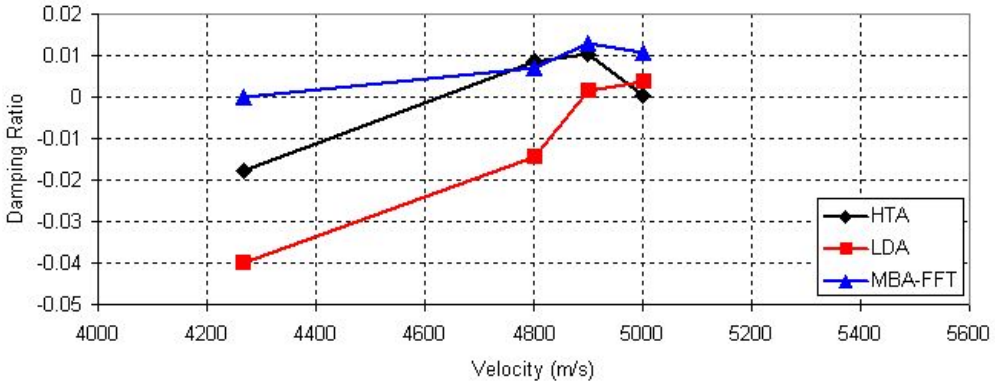

(a) Time step = 0.01 s.

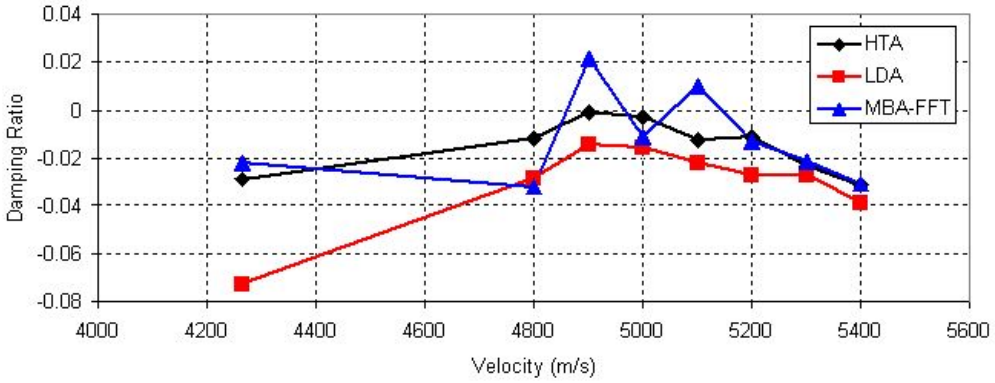

(b) Time step = 0.005 s.

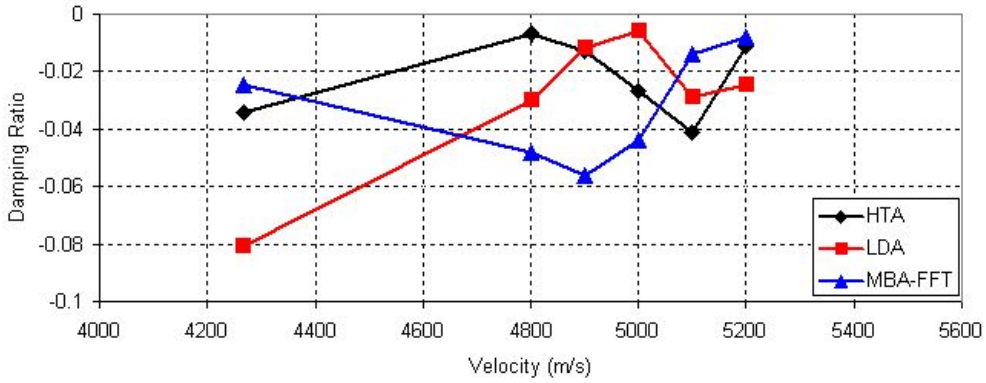

(c) Time step = 0.0025 s.

Figure 5-10: Damping ratio for axial motion of the torus.

damping, HTA indicating approximately zero damping, and LDA indicating negative damping for a time step size of 0.005 s, while all methods predict negative damping for a time step size of 0.0025 s. Figure 5-11 shows the response of node 65524 and the natural log of the amplitudes from LDA. At both velocities, the amplitude is decreasing in time, indicating that the damping ratio should be negative, as predicted by HTA and LDA at dt = 0.005 and 0.0025 s. With the damping ratio decreasing with decreasing time step size and all velocities analyzed showing decreasing amplitude in time, this mode does not flutter in the velocity range explored.

Analysis of the dynamic response at node 32520 indicates that the response is damped at all velocities analyzed. Figure 5-12 shows the calculated damping ratios, and Figure 5-13 shows that the frequency ranges from 6 Hz up to 7 Hz as the velocity is increased from 4,266 m/s up to 5,400 m/s. For this mode, the damping ratios are very similar at the three computed time step sizes, indicating convergence with respect to time step size. Within a reasonable velocity range of the peak dynamic pressure point, this mode does not flutter.

5.3.5 Summary of Low-Fidelity Analysis at Titan

Low-fidelity static and dynamic analysis was performed on a clamped ballute at Titan. Static analysis was performed at 17 points on an aerocapture trajectory, and demonstrated that coupled analysis is only meaningful when the dynamic pressure is above 1 Pa. Analysis at higher dynamic pressures shows that stresses and deformation are correlated to dynamic pressure, with the peak stress and axial displacement of the torus occuring at peak dynamic pressure. The peak stresses are well below the ultimate stress of Upilex, so some optimization may be possible while maintaining sufficient margins.

Dynamic analysis of the clamped ballute was performed at the peak dynamic pressure point on the Titan aerocapture trajectory and at velocities up to 5,400 m/s

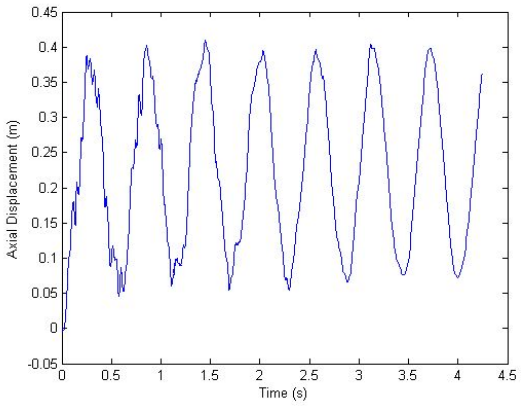

(a) Response at velocity = 4,900 m/s.

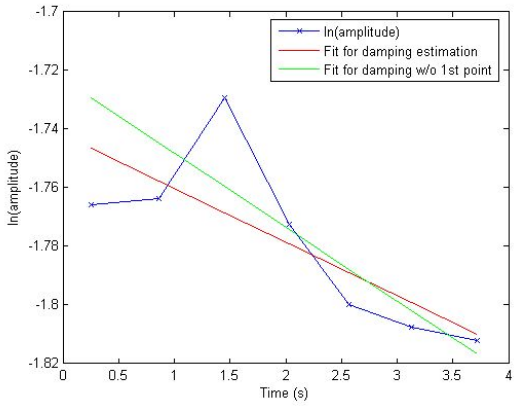

(b) LDA result at velocity = 4,900 m/s.

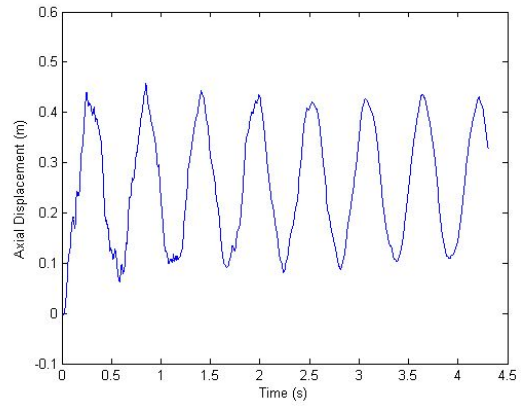

(c) Response at velocity = 5,100 m/s.

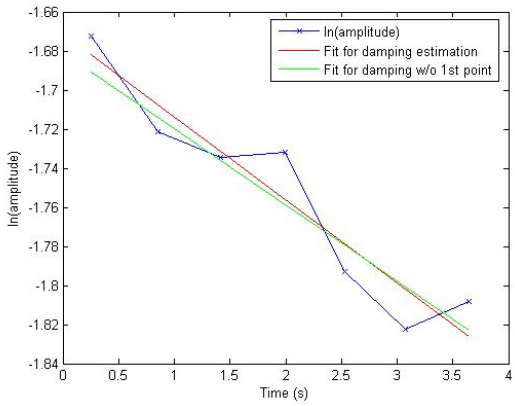

(d) LDA result at velocity = 5,100 m/s.

Figure 5-11: Response and ln(amplitude) of node 65524 for dt = 0.005 s at 4,900 and 5,100 m/s. LDA indicates that the damping ratio is negative.

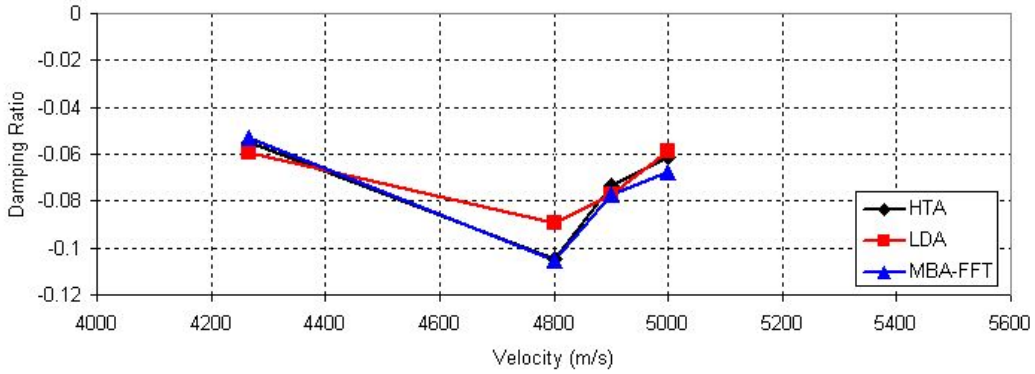

(a) Time step = 0.01 s.

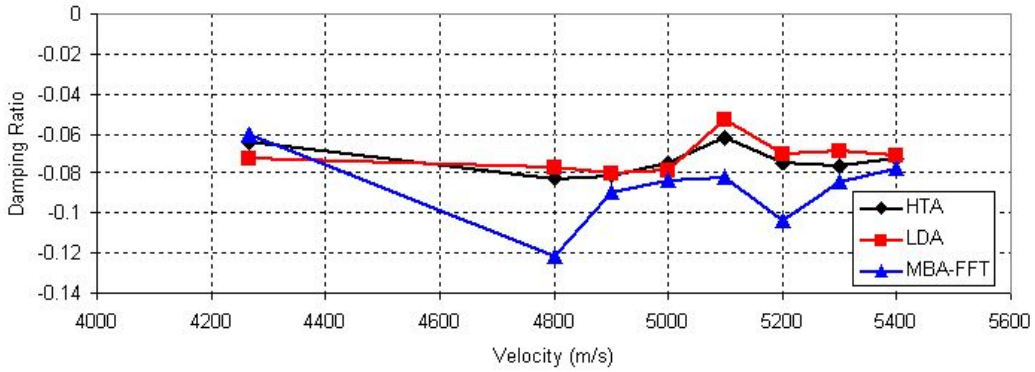

(b) Time step = 0.005 s.

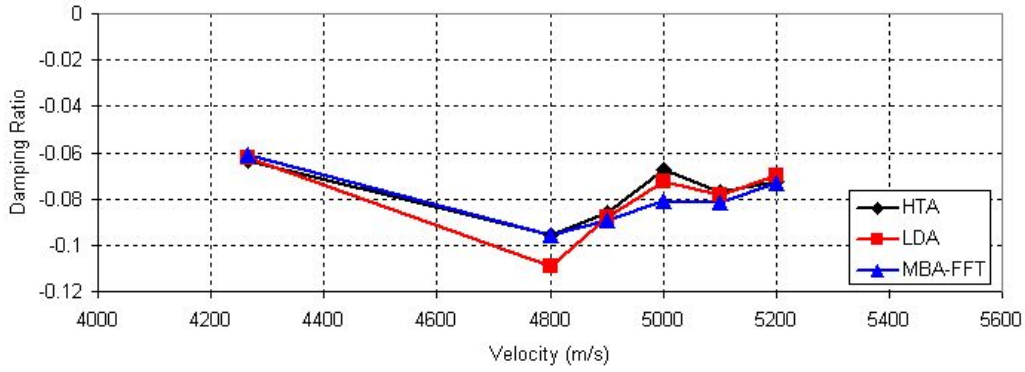

(c) Time step = 0.0025 s.

Figure 5-12: Damping ratios for flapping of the conical membrane.

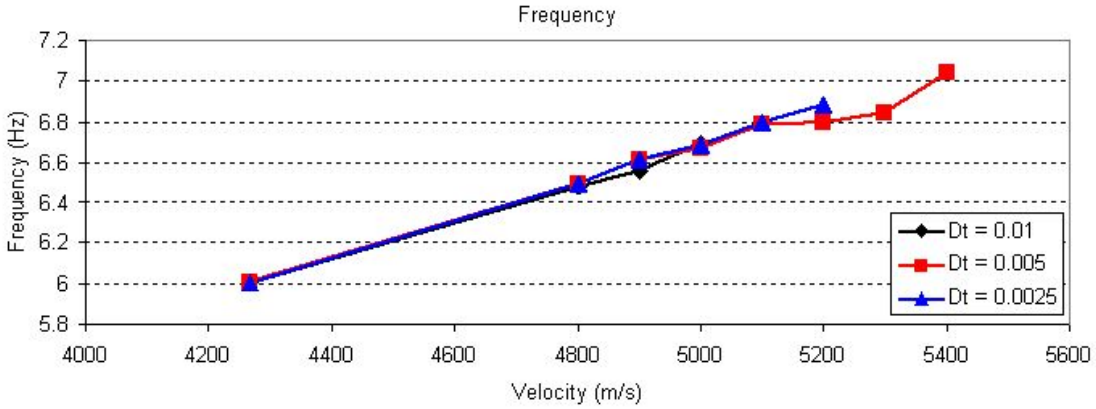

Figure 5-13: The frequency of oscillation increases roughly linearly with flight velocity at node 32520.

to determine if the ballute would experience flutter. The two lowest frequency modes were identified as axial motion of the torus at approximately 1.75 Hz and flapping of the conical membrane at 6.5 Hz. In the range of velocities studied, neither mode flutters. Overall, low-fidelity analysis indicates feasibility of ballute aerocapture at Titan with minor modifications.

CHAPTER VI

SUMMARY AND FUTURE WORK

6.1 Conclusions

This research effort has developed the variable-fidelity Ballute Aeroelastic Analysis Tool (BAAT), an aeroelastic design framework for thin-film ballutes. The code uses LS-DYNA for structural analysis and obtains aerodynamic pressures from either NASCART-GT, DAC, or MBSA, depending on the fidelity desired and the flight regime.

BAAT was validated using wind tunnel test data from a 6 inch diameter flexible kapton model in the hypersonic CF_4 wind tunnel at Mach 5.6. The deformed shape of the vehicle forebody was predicted using both low- and high-fidelity analysis in the continuum regime. During the solution process it was found that the deformed shape was more sensitive to structural parameters than to the aerodynamic load distribution. The computed deformed shape using both the low- and high-fidelity analysis matched the experiment very well.

High-fidelity analysis solutions of a clamped ballute were computed at two conditions on a Titan aerocapture trajectory using NASCART-GT or DAC coupled to LS-DYNA. The flight conditions selected were at the peak dynamic pressure point (continuum regime) and in the high transitional regime just after encountering the atmosphere. These solutions represent the first published aeroelastic solutions of a thin-film ballute using inviscid, perfect gas aerodynamics.

Low-fidelity solutions were computed and compared to the high-fidelity analyses at the same two points on a Titan aerocapture trajectory using a thin-film clamped ballute. Analysis at the peak dynamic pressure point showed good agreement of

stresses and drag, despite a nearly 70% difference in axial displacement of the torus. The difference was attributed to a difference in load distribution on the torus that resulted in only an 8% difference in drag. Analysis at the transitional point produced drag within 13% for the low- and high-fidelity results, but a large discrepancy in predicted stresses and torus displacement. From a design perspective, the large discrepancy in predicted stresses and torus displacement is not a problem because the stresses at this point does not drive structural considerations, and the drag prediction is within reason (despite the difference in deformed shape) for use in conceptual design. Furthermore, the low-fidelity analysis is between 4 and 35 times faster than comparable high-fidelity analysis (depending on the flight regime).

Given that the low-fidelity analysis can predict the peak stress on the trajectory and the aerodynamic drag along the trajectory within 15% for the clamped ballute geometry studied, low-fidelity analysis was used to demonstrate the trends along a Titan aerocapture trajectory. The results showed that analysis at dynamic pressures less then 1 Pa do not produce meaningful results, but demonstrate that there are potential issues with the ballute recontacting the spacecraft at high altitudes. The addition of supports for the torus would aleviate this problem and it is recommended that they be included in future studies. At higher dynamic pressures (> 1 Pa), stresses and displacements are correlated to dynamic pressure. The peak stress in the ballute occurs at peak dynamic pressure and is approximatley one third the ultimate stress at the estimated temperature of 200°C. With such a large margin of safety, the ballute could likely be lightened without compromising its structural integrity.

Dynamic analysis was performed using a low-fidelity structural model and an engineering estimate of unsteady aerodynamics at the peak dynamic pressure point on the Titan aerocapture trajectory. Two modes were found: the first is an axial oscillation of the torus at approximately 1.75 Hz, and the second is a flapping of the conical membrane at approximately 6.5 Hz. Analysis indicates that neither of

the first two modes flutter at speeds between 4,266 m/s (the peak dynamic pressure point) and 5,400 m/s.

The analysis presented shows that low-fidelity analysis is sufficient to predict the peak stress on the trajectory and the drag along the trajectory for conceptual design of the thin-film clamped ballute geometry studied. When the analysis time is compared relative to the accuracy gained, the low-fidelity analysis methods are especially attractive.

From a conceptual design prespective, both the low- and high-fidelity analysis presented indicates that the thin-film clamped ballute studied could survive the Titan aerocapture environment from an aeroelasticity perspective. The peak stress level is well below the ultimate stress of Upilex, no buckling is observed, and dynamic analysis indicates that flutter will not occur at the peak dynamic pressure point. Analysis at low dynamic pressures indicates that contact between the spacecraft and conic membrane is possible, and it is recommended that future studies support the torus after deployment.

6.2 Limitations of Low-Fidelity Analysis

The low-fidelity solution process demonstrated good results for the analysis of a clamped ballute, but there are limitations to the low-fidelity approach. Limitations include the lack of flowfield unsteadiness and shock-shock interaction, the inability to compute radiative heating, and improper fluid damping in dynamic analysis.

Due to the simple geometry of the clamped ballute, unsteadiness in the flowfield was not a factor in this analysis. For a geometry such as a trailing ballute, unsteadiness could be a driver in dynamic analysis. A time-accurate CFD code would be needed for this type of analysis. The clamped ballute at Titan also did not have any locations where shocks interacted, which is much more important for a trailing ballute, and drives the unsteadiness in the flow. Again, high-fidelity analysis would

be needed to resolve these problems.

Convective heat rate calculations using the low-fidelity aerodynamics model are reasonably accurate for the stagnation point of the body, and can be extended to simple surfaces. However, problems arise when the body has a recess in it (such as the torus attach point on the clamped ballute) or localized heating due to shock-shock interaction. This study estimates surface temperature from other analysis, but accurate computation of heat rate and surface temperature requires that viscosity and chemistry be included in the flow calculations.

When tackling a new problem, care must be taken to ensure that the problem being solved does not violate the assumptions of low-fidelity analysis. However, if a good solution is possible with low-fidelity analysis, great amounts of time can be saved.

6.3 Suggestions for Future Work

The presented analysis is complete and represents a first step toward the potential of the BAAT software. The addition of high temperature effects and thermal analysis would improve the accuracy of the current capabilities of BAAT. In addition, incorporating moving boundary conditions into NASCART-GT and adding six degree-of-freedom (DOF) equations of motion (EOM) would improve the capability of the tool.

6.3.1 High Temperature Aerothermodynamic Effects

The Mach number on the Titan aerocapture trajectory used in Section 5.1 is from 9 up to 21. In this speed range temperatures behind a shock (in air at 52 km altitude at Earth) are between 2,000 K and 6,000 K, high enough to begin dissociating molecular Nitrogen [6]. Since the Titan atmosphere is primarily composed of Nitrogen and the flow speed is high, the flow will be in thermochemical nonequilibrium.

The nonequilibrium flow will result in a thin shock layer, changing the surface

pressure distribution and the location of any shock-shock interactions. Furthermore, knowing the chemical constituents and state of molecules in the flow would allow computation of thermal radiation to the surface. Including thermochemical nonequilibrium effects would provide accurate convective heating and the ability to calculate radiative heating.

Adding nonequilibrium to BAAT requires implementing finite rate chemical reaction equations in NASCART-GT and the addition of rate equations for the Titan atmosphere to DAC. A chemical kinetics model for the Titan atmosphere is available from Gökçen [36], but has not been implemented in either NASCART-GT or DAC. To properly capture the surface heat rate, the boundary layer must also be modeled in NASCART-GT using either the Navier Stokes equations or the integral boundary layer method.

6.3.2 Thermal Response Analysis & Coupled Aero-Thermo-Elasticity

Temperature dependent material properties were shown to have a substantial affect on the deformed shape of the wind-tunnel test model in Section 3.3, and would likely affect the results of a dynamic aeroelastic analysis by altering the material elasticity and geometry. In the current analysis, the temperature of the material is assumed to be the same over the entire model, and is approximated from either test data or extrapolation of thermal analysis of similar configurations.

The addition of thermal analysis requires accurate heat fluxes to the surface, thermal material properties, and environmental conditions. Once high temperature effects are available in NASCART-GT, accurate convective heat fluxes will be available from the high-fidelity analysis. Obtaining the total heat flux, including both convective and radiative heating, would require NASCART-GT and DAC to be coupled to a radiation equilibrium code. To date there are no published papers that compute radiative heating in the high altitude, rarefied environment where ballutes

decelerate, but it is expected that radiative heating will be substantial given the large shock standoff distance observed in this flight regime, and the large influence of CN radiation at lower altitudes on smaller bodies at Titan [98, 131].

Coupling the thermal analysis code will require executing two analyses: one to calculate the view factors to space and every other element in the model and another to perform the thermal analysis. The thermal analysis codes available can generally be run from the command line and utilize file input/output, making them easy to interface. Furthermore, the thermal analysis will run quickly compared to the structural or aerodynamic analysis and so does not slow the analysis significantly. Computing the view factors, however, is often done via a graphical user interface and the actual analysis is very time consuming. However, since the geometry of the ballute does not change very fast, the analysis may not need to be executed for every iteration. A metric could be developed to determine when the view factors need to be recomputed based on the average movement of the model.

To obtain accurate material temperatures the surface emissivity and material conductance must be known. These parameters are often available at room temperature, but they vary with temperature and surface preparation and so testing must be performed to obtain the proper values for the material over a large temperature range.

Once surface temperatures are available, the structural model must be adapted to include temperature dependent material properties. The primary effects of temperature on the structural model are thermal expansion and changing modulus. LS-DYNA has exhibited some numerical problems when thermal expansion is included and this problem must be solved for the addition of thermal analysis to be useful.

6.3.3 High-Fidelity Dynamic Aeroelastic Analysis

The dynamic aeroelastic solutions presented in this work rely on a first-order engineering approximation of the unsteady aerodynamics. This method approximates

the damping due to the fluid, but cannot capture unsteadiness in the flow or shock-shock interactions. In Section 3.4, it was observed that shock-shock interactions exist near the body and produce a concentrated region of high pressure that is not captured by the low-fidelity aerodynamics. In the case of a trailing ballute, shock-shock and shock-wake interactions play a large part in determining the flow field, making high-fidelity analysis more important.

Adding high-fidelity dynamic analysis to BAAT requires the addition of moving boundary conditions to NASCART-GT. Due to the Cartesian grid used in NASCART-GT, implementing moving boundary conditions requires re-cutting the boundary cells and then refining the grid around the new boundary cells at each time step, which is a computationally intensive process. The addition of moving boundary conditions could potentially accelerate convergence for static deformed cases since the deformed boundary could be updated without having to restart the analysis and let the flow field develop to a steady state at each coupling iteration.

The likelihood of an aeroelastic phenomena such as flutter occurring increases with dynamic pressure, making the peak dynamic pressure point the most likely location on a ballute trajectory. Since this point is in the continuum regime at Titan, only NASCART-GT requires moving boundary conditions. If a ballute trajectory were designed to have the peak dynamic pressure occur in the transitional regime, DAC would need to be modified to handle moving boundary conditions. Since DAC has been optimized to produce static solutions with minimum computation time, the code authors (G.J. Lebeau and F.E. Lumpkin, III of NASA Johnson Space Center) estimate that it would require at least one man-year for a good programmer to implement moving boundary conditions. Alternatively, other DSMC programs could be explored.

6.3.4 6-DOF Dynamics

Prior to flight, questions about entry vehicles dynamic stability must be addressed. Ballutes will have to demonstrate dynamic stability and questions about gust response as do parachutes. For hardshell entry capsules these types of questions are answered with 6 DOF trajectory analysis and an aerodynamic database. Ballutes present a special challenge due to their flexibility, because both the geometry and orientation can change. Creating an aerodynamic database for this type of problem will be difficult and may reqire the aerodynamic response to be calculated for each time step in the trajectory analysis.

Including this analysis in BAAT would require that the current table lookup method used to determine the flight conditions be replaced by a 6 DOF trajectory code. This change was anticipated when the code was writen and will require that only a small part of the code be modified. The aerodynamic methods used can already handle arbitrary flow direction, but a mechanism for ensuring that the grid domain is large enough to enclose the deformed body may be necessary for NASCART-GT and DAC.

Computational dynamic stability analysis using high-fidelity aerodynamics would currently push the limits of even the fastest computers. Verifying the approximate methods will be the most efficient method of obtaining solutions in the near future.

6.3.5 Validation Data

This work used the ISP wind tunnel test model for validation. The model provides profile displacement data of a flexible body in a hypersonic flow, but is relatively stiff compared to proposed ballutes, and does not provide stress or three-dimensional displacement data. Furthermore, no time-accurate data is available for validation of dynamic analysis and flutter onset.

Wind tunnel tests or sounding rocket tests using scale models of inflated ballutes

could provide the data necessary for tool validation. The models would need to be of reasonable size relative to the material stiffness available and completely supported by their inflation pressure while being allowed to move freely about the spacecraft attachment point for either a clamped or trailing ballute. Time-accurate position data would need to be captured at many points on the surface. Several tests would be necessary to determine the dynamic pressure at which flutter occurs. This data would allow validation of BAAT in the dynamic regime and would provide a data point for flutter analysis validation.

REFERENCES

[1] ABAQUS, Inc., *ABAQUS Documentation*, 6.4 ed., 2003.

[2] Abe, T., "A self-consistent tension shell structure for application to aerobraking vehicle and its aerodynamic characteristics," 24th AIAA/ASME/SAE/ASEE Joint Propulsion Conference, Boston, MA, July 11-13 1988.

[3] Alexander, W., "A discussion of governing decelerator performance and design parameters in the supersonic flight regime," AIAA Paper 68-938, AIAA Aerodynamic Deceleration Systems Conference, El Centero, CA, Sep. 23-25 1968.

[4] Alexander, W. and Lau, R., "State-of-the-art study for high-speed deceleration and stabilization devices," Tech. Rep. NASA-CR-66141, NASA, Sept. 1966.

[5] Anderson, B., "Computational continuum and rarefied flow results for ballute applications," AIAA Paper 2004-292, 42nd AIAA Aerospace Sciences Meeting and Exhibit, Reno, NV, Jan. 5-8 2004.

[6] Anderson, J.D., J., *Hypersonic and High Temperature Gas Dynamics*. Reston, VA: American Institute of Aeronautics and Astronautics, 2000.

[7] Anderson, M., Bush, H., Fralich, R., and Robinson, J., "A tension shell structure for application to entry vehicles," Tech. Rep. NASA-TN-D-2675, NASA, Mar. 1965.

[8] Anderson, R., "Structures technology - 1964," *Astronautics & Aeronautics*, vol. 2, no. 12, pp. 14–20, 1964.

[9] Andrews, D. and Bloetscher, F., "Aerobraked orbital transfer vehicle definition," AIAA Paper 81-0279, 19th AIAA Aerospace Sciences Meeting, St. Louis, MO, Jan. 12-15 1981.

[10] ANSYS, Inc., *ANSYS User's Manual*, 9 ed., 2004.

[11] Bartels, R., Moses, R., Scott, R., Templeton, J., Cheatwood, F., Gnoffo, P., and Buck, G., "A proposed role of aeroelasticity in NASA's new exploration vision," Paper IF-013, DGLR International Forum on Aeroelasticity and Structural Dynamics, Munich, Germany, Jun. 28-Jul. 1 2005.

[12] Bauchau, O. and Ahmad, J., "Advanced CFD and CSD methods for multidisciplinary applications in rotorcraft problems," AIAA Paper 96-4151, 6th NASA and ISSMO Symposium on Multidisciplinary Analysis and Optimization, Bellevue, WA, Sep. 4-6 1996.

[13] Baum, J., Lua, H., Mestreau, E., Sharov, D., Lohner, R., Plessone, D., and Charman, C., "Recent developments of a coupled CFD/CSD methodology," AIAA Paper 2001-2618, 15th AIAA Computational Fluid Dynamics Conference, Anaheim, CA, June 11-14 2001.

[14] Bhardwaj, M., Kapania, R., Reichenbach, E., and Guruswamy, G., "Computational fluid dynamics/computational structural dynamics interaction methodology for aircraft wings," *AIAA Journal*, vol. 36, no. 12, 1989.

[15] Bird, G., *Molecular Gas Dynamics and the Direct Simulation of Gas Flows*. New York, NY: Oxford University Press, 1994.

[16] Bousman, W. and Winkler, D., "Application of the moving-block analysis," AIAA Paper 1981-0653, 22nd AIAA Structures, Structural Dynamics, and Materials Conference, Atlanta, GA, April 6-8 1981.

[17] Braun, R. and Powell, R., "Aerodynamic requirements of a manned mars aerobraking transfer vehicle," *Journal of Spacecraft and Rockets*, vol. 28, no. 4, pp. 361–367, 1991.

[18] Braun, R., Powell, R., and Lyne, J., "Earth aerobraking strategies for manned return from mars," *Journal of Spacecraft and Rockets*, vol. 29, no. 3, pp. 297–304, 1992.

[19] Brown, G. and Richardson, E., "Minimum-mass design for Titan aerocapture," AIAA Paper 2005-1637, 18th AIAA Aerodynamic Decelerator Systems Technology Conference and Seminar, Munich, Germany, May 2005.

[20] Buck, G., "Testing of flexible ballutes in hypersonic wind tunnels for planetary aerocapture," AIAA Paper 2006-1319, 44th AIAA Aerospace Sciences Meeting and Exhibit, Reno, NV, Jan. 9-12 2006.

[21] Charczenko, N. and McShera, J.T., J., "Aerodynamic characteristics of towed cones used as decelerators at Mach numbers from 1.57 to 4.65," Tech. Rep. NASA-TN-D-994, NASA, Dec. 1961.

[22] Clark, I., Braun, R., Theisinger, J., and Wells, G., "An evaluation of ballute entry systems for lunar return missions," AIAA Paper 2006-6276, AIAA Atmospheric Flight Mechanics Conference and Exhibit, Keystone, CO, Aug. 21-24 2006.

[23] Couch, L., "Drag and stability characteristics of a variety of reefed and unreefed parachute configurations at Mach 1.80 with an empirical correlation for supersonic Mach numbers," Tech. Rep. NASA-TR-R-429, NASA, Feb. 1975.

[24] Cruz, J. and Lindgard, J., "Aerodynamic decelerators for planetary exploration: Past, present, and future," AIAA Paper 2006-6792, AIAA Guidance, Navigation, and Control Conference and Exhibit, Keystone, CO, Aug. 21-24 2006.

[25] Cruz, M., "The aerocapture vehicle mission design concept - aerodynamically controlled capture of payload into Mars orbit," AIAA Paper 1979-0893, Conference on Advanced Technology for Future Space Systems, Hampton, VA, May 8-10 1979.

[26] "Summary properties for Kapton polyimide films," Tech. Rep. H-38492-1, DuPont Corp., Mar. 1997.

[27] "DuPont Kapton HN: Polyimide film," Tech. Rep. K-15345, DuPont Corp., Mar. 2006.

[28] Farhat, C. and Lesoinne, M., "Two efficient staggered algorithms for the serial and parallel solution of three-dimensional nonlinear transient aeroelastic problems," *Computer Methods in Applied Mechanics and Engineering*, vol. 182, no. 3-4, pp. 499–515, 2000.

[29] French, J. and Cruz, M., "Aerobraking and aerocapture for planetary missions," *Astronautics & Aeronautics*, vol. 18, no. 2, pp. 48–55, 1980.

[30] Gillis, C., "Deployable aerodynamic decelerators for space missions," *Journal of Spacecraft and Rockets*, vol. 6, no. 8, pp. 885–890, 1969.

[31] Gnoffo, P., "An upwind-biased, point-implicit relaxation algorithm for viscous compressible perfect gas flows," Tech. Rep. NASA-TP-2953, NASA, Feb. 1990.

[32] Gnoffo, P., "Planetary-entry gas dynamics," *Annual Review of Fluid Mechanics*, vol. 31, pp. 459–494, 1999.

[33] Gnoffo, P., "Computational aerothermodynamics in aeroassist applications," *Journal of Spacecraft and Rockets*, vol. 40, no. 3, pp. 305–312, 2003.

[34] Gnoffo, P. and Anderson, B., "Computational analysis of towed ballute interactions," AIAA Paper 2002-2997, 8th AIAA/ASME Joint Thermophysics and Heat Transfer Conference, Saint Louis, MO, June 24-26 2002.

[35] Gnoffo, P., Gupta, R., and Shinn, J., "Conservation equations and physical models for hypersonic air flows in thermal and chemical nonequilibrium," Tech. Rep. NASA-TP-2867, NASA, 1989.

[36] Gökçen, T., "N_2-CH_4-Ar chemical kinetic model for simulations of atmospheric entry to Titan," AIAA Paper 2004-2469, 37th AIAA Thermophysics Conference, Portland, OR, June 28-July 1 2004.

[37] Graesslin, M. and Schoettle, U., "Flight performance evaluation of the re-entry mission IRDT-1," IAF Paper 01-V305, 52nd IAF International Astronautical Congress, Toulouse, France, Oct. 1-5 2001.

[38] Graham, Jr., J., "Development of ballute for retardation of Arcas Rocketsondes," Tech. Rep. AFCRL-65-877, U.S. Air Force, Dec. 1965.

[39] Grenich, A. and Woods, W., "Flow field investigation of atmospheric braking for high drag vehicles with forward facing jets in spacecraft entry," AIAA Paper 81-0293, 19th AIAA Aerospace Sciences Meeting, Saint Louis, MO, Jan. 12-15 1981.

[40] Guruswamy, G., "Coupled finite-difference/finite-element approach for wing-body aeroelasticity," AIAA Paper 92-4680, 4th AIAA/USAF/NASA/OAI Symposium on Multidisciplinary Analysis and Optimization, Cleveland, OH, Sep. 21-23 1992.

[41] Guy, L., "Structural and decelerator design options for Mars entry," *Journal of Spacecraft and Rockets*, vol. 6, no. 1, pp. 44–49, 1969.

[42] Hall, J., "A review of ballute technology for planetary aerocapture," Paper IAA-L-1112, 4th IAA Conference on Low Cost Planetary Missions, Laurel, MD, May 2-5 2000.

[43] Hall, J. and Le, A., "Aerocapture trajectories for spacecraft with large, towed ballutes," in *Advances in the Astronautical Sciences*, vol. 108 II, pp. 1857–1872, Univelt Inc., San Diego, CA, 2001.

[44] Hall, J., Noca, M., and Bailey, R., "Cost-benefit analysis of the aerocapture mission set," *Journal of Spacecraft and Rockets*, vol. 42, no. 2, pp. 309–320, 2005.

[45] Hammond, C. and Doggett Jr., R., "Determination of subcritical damping by moving-block/randomdec applications," in *Flutter Testing Techniques*, pp. 59–76, NASA-SP-415, 1975.

[46] Heitchue, R., "Emergency space station escape system consisting of retrorocket, expandable reentry structure, life support unit, survival provisions and communications beacons," in *Advances in the Astronautical Sciences* (Peterson, N., ed.), vol. 16, pt. 1, pp. 680–692, Western Periodicals, North Hollywood, CA, 1963.

[47] Hornung, H., "Hypersonic flow over bodies in tandem," *Shock Waves*, vol. 11, no. 6, pp. 441–445, 2002.

[48] Houtz, N., "Optimization of inflatable drag devices by isotensoid design," AIAA Paper 64-437, 1st AIAA Annual Meeting, Washington, D.C., June 29-July 2 1964.

[49] Hughes, S., Dillman, R., Starr, B., Stephan, R., Lindell, M., Player, C., and Cheatwood, F., "Inflatable re-entry vehicle experiment (IRVE) design overview," AIAA Paper 2005-1636, 18th AIAA Aerodynamic Decelerator Systems Technology Conference and Seminar, Munich, Germany, May 23-26 2005.

[50] Hunter, J., *An Efficient Method for Time-Marching Supersonic Flutter Predictions Using CFD*. Masters thesis, Oklahoma State University, 1997.

[51] Ivanov, S., Kulikov, S., Pichkhadze, K., Serdyuk, V., Kassing, D., Marraffa, L., and Wilde, D., "New technology of payload return from space to the Earth," IAF Paper 00-V204, 51st IAF International Astronautical Congress, Rio de Janeiro, Brazil, Oct. 2-6 2000.

[52] James, B., Munk, M., and Moon, S., "Aerocapture technology project overview," AIAA Paper 2003-4654, 39th Joint Propulsion Conference and Exhibit, Huntsville, AL, July 20-23 2003.

[53] Jits, R. and Walberg, G., "High l/d Mars aerocapture for 2001, 2003, and 2005 mission opportunities," AIAA Paper 98-0299, 36th Aerospace Sciences Meeting, Reno, NV, Jan. 12-15 1998.

[54] Johnson, B. A., "Design, fabrication, and static testing of first-stage attached inflatable decelerator (AID) models," Tech. Rep. NASA-CR-111934, Sep. 1971.

[55] Johnson, W. and Lyons, D., "Titan ballute aerocapture using a perturbed TitanGRAM model," AIAA Paper 2004-5280, AIAA Atmospheric Flight Mechanics Conference and Exhibit, Providence, RI, Aug. 16-19 2004.

[56] Kayser, L., "Pressure distribution, heat transfer, and drag tests on the Goodyear ballute," Tech. Rep. AEDC-TDR-62-39, Arnold Air Force Station, March 1962.

[57] Kendall, R., "Techniques for space and hypersonic flight escape," in *SAE Aerospace Systems Conference*, pp. 394–400, Society of Automotive Engineers, Inc., New York, 1967.

[58] Kendall, R. and Maddox, A., "The use of inflatable structures for re-entry of orbiting vehicles," SAE Paper 901835, SAE Aerospace Technology Conference and Exposition, Long Beach,CA, Oct. 1- 4 1990.

[59] Kendall, Jr., R. and Kendall, Sr., R., "Advanced unmanned/manned space payload inflatable decelerator/delivery systems," AIAA Paper 95-3798, AIAA Space Programs and Technologies Conference, Huntsville, AL, Sep. 26-28 1995.

[60] Kruijff, M., Van der Heide, E., and Calzada Gil, S., "YES2 inherently-safe tethered re-entry mission and contingencies," IAC Paper 03-IAA.6.2.02,

54th International Astronautical Congress of the International Astronautical Federation, Bremen, Germany, Sep. 29 - Oct. 3 2003.

[61] Kruijff, M., Van der Heide, E., Dragoni, E., Castagnetti, D., and Ferretti, S., "Concept selection and design of the inherently safe re-entry capsule for YES2," IAC Paper 03-V.3.08, 54th International Astronautical Congress of the International Astronautical Federation, Bremen, Germany, Sep. 29 - Oct. 3 2003.

[62] Kustas, F., Rawal, S., Wilcockson, W., Edquist, C., Thornton, J., and Giellis, R., "Attached inflatable ballute for spacecraft deceleration," in *IEEE Aerospace Conference*, vol. 7, pp. 421–427, Institute of Electrical and Electronics Engineers, Piscataway, NJ., 2000.

[63] Kustas, F., Rawal, S., Willcockson, W., Edquist, C., Thornton, J., and Sandy, C., "Inflatable decelerator ballute for planetary exploration spacecraft," AIAA Paper 2000-1795, 41st AIAA/ASME/ASCE/AHS/ASC Structures, Structural Dynamics, and Materials Conference and Exhibit, Atlanta, GA, April 3-6 2000.

[64] Kyser, A., "Deployment mechanics for an inflatable tension-cone decelerator," Tech. Rep. NASA-CR-929, NASA, Nov. 1967.

[65] LeBeau, G. and Lumpkin, F.E., I., "Application highlights of the DSMC analysis code (DAC) software for simulating rarefied flows," *Computer Methods in Applied Mechanics and Engineering*, vol. 191, no. 6-7, pp. 595–609, 2001.

[66] Lesoinne, M. and Farhat, C., "Higher-order subiteration-free staggered algorithm for nonlinear transient aeroelastic problems," *AIAA Journal*, vol. 36, no. 9, pp. 1754–1757, 1998.

[67] Ling, L., Baseggio, F., and Fuhry, D., "Parametric entry corridors for Lunar/Mars aerocapture missions," Tech. Rep. NASA-TM-102178, NASA, Apr. 1991.

[68] Liu, D., Yao, Z., Sarhaddi, D., and Chavez, F., "From piston theory to a unified hypersonic-supersonic lifting surface method," *Journal of Aircarft*, vol. 34, no. 3, pp. 304–312, 1997.

[69] Livermore Software Technology Corp., *LS-DYNA Keyword User's Manual*, 970 ed., 2003.

[70] London, H., "Change of satellite orbit plane by aerodynamic maneuvering," *Journal of the Aerospace Sciences*, vol. 29, no. 3, pp. 323–332, 1961.

[71] Lyons, D. and Johnson, W., "Ballute aerocapture trajectories at Neptune," AIAA Paper 2004-5181, AIAA Atmospheric Flight Mechanics Conference and Exhibit, Providence, RI, Aug. 16-19 2004.

[72] Marshall, D. and Ruffin, S., "A new inviscid wall boundary condition treatment for embedded boundary cartesian grid schemes," AIAA Paper 2004-0583, 42nd AIAA Aerospace Sciences Meeting and Exhibit, Reno, NV, Jan. 5-8 2004.

[73] Masciarelli, J., Lin, J., Ware, J., Rohrschneider, R., Braun, R., Bartels, R., Moses, R., and Hall, J., "Ultra lightweight ballutes for return to Earth from the Moon," AIAA Paper 2006-1698, AIAA/ASME/ASCE/AHS/ASC Structures, Structural Dynamics and Materials Conference, Newport, RI, May 1-4 2006.

[74] Masciarelli, J., Rousseau, S., Fraysse, H., and Perot, E., "An analytic aerocapture guidance algorithm for the Mars Sample Return orbiter," AIAA Paper 2000-4116, AIAA Atmospheric Flight Mechanics Conference, Denver, CO, Aug. 14-17 2000.

[75] Matthies, H. and Steindorf, J., "Partitioned strong coupling algorithms for fluid-structure interaction," *Computers & Structures*, vol. 81, no. 8-11, pp. 805–812, 2003.

[76] Mayhue, J. and Eckstrom, C., "Flight-test results from supersonic deployment of an 18-foot-diameter 5.49 meter/towed ballute decelerator," Tech. Rep. NASA-TM-X-1773, NASA, May 1969.

[77] Maynard, J., "Aerodynamic characteristics of parachutes at Mach numbers from 1.6 to 3," Tech. Rep. NASA-TN-D-752, NASA, May 1961.

[78] McIntyre, T., Lourel, I., Eichmann, T., Morgan, R., Jacobs, P., and Bishop, A., "Experimental expansion tube study of the flow over a toroidal ballute," *Journal of Spacecraft and Rockets*, vol. 41, no. 5, pp. 716–725, 2004.

[79] McNamara, J., Thuruthimattam, B., Friedmann, P., Powell, K., and Bartels, R., "Hypersonic aerothermoelastic studies for reusable launch vehicles," AIAA Paper 2004-1590, 45th AIAA/ASME/ASCE/AHS/ASC Structures, Structural Dynamics, and Materials Conference, Palm Springs, CA, April 19-22 2004.

[80] McRonald, A., "A light-weight inflatable hypersonic drag device for planetary entry," AIAA Paper 99-0422, Association Aeronautique de France Conference, Arcachon, France, Mar. 16-18 1999.

[81] McRonald, A., "A light-weight inflatable hypersonic drag device for Venus entry," AAS Paper 99-355, AAS/AIAA Astrodynamics Specialist Conference, Girdwood, AK, Aug. 16-19 1999.

[82] McRonald, A., "A light-weight hypersonic inflatable drag device for a Neptune orbiter," AIAA Paper 2000-0123, AAS/AIAA Space Flight Mechanics Meeting, Clearwater, FL, Jan. 23-26 2000.

[83] McShera, J.T., J., "Aerodynamic drag and stability of towed inflatable decelerators at supersonic speeds," Tech. Rep. NASA-TN-D-1601, NASA, Mar. 1 1963.

[84] McShera, J.T., J. and Bohon, H., "A summary of supersonic decelerators with emphasis on problem areas in aerodynamics and structures," AIAA Paper 67-201, AIAA Aerospace Sciences Meeting, New York, NY, Jan. 23-26 1967.

[85] McShera, J.T., J. and Keyes, J., "Wind tunnel investigation of a balloon as a towed decelerator at Mach numbers from 1.47 to 2.50," Tech. Rep. NASA-TN-D-919, NASA, Aug. 1961.

[86] Miller, K., Gulick, D., Lewis, J., Trochman, B., Stein, J., Lyons, D., and Wilmoth, R., "Trailing ballute aerocapture - concept and feasibility assessment," AIAA Paper 2003-4655, 39th AIAA/ASME/SAE/ASEE Joint Propulsion Conference and Exhibit, Huntsville, AL, July 20-23 2003.

[87] Miller, K., Masciarelli, J., Hausle, F., Riesco, M., Sharma, D., Zeller, C., Gnoffo, P., Buck, G., Ware, J., and Rohrschneider, R., "Ultralightweight ballute technology for aerocapture and aeroassist missions," Tech. Rep. To be published as a NASA-CR-1999 report, NASA, Jan. 2007.

[88] Morel, Q., Hobbs, S., and Kruijff, M., "Cranfield's inherently safe reentry capsule design for YES2," IAC Paper 03-U.1.07, 54th International Astronautical Congress of the International Astronautical Federation, Bremen, Germany, Sep. 29 - Oct. 3 2003.

[89] Morley, C., *GasEQ: A Chemical Equilibrium Program*. http://www.gaseq.co.uk, 0.79 ed.

[90] Morton, S., Melville, R., and Visbal, M., "Accuracy and coupling issues of aeroelastic navier-stokes solutions on deforming meshes," *Journal of Aircarft*, vol. 35, no. 5, pp. 798–805, 1998.

[91] Moss, J., Blanchard, R., Wilmoth, R., and Braun, R., "Mars pathfinder rarefied aerodynamics: Computations and measurements," AIAA Paper 98-0298, 36th Aerospace Sciences Meeting and Exhibit, Reno, NV, Jan. 12-15 1998.

[92] Mosseev, Y., "The multipurpose integrated PC-software for structural and aeroelastic analysis of decelerators, paragliders and balloons," AIAA Paper 97-1455, 14th AIAA Aerodynamic Decelerator Systems Technology Conference, San Francisco, CA, June 3-5 1997.

[93] Mosseev, Y., "The decelerator pitch-dependent performances prediction based on 3D aeroelastic analysis," AIAA Paper 99-1717, 15th CEAS/AIAA Aerodynamic Decelerator Systems Technology Conference, Toulouse, France, June 8-11 1999.

[94] Mulqueen, J., "Applications of low lift to drag ratio aerobrakes using angle of attack variation for control," Tech. Rep. NASA-TM-103544, NASA, June 1991.

[95] Musil, J., "Study of expandable, terminal decelerators for Mars atmosphere entry, volume I - final summary report," Tech. Rep. GER-12842, vol. 1, Goodyear Aerospace Corp., Oct. 3 1966.

[96] Naghipour, M., Taheri, F., and Zou, G., "Evaluation of vibration damping of glass-reinforced-polymer-reinforced glulam composite beams," *Journal of Structural Engineering*, vol. 131, no. 7, pp. 1044–1050, 2005.

[97] "NASA space science strategic plan, Nov. 2000." http://www.hq.nasa.gov/office/codez/plans/SSE00plan.pdf, Accessed on June 17, 2005, 2000.

[98] Olejniczak, J., Wright, M., Prabhu, D., Takashima, N., Hollis, B., Zoby, E., and Sutton, K., "An analysis of the radiative heating environment for aerocapture at Titan," AIAA Paper 2003-4953, 39th AIAA/ASME/SAE/ASEE Joint Propulsion Conference and Exhibit, Huntsville, AL, July 20-23 2003.

[99] Park, C., "A survey of aerobraking orbital transfer vehicle design concepts," AIAA Paper 87-514, 25th AIAA Aerospace Sciences Meeting, Reno, NV, Jan. 12-15 1987.

[100] Park, C., "Theory of idealized two-dimensional ballute in newtonian hypersonic flow," *Journal of Spacecraft and Rockets*, vol. 25, no. 3, p. 986, 1988.

[101] Piperno, S. and Farhat, C., "Energy based design and analysis of staggered solvers for nonlinear transient aeroelastic problems," AIAA Paper 2000-1447, 41st AIAA/ASME/ASCE/AHSIASC Structures, Structural dynamics, and Materials Conference and Exhibit, Atlanta, GA, Apr. 3-6 2000.

[102] Piperno, S. and Farhat, C., "Partitioned procedures for the transient solution of coupled aeroelastic problems - part ii: energy transfer analysis and three-dimensional applications," *Computer Methods in Applied Mechanics and Engineering*, vol. 190, no. 24-25, pp. 3147–3170, 2001.

[103] Piperno, S., Farhat, C., and Larrouturou, B., "Partitioned procedures for the transient solution of coupled aeroelastic problems - part i: Model problem, theory and two-dimensional application," *Computer Methods in Applied Mechanics and Engineering*, vol. 124, no. 1-2, pp. 79–112, 1995.

[104] Powell, R. and Braun, R., "A six degree-of-freedom guidance and control analysis of Mars aerocapture," *Journal of Guidance, Control and Dynamics*, vol. 16, no. 6, pp. 1038–1044, 1993.

[105] Prada y Nogueira, I., Forlivesi, F., and Morel, Q., "The FEM applicability for the first-stage design of inflatable bodies. iteration methodology between FD and FEM for the inherently safe re-entry capsule for YES2. the breogan leakage protection system.," IAC Paper 03-U.3.04, 54th International Astronautical Congress of the International Astronautical Federation, Bremen, Germany, Sep. 29-Oct. 3 2003.

[106] Rasheed, A., Fujii, K., Hornung, H., and Hall, J., "Experimental investigation of the flow over a toroidal aerocapture ballute," AIAA Paper 2001-2460, 19th AIAA Applied Aerodynamics Conference, Anaheim, CA, June 11-14 2001.

[107] Seide, P., Weingarten, V., and Morgan, E., "Final report on the development of design criteria for elastic stability of thin shell structures," Tech. Rep. AFBMF/TR-61-7, US Air Force, Dec. 1960.

[108] Smith, C. and Wereley, N., "Transient analysis for damping identification in rotating composite beams with integral damping layers," *Smart Materials and Structures*, vol. 5, no. 5, pp. 540–550, 1996.

[109] Smith, T., McCoy, E., Krasinski, M., Limaye, S., Shook, L., Uhelsky, F., and Graham, W., "Ballute and parachute decelerators for FASM/QuickLook UAV," AIAA Paper 2003-2142, 17th AIAA Aerodynamic Decelerator Systems Technology Conference and Seminar, Monterey, CA, May 19-22 2003.

[110] Stroud, W. and Zender, G., "Experimental investigation to determine utility of tension shell concept," Tech. Rep. NASA-TM-X-1211, NASA, Mar. 1966.

[111] Su, X., Abdi, F., Taleghani, B., and Blandino, J., "Wrinkling analysis of a Kapton square membrane under tensile loading," AIAA Paper 2003-1985, 44th AIAA/ASME/ASCE/AHS Structures, Structural Dynamics, and Materials Conference, Norfolk, VA, Apr. 7-10 2003.

[112] Sutton, K. and Graves, R.A., J., "A general stagnation-point convective-heating equation for arbitrary gas mixtures," Tech. Rep. NASA-TR-R-376, NASA, 1971.

[113] Tauber, M., "A review of high-speed, convective, heat-transfer computation methods," Tech. Rep. NASA-TP-2914, NASA, 1989.

[114] Tauber, M. and Sutton, K., "Stagnation-point radiative heating relations for Earth and Mars entries," *Journal of Spacecraft and Rockets*, vol. 28, no. 1, pp. 40–42, 1991.

[115] Tessler, A., Sleight, D., and Wang, J., "Nonlinear shell modeling of thin membranes with emphasis on structural wrinkling," AIAA Paper 2003-1931, 44th AIAA/ASME/ASCE/AHS/ASC Structures, Structural Dynamics, and Materials Conference, Norfolk, VA, Apr. 7-10 2003.

[116] Thuruthimattam, B., Friedmann, P., MacNamara, J., and Powell, K., "Aeroelasticity of a generic hypersonic vehicle," AIAA Paper 2002-1209, 43rd AIAA/ASME/ASCE/AHS Structures, Structural Dynamics, and Materials Conference, Denver, CO, Apr. 22-25 2002.

[117] Topping, A., "Ring buckling of inflated drag bodies," *Journal of Aircarft*, vol. 8, no. 11, pp. 869–874, 1970.

[118] Tu, S. and Ruffin, S., "Solution adaptive, unstructured cartesian-grid methodology for chemically reacting flows," AIAA Paper 2002-3097, 8th AIAA/ASME Joint Thermophysics and Heat Transfer Conference, St. Louis, MO, Jun 24-26 2002.

[119] Tucker, M. and Pitt, E., *Waves in Ocean Engineering*, vol. 5 of *Elsevier Ocean Engineering Book Series*. Oxford: Elsevier Sciences, Ltd., 2001.

[120] Van der Heide, E. J., Kruijff, M., Avanzini, A., Liedtke, V., and Karlovsky, A., "Thermal protection testing of the inflatable capsule for YES2," IAC Paper 03-I.3.05, 54th International Astronautical Congress of the International Astronautical Federation, Bremen, Germany, Sept. 29 - Oct. 3 2003.

[121] Walberg, G., "A survey of aeroassisted orbit transfer," *Journal of Spacecraft and Rockets*, vol. 22, no. 1, pp. 3–18, 1985.

[122] Wang, J., Chen, T., Sleight, D., and Tessler, A., "Simulating nonlinear deformations of solar sail membranes using explicit time integration," AIAA Paper 2004-1580, 45th AIAA/ASME/ASCE/AHS/ASC Structures, Structural Dynamics, and Materials Conference, Palm springs, CA, Apr. 19-22 2004.

[123] Warzecha, L., "Performance and design considerations for maneuvering space vehicles," IAS Paper 60-59, IAS National Summer Meeting, Los Angeles, CA, June 28-July 1 1960.

[124] Weeks, G., "Buckling of a pressurized toroidal ring under uniform external loading," Tech. Rep. NASA-TN-D-4124, NASA, Aug. 1967.

[125] Wercinski, P., Henline, W., Tran, H., Milos, F., Papadopoulos, P., Chen, Y.-K., and Venkatapathy, E., "Trajectory, aerothermal conditions and thermal protection system mass for the MARS 2001 aerocapture mission," AIAA Paper 97-472, 35th Aerospace Sciences Meeting and Exhibit, Reno, NV, Jan. 6-10 1997.

[126] Westhelle, C. and Masciarelli, J., "Assessment of aerocapture flight at Titan using a drag-only device," AIAA Paper 2003-5389, AIAA Atmospheric Flight Mechanics Conference and Exhibit, Austin, TX, Aug. 11-14 2003.

[127] White, W. and Riddle, C., "An investigation of the deployment characteristics and drag effectiveness of the gemini personnel decelerator at subsonic and supersonic speeds, phase II," Tech. Rep. AEDC-TDR-63-255, Dec. 1963.

[128] Wilde, D. and Walther, S., "Flight test and ISS application of the inflatable reentry and descent technology (IRDT)," *Acta Astronautica*, vol. 51, no. 1-9, pp. 83–88, 2002.

[129] Wilmoth, R., *DACFREE: A Free-Molecular/Newtonian Code for Hypersonic Flow*. NASA Langley Research Center, Aerothermodynamics Branch.

[130] Wilmoth, R., Blanchard, R., and Moss, J., "Rarefied transitional bridging of blunt body aerodynamics," 21st International Symposium on Rarefied Gas Dynamics, Marseille, France, July 1998.

[131] Wright, M., Bose, D., and Olejniczak, J., "Impact of flowfield-radiation coupling on aeroheating for Titan aerocapture," *Journal of Thermophysics and Heat Transfer*, vol. 19, no. 1, pp. 17–27, 2005.

[132] Yavrouian, A., Yen, S., Plett, G., Cutts, J., and Baek, D., "Evaluation of materials for Venus aerobot applications," AIAA Paper 99-3859, 13th Lighter Than Air Technology Conference and AIAA International Balloon Technology Conference, Norfolk, VA, June 28-July 1 1999.

[133] Yavrouian, A., Yen, S., Plett, G., and Weissman, N., "High temperature materials for Venus balloon envelopes," AIAA Paper 95-1617, 11th Lighter Than Air Technology Conference, Clearwater, FL, May 16-18 1995.

[134] Zacharov, A., "MARS-96." http://www.iki.rssi.ru/mars96/09_mars_3.htm, Accessed on Oct. 18, 2005.